Architecture and Engineering Series

# Load Paths in Historic Truss Bridges

## Researching realistic lateral strength of these bridges and seeking improvements over traditional analytical methods

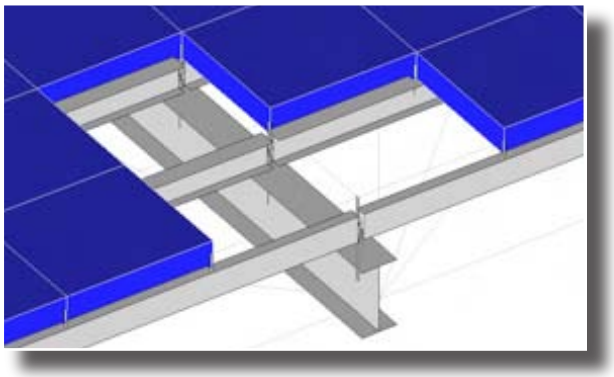

University of Colorado at Denver

2004-25

National Center for Preservation Technology and Training
*Technology Serving the Future of America's Heritage*
*www.ncptt.nps.gov/products*

**ACKNOWLEDGEMENTS**

The University of Colorado at Denver has completed this work funded in part by Grant # MT-2210-04-NC-12 from the National Center for Preservation Technology and Training and Grant # 2004-M1-019 from the State Historical Fund of the Colorado Historical Society. Further, the cooperation of the bridge owners is acknowledged: City of Fruita, CO; Bent County, CO; Summit County, CO; Montrose County, CO; and Garfield County, CO. The assistance Val Moser and Don Brown of Campbell Scientific, Inc. is gratefully acknowledged.

In addition to Principal Project Contact Kevin L. Rens and Principal Investigator Frederick R. Rutz, the following University of Colorado at Denver students and others assisted in laboratory and field investigations throughout the project:
Mohammad Abu-Hassan, Paul Bountry, Sam Brown, Nick Clough, Jennifer Davis, Kazwan Elias, Aaron Erfman, Helen Frey, Shohreh Hamedian, Paul Jacob, Veronica Jacobson, Chris Kline, Clint Krajnik, Peter Marxhausen, Andy Pultorak, William Swigert, and Jim Van Liere.

**ABSTRACT**
The stiffening effect of existing features on historic truss bridges was examined. 3D analytical models as traditional skeleton structures were compared to models that included the bridge decks. The analytical models were compared to field tests under real wind conditions. A methodology for use of stiffening elements such as decks is offered to aid engineers in historic bridge preservation efforts.

## PART 1 GENERAL DESCRIPTION

### 1.1 Introduction

Developments in the engineering design and construction of truss bridges illustrate a history of engineering innovations. While historic bridges present these developments in a forum readily accessible for public viewing, only a small fraction of this engineering heritage remains. Historic truss bridges from the late 19$^{th}$ and early 20$^{th}$ centuries are vanishing rapidly. 60% of Colorado through-truss bridges in existence 20 years ago have been removed (Rutz 2004a) and it is estimated that 50% of the nation's truss bridges have been removed over the same time period (DeLony 2005). At this rate of attrition, the American engineering legacy of the truss bridge may soon be relegated to the history books.

One avenue for preservation is rehabilitation of such bridges for pedestrian use. Conversion to pedestrian use permits ready public access to historic structures and has the added advantage of providing incentives for continued maintenance. Unfortunately, the engineer for today's historic bridge preservation project often finds the bridge has insufficient lateral strength to satisfy modern requirements (Rutz and Rens 2004). This is due to two circumstances that combine together, hampering preservation projects: (1) today's design wind load is significantly higher than that used for the original design a

century ago and (2) the use of traditional structural analysis can lead to an incorrect conclusion that wind load results in structure overstress.

## 1.2 Goals

The focus of research at the University of Colorado at Denver has been on the identification of alternate load paths in historic truss bridges. Modern methods are being employed to aid in the preservation of this technological heritage. There is strong evidence that alternative load paths do exist – they have just been overlooked for the past century or so. While the overall purpose of the project is to aid in preservation efforts for historic iron and steel truss bridges, the specific goal of this project is to demonstrate a new methodology to account for increased strength from non-traditional (but real) load paths.

## 1.3 Rehabilitation for Preservation

Rehabilitation for pedestrian use is a practical and popular way to preserve these historic structures. But the American Association of State Highway and Transportation Officials (AASHTO) *Guide Specifications for the Design of Pedestrian Bridges* (AASHTO 1997) throws an obstacle in the way. It mandates modern wind load design criteria. Structural engineers attempting to rehabilitate historic bridges from former highway to modern pedestrian use often discover that the old structures lack the strength to resist the AASHTO wind load criteria. This can contribute to either a “heavy-handed” design approach, which is both expensive and detrimental to the historic character to be preserved in the first place, or condemnation of the bridge.

A dichotomy presents itself: On the one hand, historic truss bridges often do not possess "code-compliant" lateral resistance for current wind load requirements. Yet in case after case observations reveal *no* physical evidence to suggest that wind has caused damage or distress, even after a century of exposure. At this age, bridges have indeed weathered many severe windstorms.

## 1.4 Traditional vs. Modern Analysis

Traditional structural analyses of truss bridges are based on a "skeleton" frame analysis, the classic textbook method, which has been used since 1847 (Rutz 2004b). While the *techniques* of analysis have changed – computer analysis vs. manual calculations – the *basis* has remained basically unchanged. Engineers are so accustomed to this direct methodology that alternative load paths are customarily neglected. Further, seldom does the practicing engineer have the budget to complete time-consuming analytical studies, nor the inclination to accept liability for new and untried methodologies.

Traditional structural analysis is based on a "skeleton" frame, such as is illustrated in Figure 2.1. The "computer" in the 19$^{th}$ century design office was the individual who completed the calculations, using the classic textbook methods of joints and sections (Ketchum 1908) or graphical methods that simplified some of the arithmetic (Waddell 1898a). Today's practitioner using one of the many readily available computer programs is really utilizing matrix algebra. The "computer" is now a machine, but it does the same

job – it performs the calculations. While the practices have changed, the fundamental basis is still the same – a “skeleton” frame is still assumed.

## 1.5 Summary of Bridges Studied

It was believed that to be of the greatest practical value in aiding preservation efforts that real bridges be examined. The study focused on five real – not “textbook” – structures located throughout Colorado as shown in Figures 1.1 through 1.13. All of the bridges are through-trusses, all are former highway bridges, all are pin-connected with moment-resisting portal frames at the ends, all are metal – either wrought iron or steel, and all have horizontal trusses consisting of rod X-bracing intended to resist lateral loads.

Figure 1.1. Fruita Bridge over the Colorado River, near Fruita Colorado. This three-span steel Parker truss was built in 1907. Each 47-meter (155-feet) span has eight bays. It has steel floor beams and timber stringers covered by a timber deck. Steel eyebars serve as bottom chords and principal diagonals and steel rods provide counterbracing. It served until a replacement bridge was built about one half mile downstream in 1970, and has been abandoned since then. The former wood railing has fallen away. The City of Fruita would like to reopen the bridge for pedestrian and bicycle use as part of a connecting bikeway leading to nearby tourist attractions, but has been stymied by the expense of rehabilitation. The north span, which was instrumented, is at the far right.

Figure 1.2. Fruita Bridge Deck. The deck timbers are spiked to timber stringers, which bear on steel floor beams. The deck is discontinuous in that there are gaps between the deck timbers. The short vertical timbers are the remnants of a former wood railing.

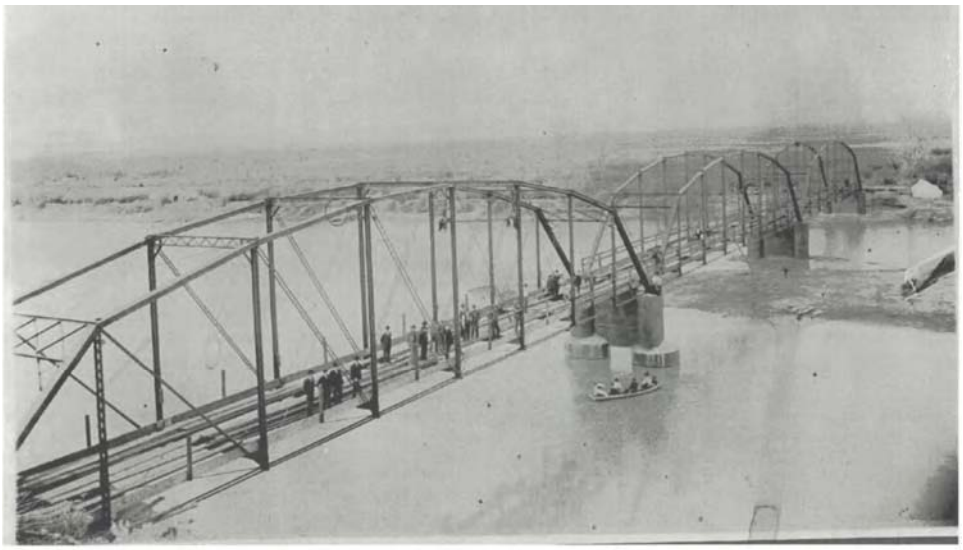

Figure 1.3. Photo of Fruita Bridge believed to be from spring of 1907, when the bridge was under construction. Most of the timber stringers have been set on the floor beams, but are laying flat, with people are standing on them. The stringers on the exterior sides are oriented vertically and the wood posts for the railing have been installed. (Photo courtesy of Museum of Western Colorado).

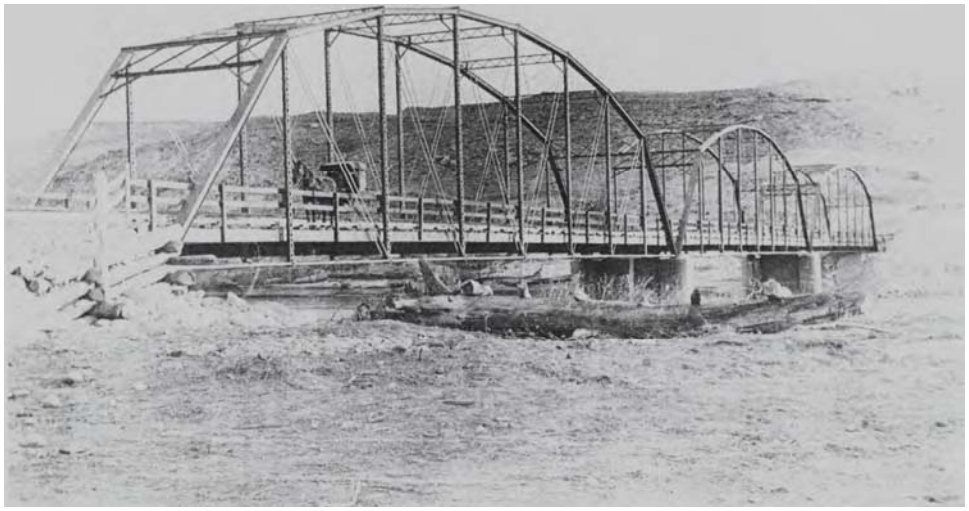

Figure 1.4. Undated photograph of completed bridge. The deck timbers can be seen in place over the timber stringers and the wood rail can be seen. The view is from north to south. The north approach consists of backfill, contained by log wing walls. (Photo courtesy of Museum of Western Colorado).

Figure 1.5. Prowers Bridge over the Arkansas River, near Lamar, Colorado. This bridge consists of one 5 panel Pratt pony truss built in 1921, three 9 panel Camelback Pratt through trusses built in 1909, two 6 panel Pratt through truss built in 1902 and 1906. The 49-meter (160-feet) Camelback Pratt through truss span, seen in this photo, was instrumented because it received the greatest wind exposure. It has steel floor beams with steel stringers, covered by a corrugated metal deck with asphalt pavement. It has steel eyebar bottom chords and diagonals with steel rod counterbracing. The railing is a steel lattice with single angle top and bottom rails. Virtually all paint has weathered away. It survived a major flood of the Arkansas River in 1921 and served as a highway bridge until its abandonment in 1994 when a nearby replacement bridge was constructed.

Figure 1.6. Prowers Bridge Deck. The steel stringers are riveted to the floor beams, suggesting that the stringers are original. However, the corrugated bridge deck is clearly a replacement. Asphalt pavement, now significantly weathered, was installed over the corrugated deck.

Figure 1.7. Blue River Bridge over the Blue River near Silverthorne/Dillon, Colorado. This 37-meter (120 feet)-span steel Pratt truss has five bays, with a timber deck on steel stringers. It has steel eyebar bottom chords and diagonals and steel rod X-bracing at the center bay. The railing is a steel lattice with double angle top and bottom rails. It is believed to have been built approximately 1895 as the Two-Mile Bridge near Breckenridge, Colorado and moved to this site at a later, but unknown, date. It is known to have been in its present location when the Dillon Dam was built immediately upstream in 1960. Closed to vehicular use, it is still used as a pedestrian crossing of the Blue River.

Figure 1.8. Blue River Bridge Deck. The deck consists of longitudinal "running boards" on transverse timbers on steel stringers. The orthogonal criss-crossing of running boards and deck timbers creates a much more continuous deck than that at Fruita Bridge. The steel stringers bear on and are mechanically attached to the steel floor beams.

Figure 1.9. San Miguel Bridge over San Miguel River near Uravan, Colorado. This 43-meter (142–feet) wrought iron Pratt truss was built in 1886 as part of a five-span Fifth Street Bridge over the then Grand (now Colorado) River at Grand Junction, Colorado. One span was relocated to the San Miguel river location in the 1930's. It has a roadway of gravel on an unusual system of semi-circular lengths of corrugated metal pipe set between steel stringers. It has wrought iron eyebar bottom chords and diagonals and wrought iron rod counterbracing. A steel vehicular rail has replaced the original railing. It served the mining industry in western Colorado until the 1980's. Abandoned since 1990, it remains the oldest bridge originally built in Colorado.

Figure 1.10. San Miguel Bridge Deck. The deck, believed to have been installed in 1964, consists of gravel roadbase on semi-circular corrugated metal pipe segments which bear on the bottom flanges of steel stringers. The metal pipe has been replaced with timber blocks in a few places where the corrugated metal pipe has rusted away.

Figure 1.11. Fifth Street Bridge over Grand River, Grand Junction, CO. Built in 1886, this Pratt truss was of wrought iron construction. One span of this bridge was relocated to the San Miguel location in the 1930's. Note the timber deck and very simple, single board railing. (Photo courtesy of Museum of Western Colorado).

Figure 1.12. Rifle Bridge over the Colorado River at Rifle, Colorado. This 73 meter (240-foot) span Pennsylvania truss comprises the longer of two different spans at that location. It has steel floor beams with steel stringers, covered by a corrugated metal deck with asphalt pavement. It has steel eyebar bottom chords and diagonals and steel rod counterbracing. The railing is a steel lattice with double angle top and bottom rails. It has been abandoned since the late 1960's, when a replacement bridge was constructed.

Figure 1.13. Rifle Bridge deck. The deck of (weathered) asphalt pavement on corrugated bridge deck on a combination of steel and timber stringers is similar to that of the Prowers Bridge.

## 1.6 Loads

Superimposed dead load and superimposed live load are still computed manually, the same way as the 19th century designer. Self-weight may be computed manually, or may be determined by software. The *AASHTO Guide Specifications for the Design of Pedestrian Bridges* (AASHTO, 1997) prescribes the live load value. It may vary between 3.11 kPa to 4.07 kPa (65 psf to 85 psf), depending on the area of the walkway. The late 19th century and early 20th century designer selected design wind loads on a case-by-case basis, which varied typically from 1.44 kPa to 2.39 kPa (30 psf to 50 psf) applied to the projected area of the components (Smith 1881, Waddell 1898, and Cooper 1905). Today's AASHTO *Guide Specifications for the Design of Pedestrian Bridges* mandates 3.59 kPa (75 psf) applied to the same area.

## 1.7 Materials

The surviving truss bridges are almost always of wrought iron or steel, although a relatively small number of timber trusses remain. However, allowable stresses for iron and steel are presently at higher levels than when they were designed (Hatfield 2001).

## 1.8 Customary Analysis

Today's typical analysis for truss bridges used for pedestrian crossings would be based on:

- AASHTO wind load determined from a pressure of 3.59 kPa (75 psf).

- "Pin" boundary conditions for both bearings at one end and "roller" boundary conditions for both bearings at the other end.
- Internal member-to-member connections treated as pinned
- Probably a 3D skeleton analysis, although some engineers still use 2D analysis of the vertical trusses and for the top and bottom horizontal trusses and combine the results. For a 3-D model, a true "pin" boundary condition is a joint that is restrained from translation in all three degrees of freedom (DOF), but the three rotational DOF's are released. The "pin" support acts like a ball joint. A true "roller" boundary condition is the same as a "pin" with an additional release for translation in the bridge longitudinal direction.

It may be noted that the term "pin", meaning "free to rotate" as used in modern structural analysis, derives from 19$^{th}$ century analyses of trusses that had true physical pins.

# PART 2 MODELING & ANALYSIS

## 2.1 Modeling Considerations

In this Section, two bridge configurations were compared for each of the five bridges studied: a skeleton model and a deck model. The choice for boundary conditions for both configurations was pinned joints at one end and roller joints at the other. The roller joints are restrained from lateral translation, but are free to translate in the longitudinal direction of the bridge. The condition of internal member connections was pinned, that is released to rotate. These choices are not necessarily theoretically correct, but were chosen because it was believed that most designers would select them.

## 2.2 Fruita Bridge

A pin-connected skeleton frame, shown in Fig. 2.1, was analyzed under AASHTO loads. This analysis was compared to the deck model subject to the same loads. As-built dimensions and section properties from the Fruita Bridge were used. Because it was desired to investigate the problem using software tools that were readily available to practicing engineers, RISA-3D software (RISA 2002) was used for both analyses. RISA-3D is exemplary of readily available software that includes both frame elements and plate/shell elements.

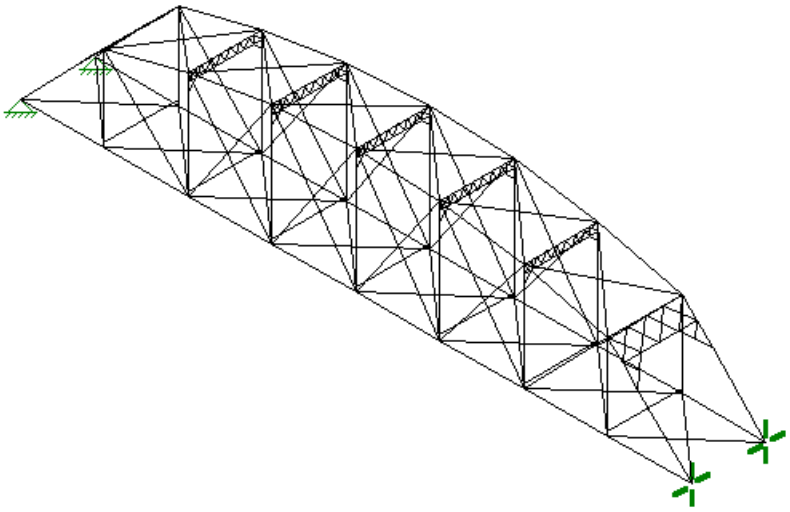

Figure 2.1. 3D model of the Fruita Bridge, illustrating the traditional skeleton based on the steel members only. The boundary conditions of pinned at one end and rollers at the other end are indicated. The rollers are restrained from translation in the lateral direction.

Figures 2.2 and 2.3 illustrate the superimposed vertical dead loads (gravity loads) and their effect, respectively, for the skeleton structure. Live load was not included in the analysis.

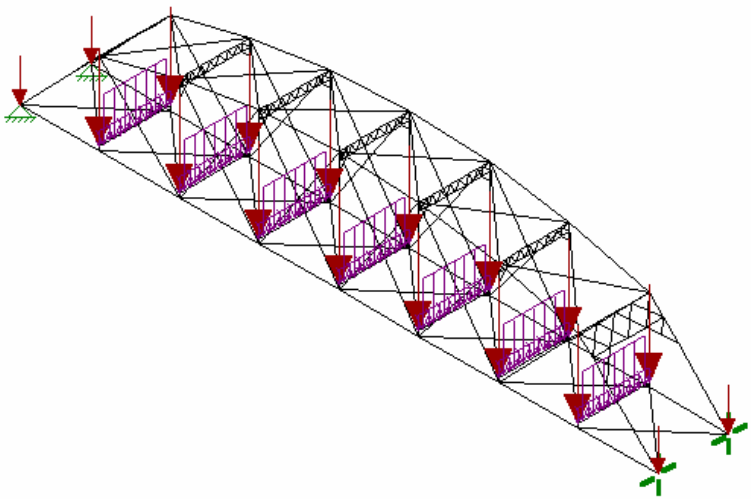

Figure 2.2. Fruita Bridge: Representation of superimposed gravity loads.

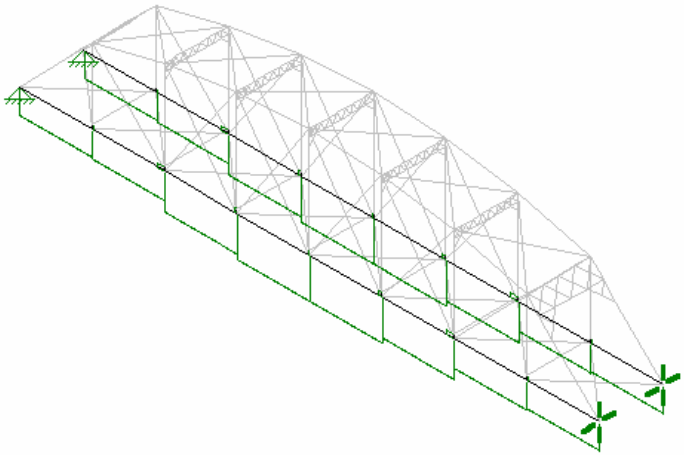

Figure 2.3. Fruita Bridge: Graphical representation of relative axial forces in the bottom chord eyebars due to gravity loads for the skeleton structure.

Figures 2.4 and 2.5 illustrate the wind load and its effect on the skeleton structure. The lateral loads due to wind were based on the AASHTO criteria of 3.59 kPa (75 psf). This is the customary approach for truss bridge lateral analysis today.

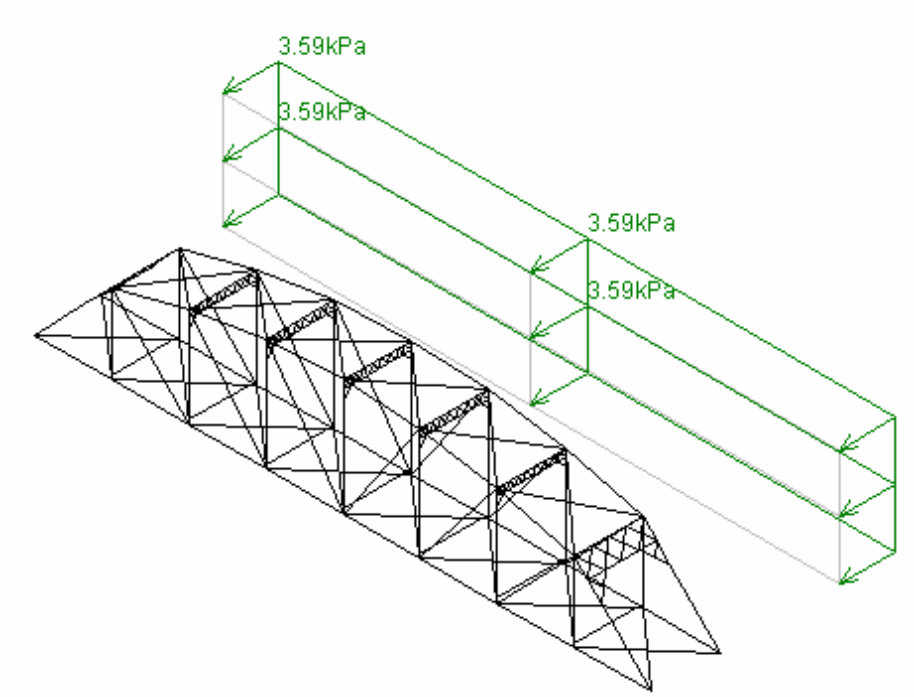


Figure 2.4. Fruita Bridge: Representation of wind pressure on the bridge.

Figure 2.5 shows a representation of axial forces in the bottom chord eyebars due to wind load. Tension predominates on the leeward side while compression predominates on the windward side. Note that with a 3D analysis there is a reversal of sign in the member forces on both sides near the pinned ends. This reversal is not detected if the "combined 2D" method is used for the analysis. It is due to the couple in the lateral direction created by the pinned restraints at one end, and is similar to the basic "propped cantilever" condition, diagrams for which are reproduced in Figure 2.6.

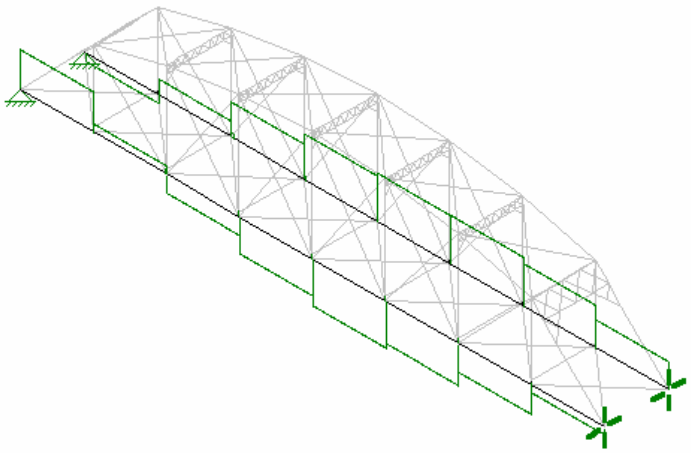

Figure 2.5. Fruita Bridge: Graphical representation of axial forces in the bottom chord eyebars due to wind for the skeleton structure. Note the reversal in sign for the bottom chords near the pinned boundary conditions (at left of the figure).

The compression due to wind load was greater than tension due to dead load only, leaving the eyebars on the windward side subject to buckling when the "skeleton" analysis is used. A logical engineering solution to the perceived buckling problem would be to decrease the *kl/r* of these members – with consequent detriment to the preservation of bridge's historic character.

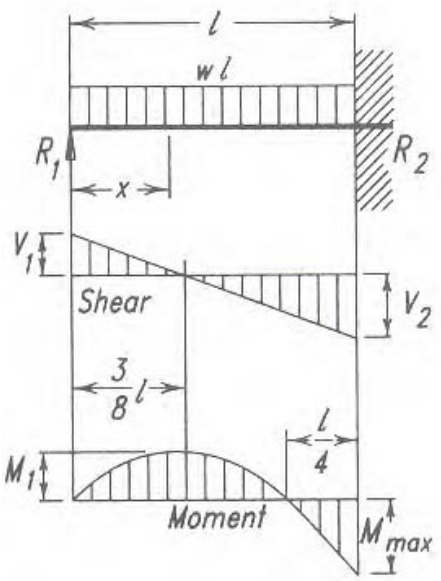


Figure 2.6. Shear and moment diagrams for "propped cantilever" condition, from the AISC Manual of Steel Construction (AISC 2001). The moment at the fixed end is analogous to a couple induced by lateral loads at the pinned ends of the skeleton truss shown in Figure 2.5.

The next step was to add plate elements to the model with stringers. The wood plank deck was modeled using 800 plate elements on wood stringers, added to the skeleton model, and is shown in Figure 2.7. For the deck model, both timber stringers and a timber deck were included in the model. Individual deck planks, with gaps between the planks, were approximated. The actual deck planks are spiked to the timber stringers so the model approximated the spiked connection as pinned. Pinned joints also approximated the stringer to floor beam connection. The model used frame elements for all members except the deck, which is modeled with RISA plate/shell elements. These elements are four-joint quadrilateral elements. They are called "mixed interpolation elements" in that they are based on plate assumptions with added interpolating functions for out-of-plane transverse shear (Bathe 1996). This approach is analogous to

incorporating shear deformation with flexural effects from beam theory, resulting in an element that can be used for thin and thick (this case) plate applications (RISA 2002).

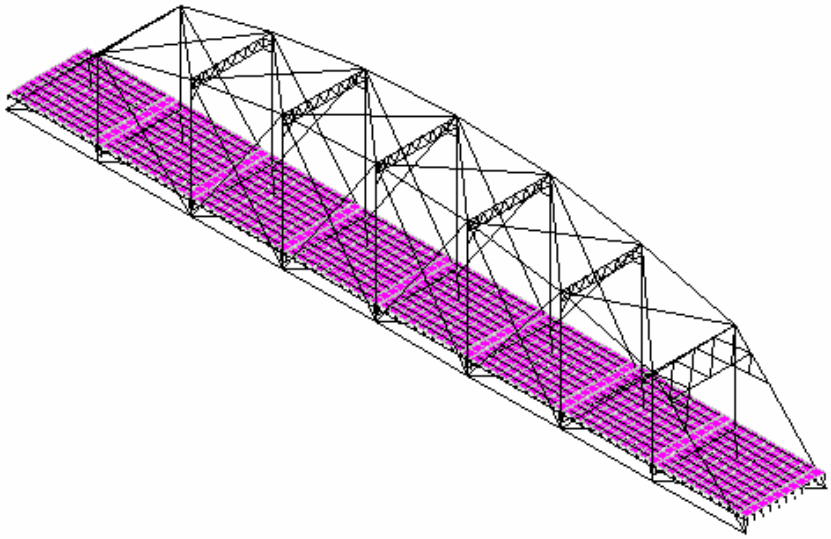

Figure 2.7. Fruita Bridge: Skeleton model with stringers and deck. The deck was modeled with plate elements to approximate individual deck planks with small gaps between them.

The stringers bear on the floor beams as shown in the rendering in Figure 2.8. The frame elements were offset from each other as illustrated in Figure 2.9, to represent the stacking of actual stringers on the floor beams. The plate elements were offset in a similar manner, again to represent the stacking of actual deck planks on the stringers. This is illustrated in the rendering in Figure 2.10. Compare the model representation to the deck photographs in Figure 1.2.

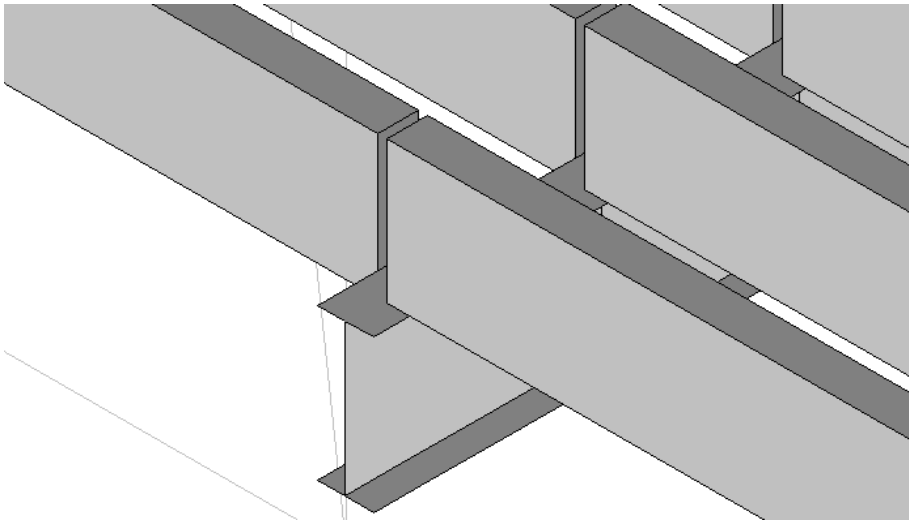

Figure 2.8. Fruita Bridge: Rendering of timber stringers on a steel floor beam. The rendering was produced by RISA 3D.

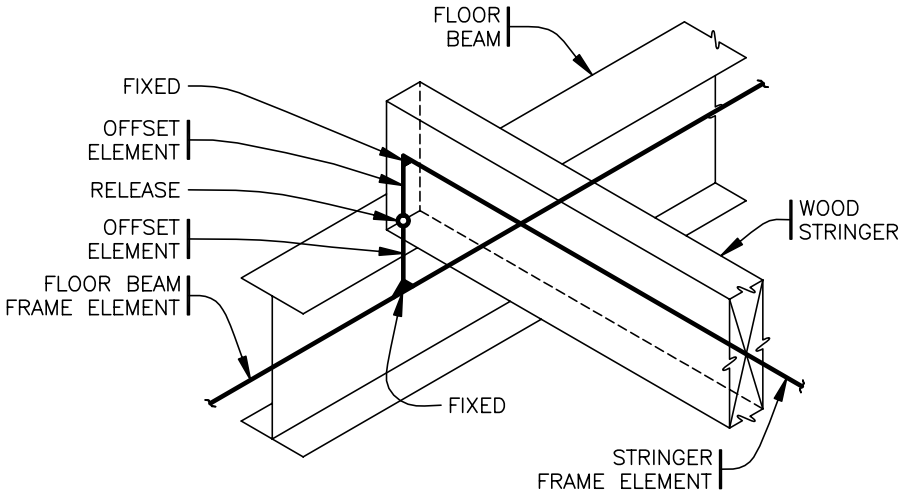


Figure 2.9. Fruita Bridge: Offset members and release location. The rotational release point is located at the intersection of the bottom of the stringer and the top of the floor beam.

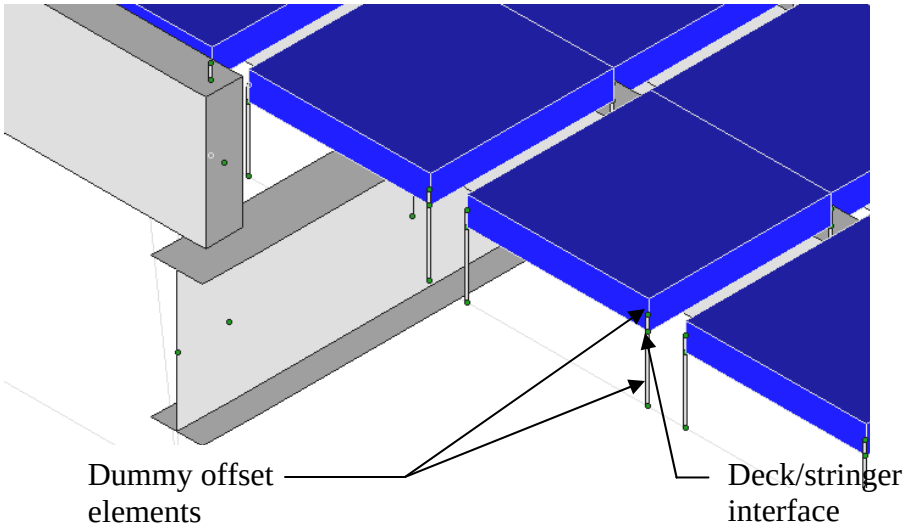


Figure 2.10. Fruita Bridge: Rendering of the timber deck planks on timber stringers on steel floor beam. For clarity, one stringer has been intentionally not shown, although its centerline is shown. Dummy offset elements, from the stringer centerline to the deck/stringer interface and from the deck/stringer interface to the center of the deck plates, can be seen. There is a rotational release at the location of the deck/stringer interface. As with Figure 2.8, the rendering was produced by RISA-3D.

The final case was to treat the deck as a diaphragm, as shown in Figure 2.11, which further reduces the axial forces in the bottom chord eyebars. The axial forces in the bottom chord eyebars under wind are greatly reduced compared to the traditional "skeleton" values, as shown in Table 2.1. This is considered unrealistically stiff in the lateral direction because actual wood decks have gaps between the planks. However, it is presented as a potential lower bound for bottom chord forces.

The results of axial forces in the bottom chord eyebars are summarized in Table 2.1. All models have the same applied loads based on the AASHTO mandated wind pressure.

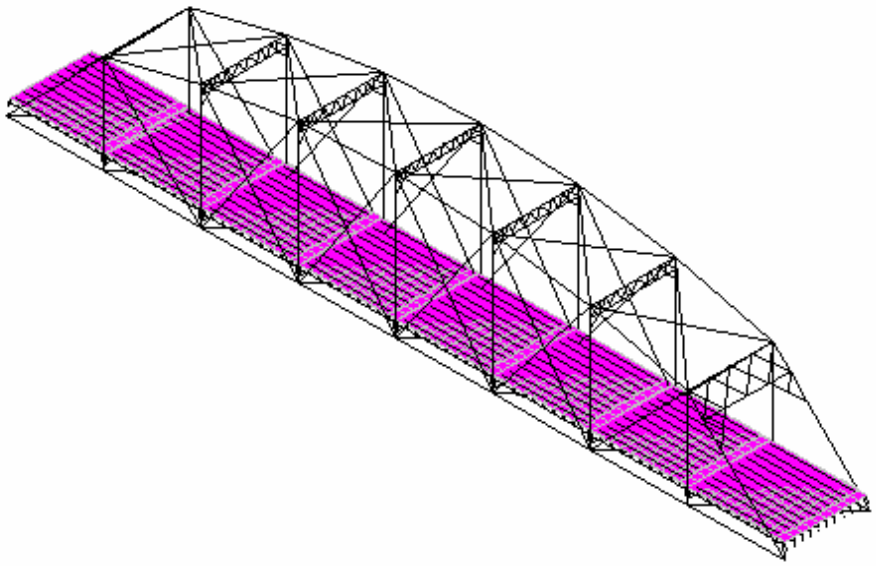

Figure 2.11. Fruita Bridge: The deck treated as a single diaphragm, shown here as part of each bay.

The values with negative signs indicate net compression in the windward bottom chord eyebar sufficient to result in buckling. It is to be noted that use of models of increasing lateral stiffness (Case 2, the deck model) reduce the effect, but do not eliminate compression buckling. Only with Case 3, the (unrealistically stiff) diaphragm deck, does the net force in the windward bottom chord eyebars remain in tension.

Table 2.1. Fruita Bridge: Summary of Maximum Axial Compressive Forces in Bottom Chord Eyebars. Forces are for windward side and are expressed are in kN (kips), followed by percent reduction in compression (or increase in tension) of the traditional skeleton value. (Positive = tension; negative = compression).

| Model | Axial force due to dead load only | Axial force due to wind load only | Net axial force due to wind plus dead load* |
|---|---|---|---|
| Case 1: Skeleton (Figure 2.1) | 149 (33.4) | -320 (-71.9) | -168 (-37.8) |
| Case 2: Deck (Figure 2.7) | 133 (29.6) 11% | -220 (-49.0) 32% | -89.5 (-19.9) 47% |
| Case 3: Diaphragm (Figure 2.11) | 130 (28.8) 14% | -43 (-9.5) 87% | 87 (19.4) 151% |

* Note values are not necessarily identical to (D – W) because tension–only members may not be the same for the (D+W) case as for the individual D or W cases.

The percent change from the skeleton case was determined for the deck model from:

$$\% \text{ change} = 100 \times \left| \frac{F_{skeleton} - F_{deck}}{F_{skeleton}} \right| \tag{2.1}$$

and for the diaphragm model from:

$$\% \text{ change} = 100 \times \left| \frac{F_{skeleton} - F_{diaphragm}}{F_{skeleton}} \right| \tag{2.2}$$

where:

$F_{skeleton}$ = calculated force in windward bottom chord from the skeleton model

$F_{deck}$ = calculated force in windward bottom chord from the deck model

$F_{diaphragm}$ = calculated force in windward bottom chord from the diaphragm model

## 2.3 Prowers Bridge

Prowers Bridge was modeled similarly to Fruita Bridge. Figures 2.12 through 2.20 for Prowers Bridge illustrate the same technique as discussed above for Fruita. Those discussions will not be repeated here.

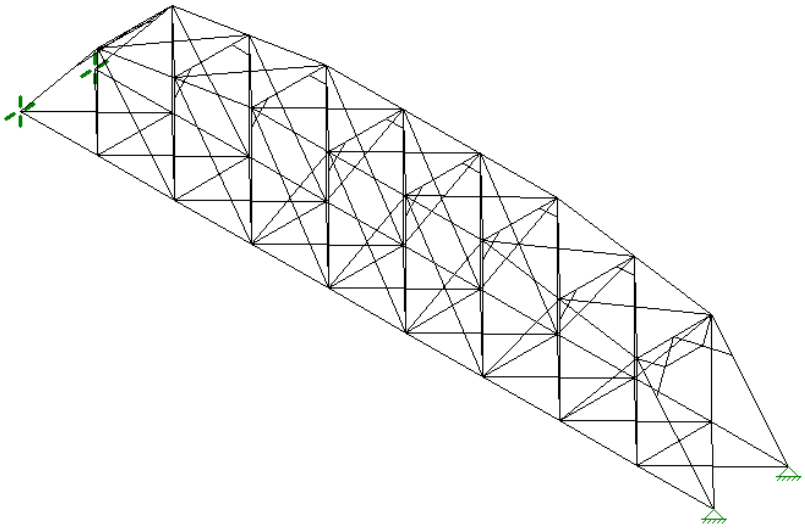

Figure 2.12. Prowers Bridge. Illustration of the traditional skeleton based on the steel members only.

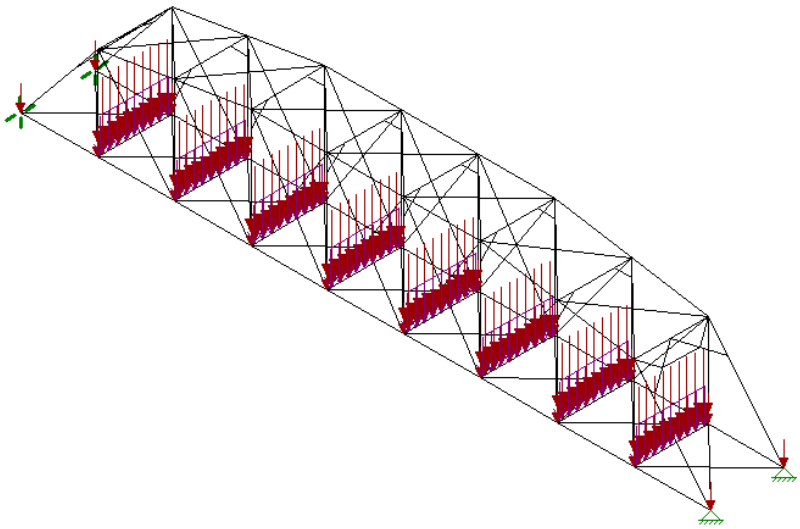

Figure 2.13. Prowers Bridge. Representation of superimposed gravity loads.

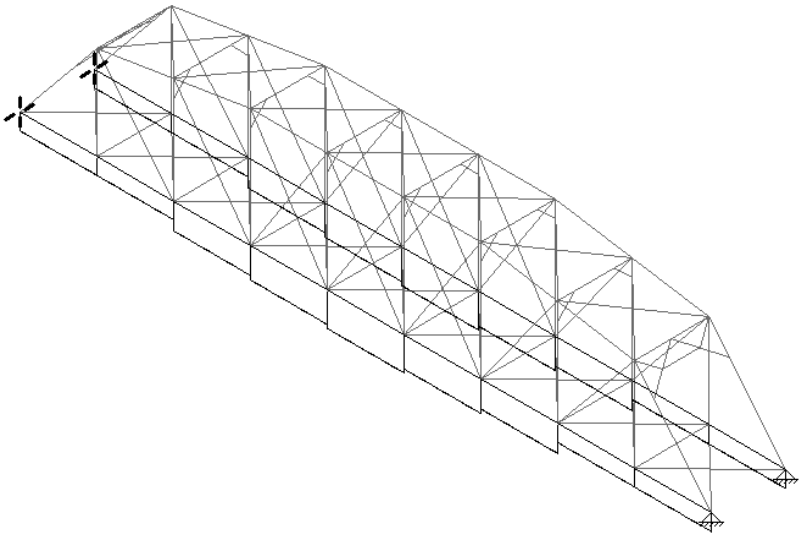

Figure 2.14. Prowers Bridge. Relative axial forces in the bottom chord eyebars due to gravity loads for the skeleton structure.

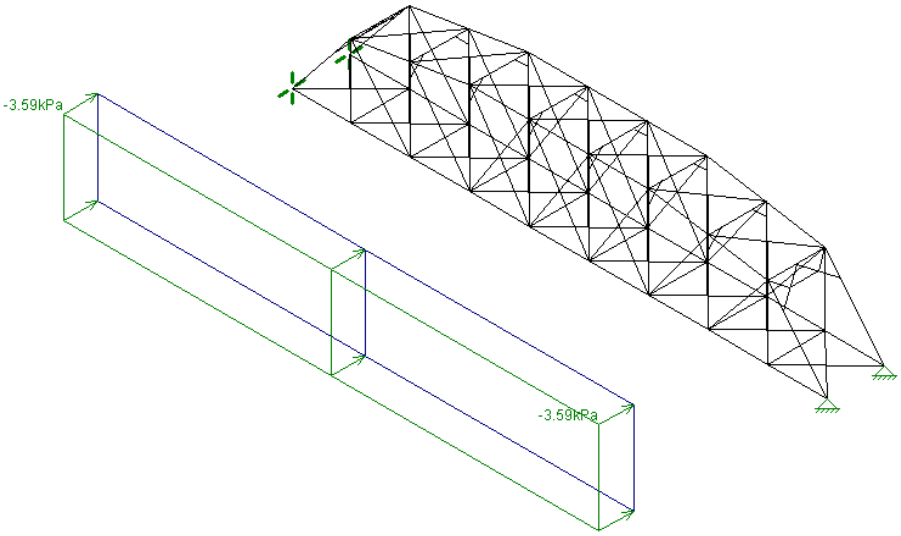


Figure 2.15. Prowers Bridge. Wind Pressure on the bridge.

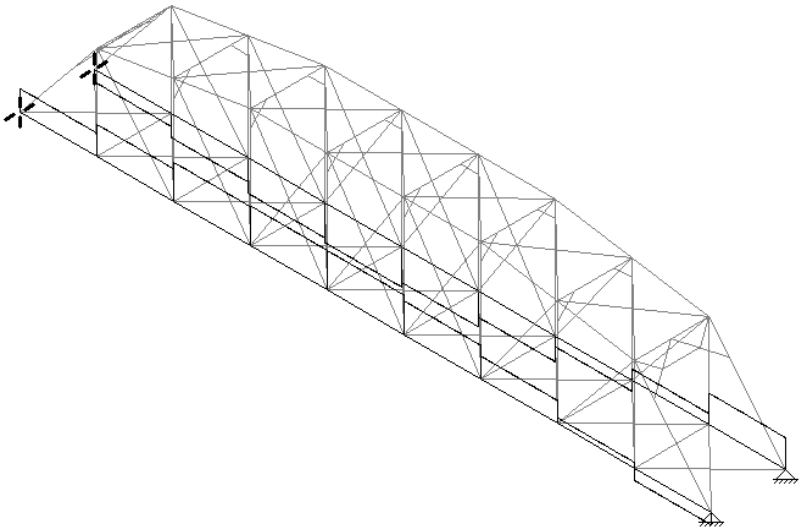

Figure 2.16. Prowers Bridge. Graphical representation of axial forces in the bottom chord eyebars due to wind for the skeleton structure. The reversal in sign occurs near the pinned end, similar to that shown in Figure 2.5 for Fruita Bridge.

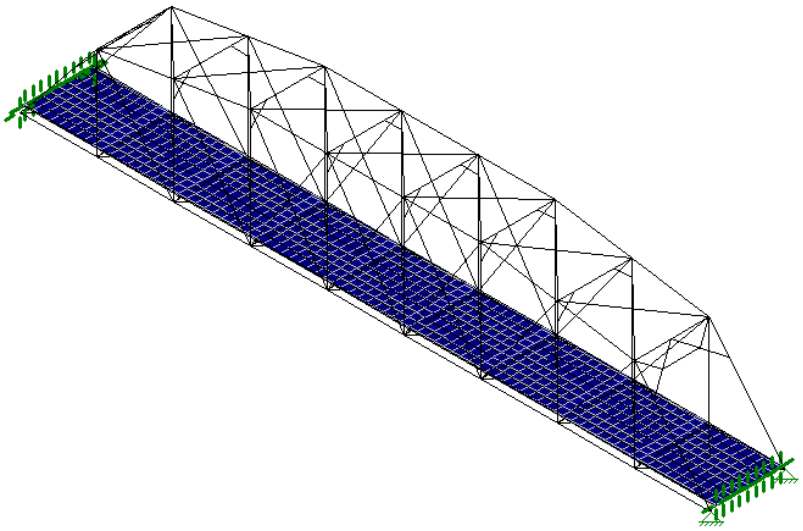

Figure 2.17. Prowers Bridge. Skeleton model with stringers and deck.

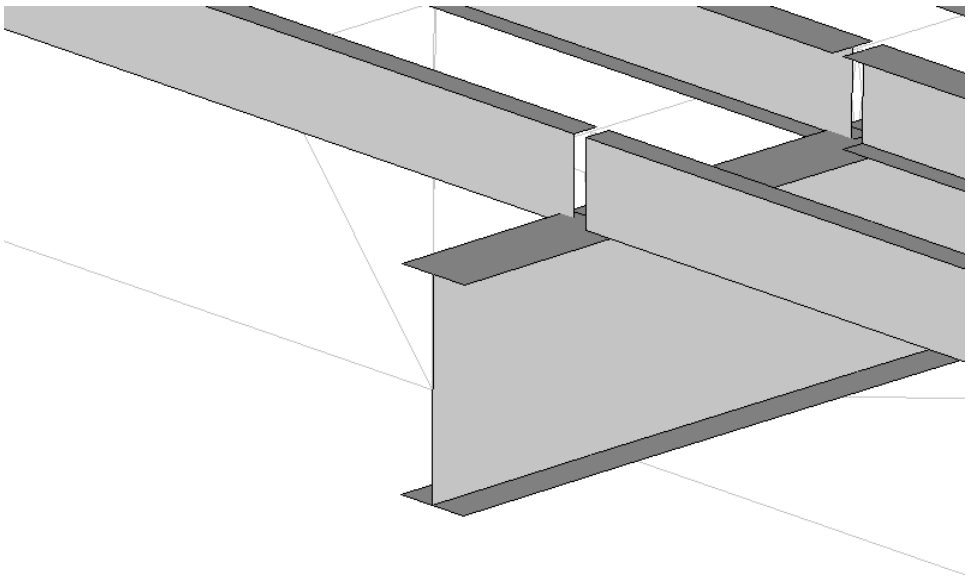

Figure 2.18. Prowers Bridge. Rendering of steel stringers on steel floor beam.

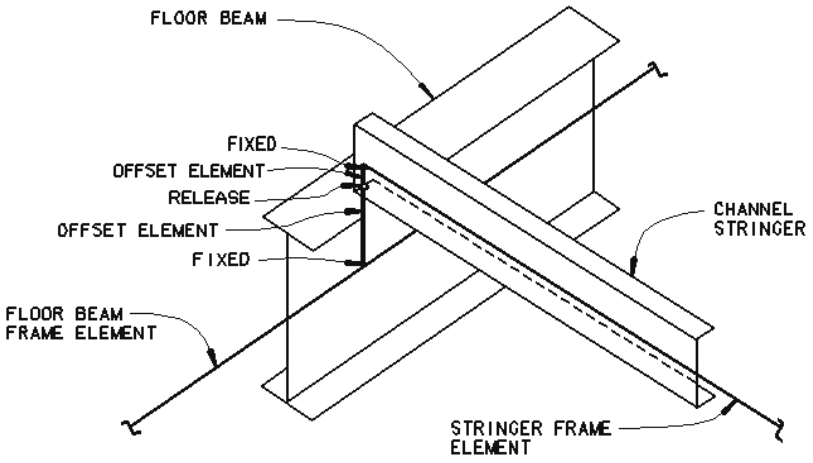


Figure 2.19. Prowers Bridge. Offset members and release locations

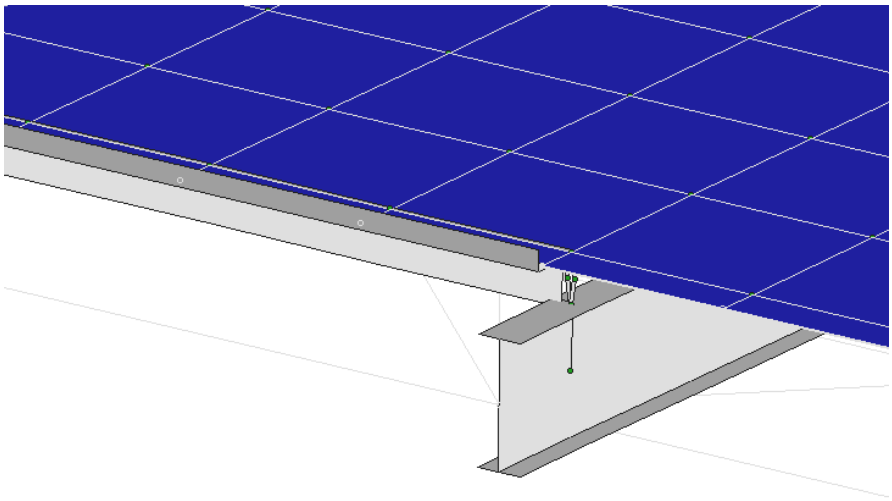

Figure 2.20. Prowers Bridge. Rendering of equivalent corrugated steel deck with deck edge angle on steel stringers on steel floor beam.

Compare modeled representations of Figures 2.18 – 2.20 to the actual deck shown in Figure 1.6. As can be seen by the comparison of the figures, the corrugated metal bridge deck was topped with an asphalt pavement, all of which was modeled as plate elements and shown in Figure 2.20.

Table 2.2. Prowers Bridge: Summary of Maximum Axial Compressive Forces in Bottom Chord Eyebars. Forces are for windward side and are expressed in kN (kips), followed by percent of reduction (or increase in tension) compared to the traditional skeleton value. (Positive = tension; negative = compression).

| Model | Axial force due to dead load only | Axial compression due to wind load only | Net axial force due to wind plus dead load |
|---|---|---|---|
| Case 1: | | | |
| Skeleton | 284.2 | -226.8 | 69.8 |
| (Figure 2.12) | (63.9) | (-51.0) | (15.7) |
| Case 2: | | | |
| Deck | 278.9 | -152.1 | 129.8 |
| (Figure 2.17) | (62.74) | (-34.2) | (29.2) |
| | 1.8% | 32.9% | 86.0% |
| Case 3: | | | |
| Diaphragm | 279.0 | -27.1 | 260.7 |
| | (62.71) | (-6.1) | (58.6) |
| | 1.9% | 88.0% | 272% |

* Note values are not necessarily identical to (D-W) because tension–only members may not be the same for the (D+W) case as for the individual D or W cases.

The percent change from the skeleton case was determined for the deck model from:

$$\% \text{ change} = 100 \times \left| \frac{F_{skeleton} - F_{deck}}{F_{skeleton}} \right| \tag{2.1}$$

and for the diaphragm model from:

$$\% \text{ change} = 100 \times \left| \frac{F_{skeleton} - F_{diaphragm}}{F_{skeleton}} \right| \tag{2.2}$$

where:

$F_{skeleton}$ = calculated force in windward bottom chord from the skeleton model

$F_{deck}$ = calculated force in windward bottom chord from the deck model

$F_{diaphragm}$ = calculated force in windward bottom chord from the diaphragm model

## 2.4 Blue River Bridge

As with Prowers Bridge, Blue River Bridge, shown in Figures 2.21 through 2.29, was modeled similarly to Fruita Bridge. Figures for Blue Bridge illustrate the same technique as discussed above for Fruita. Those discussions will not be repeated here.

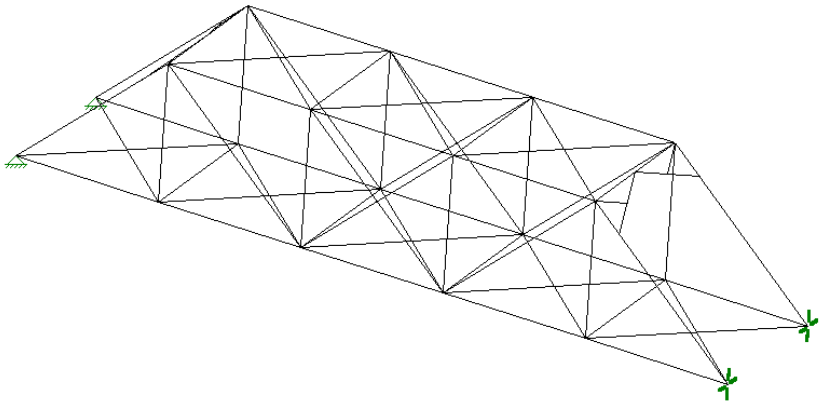

Figure 2.21. Blue River Bridge: Illustrating the traditional skeleton based on the primary members only.

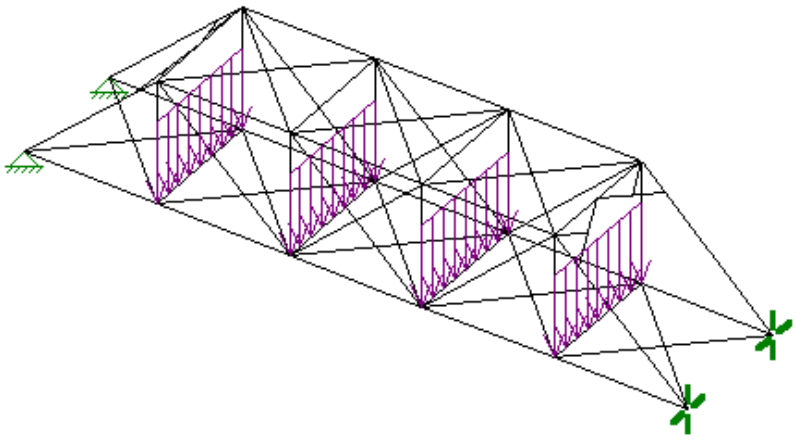

Fig. 2.22. Blue River Bridge: Representation of superimposed gravity loads.

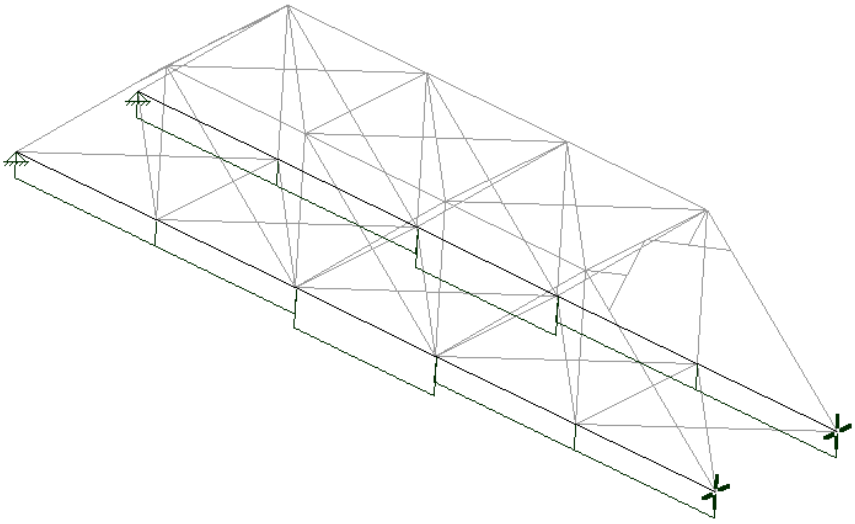

Figure 2.23. Blue River Bridge: Relative axial forces in the bottom chord eyebars due to gravity loads for the skeleton structure.

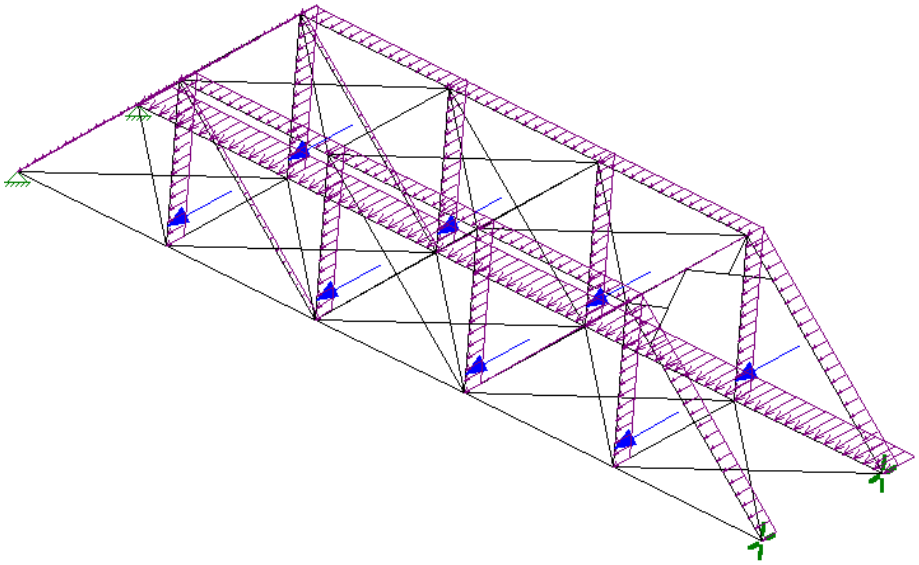

Figure 2.24. Blue River Bridge: Wind pressure on the bridge.

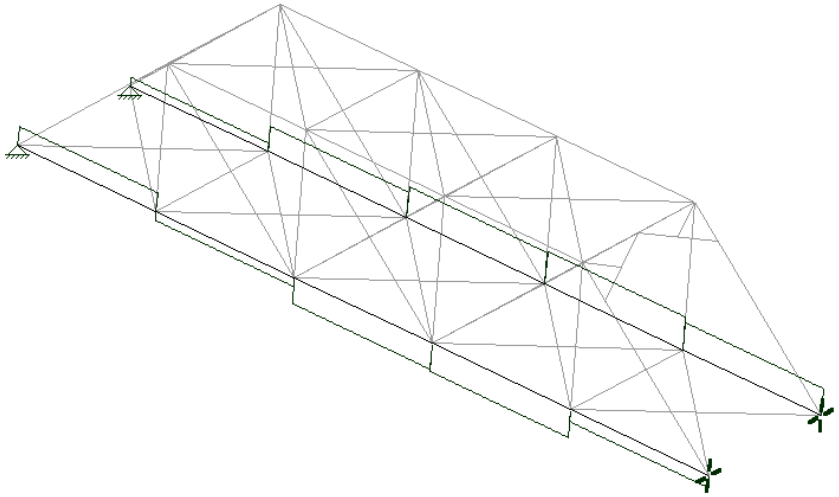

Figure 2.25. Blue River Bridge: Graphical representation of axial forces in the bottom chord eyebars due to wind for the skeleton structure. The reversal in sign occurs near the pinned end, similar to that shown for Fruita Bridge in Figure 2.5.

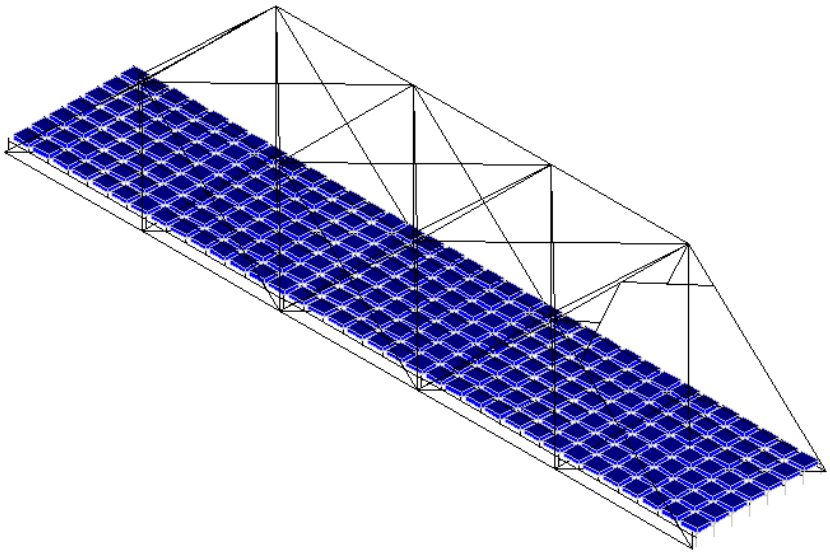

Figure 2.26. Blue River Bridge: Skeleton model with stringers and deck.

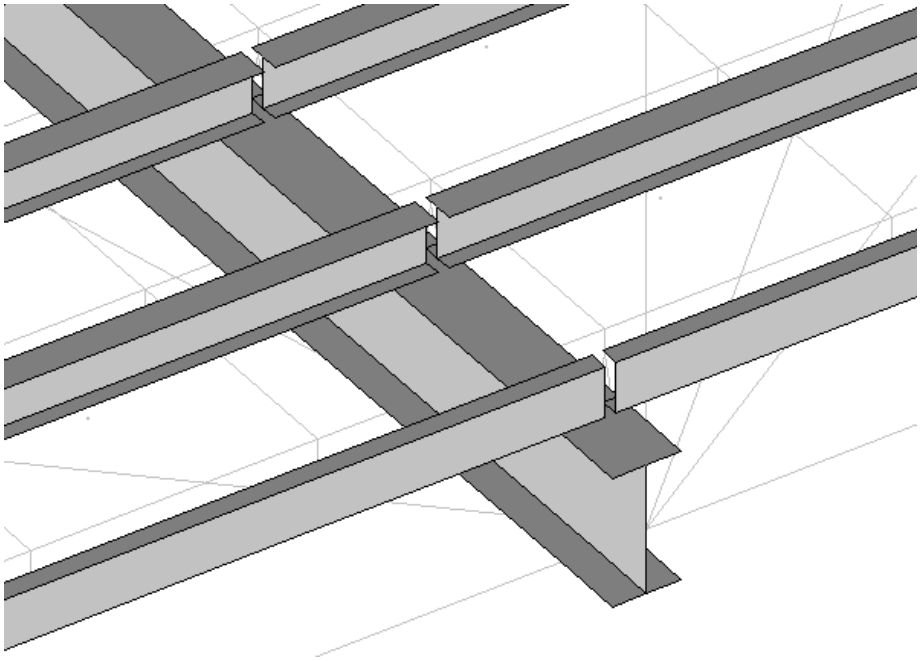

Figure 2.27. Blue River Bridge. Rendering of steel stringers on steel floor beam.

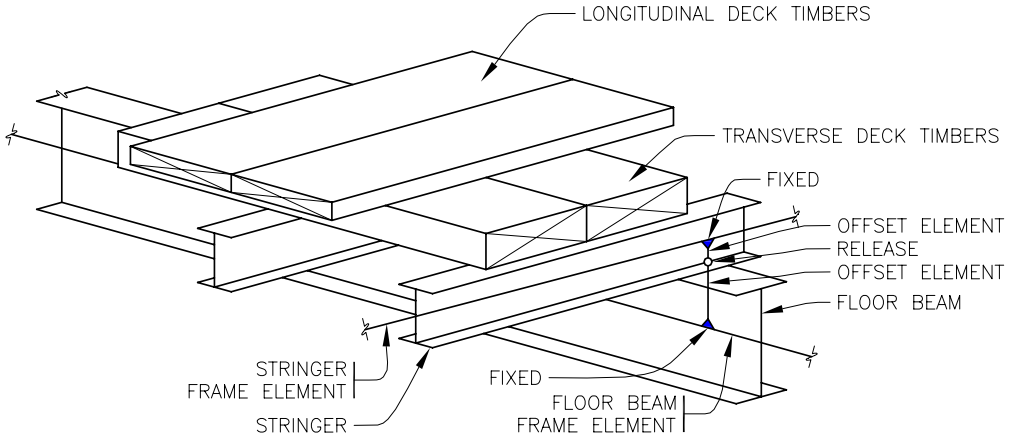


Figure 2.28. Blue River Bridge. Offset members and release locations.

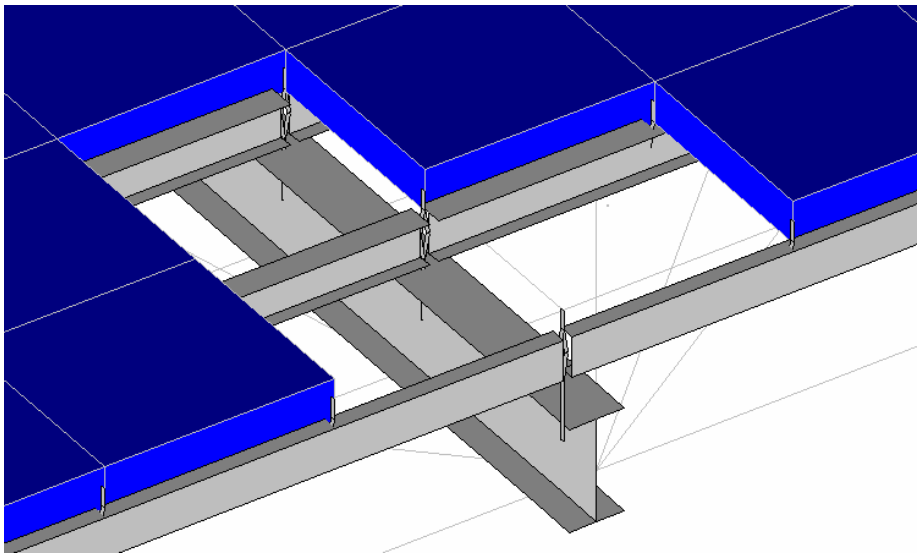

Figure 2.29. Blue River Bridge: Rendering of deck timber deck on steel stringers on steel floor beam. The mutually orthogonally deck timbers have been treated as a single monolithic solid.

Compare the model representations for Blue River Bridge shown in Figures 2.27 –2.29 to the actual deck shown in Figure 1.8. The transverse deck boards and the longitudinal running boards oriented perpendicular to them were treated as a solid instead of as individual boards. This was because the two mutually perpendicular layers, well spiked together, were believed to act similar to a single solid material. As such, this timber deck was considerably stiffer in the lateral direction than the deck at Fruita Bridge.

Table 2.3. Blue River Bridge: Summary of Maximum Axial Compressive Forces in Bottom Chord Eyebars. Forces are for windward side and are expressed are in kN (kips), followed by percent reduction in compression (or increase in tension) compared to the traditional skeleton value. (Positive = tension; negative = compression). Note the deck and diaphragm values are virtually identical, suggesting the deck, as modeled, is about as stiff as possible.

| Model | Axial force due to dead load only | Axial compression due to wind load only | Net axial force due to wind plus dead load* |
|---|---|---|---|
| Case 1: | | | |
| Skeleton | 57 | -60 | -1.4 |
| (Figure 26) | (12.6) | (-13.3) | (-0.3) |
| | | | |
| Case 2: | | | |
| Deck | 56 | -50 | 9.4 |
| (Figure 31) | (12.5) | (-11.2) | (2.1) |
| | 1% | 16% | 600% |
| Case 3: | | | |
| Diaphragm | 56 | -46 | 13.2 |
| | (12.5) | (-10.4) | (3.0) |
| | 1% | 22% | 900% |

* Note values are not necessarily identical to (D-W) because tension–only members may not be the same for the (D+W) case as for the individual D or W cases.

The percent change from the skeleton case was determined for the deck model from:

$$\% \text{ change} = 100 \times \left| \frac{F_{skeleton} - F_{deck}}{F_{skeleton}} \right| \tag{2.1}$$

and for the diaphragm model from:

$$\% \text{ change} = 100 \times \left| \frac{F_{skeleton} - F_{diaphragm}}{F_{skeleton}} \right| \tag{2.2}$$

where:

$F_{skeleton}$ = calculated force in windward bottom chord from the skeleton model

$F_{deck}$ = calculated force in windward bottom chord from the deck model

$F_{diaphragm}$ = calculated force in windward bottom chord from the diaphragm model

## 2.5 San Miguel Bridge

As with Prowers Bridge and Blue River Bridge, San Miguel Bridge as shown in Figures 2.30 through 2.38 was modeled similarly to Fruita Bridge. Figures for San Miguel Bridge illustrate the same technique as discussed above for Fruita. Those discussions will not be repeated here.

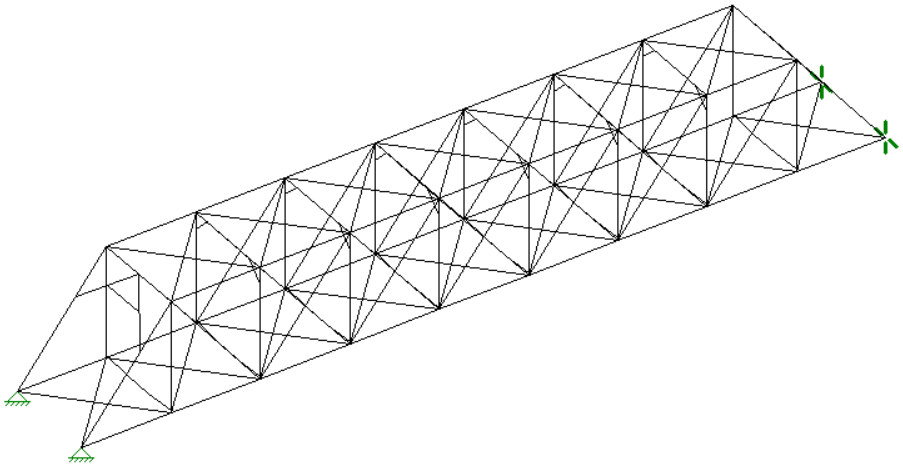

Figure 2.30. San Miguel Bridge: Illustration of the traditional of skeleton structure based on steel members only.

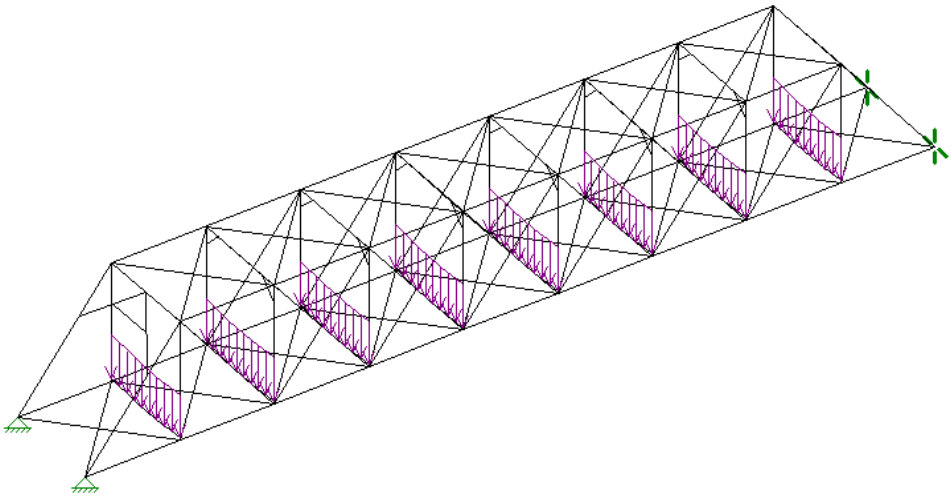

Figure 2.31. San Miguel Bridge: Gravity loads applied to skeleton structure.

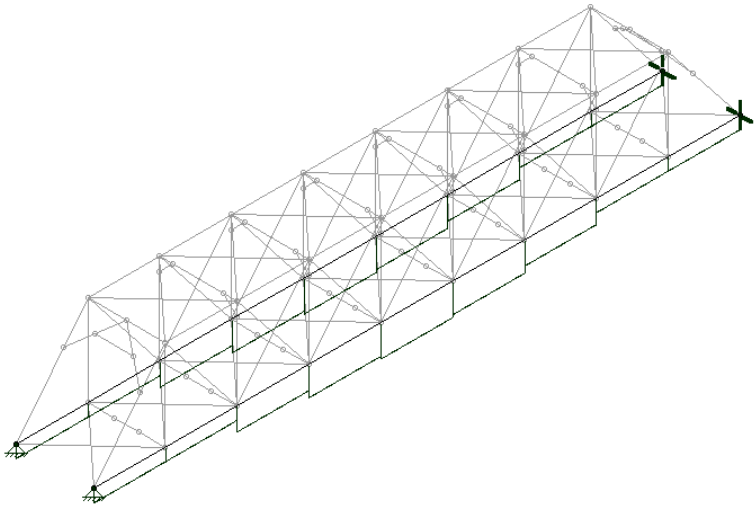

Figure 2.32. San Miguel Bridge: Diagram of axial force in bottom chords due to gravity loads for the skeleton structure.

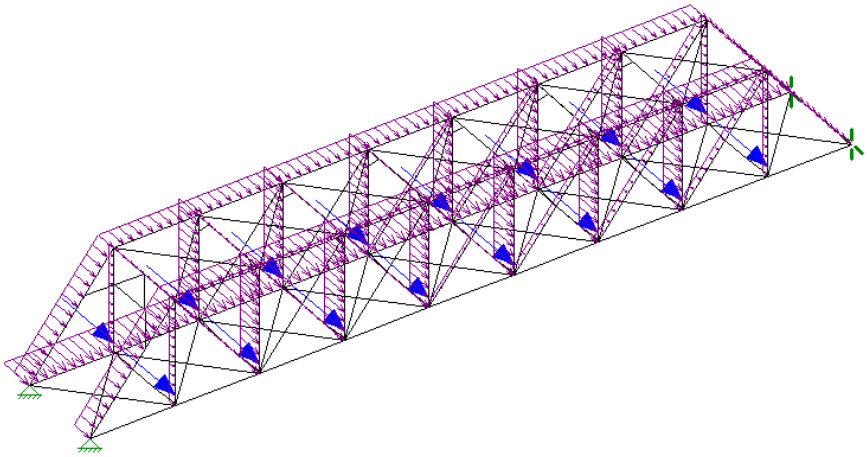

Figure 2.33. San Miguel Bridge: Wind load applied to skeleton structure.

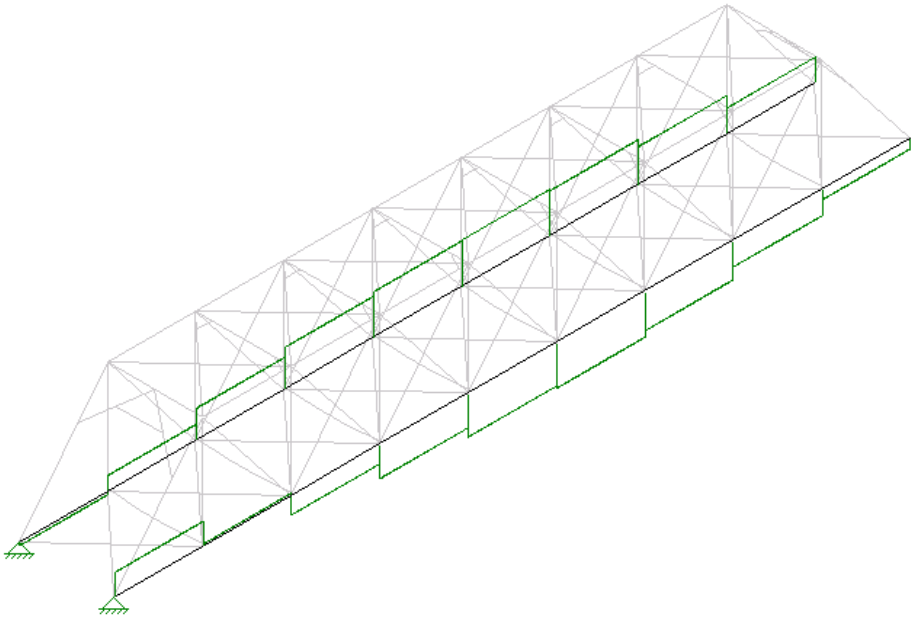

Figure 2.34. San Miguel Bridge: Diagram of axial force in bottom chords due to wind load. The reversal in sign occurs near the pinned end, similar to that shown in Figure 2.5 for Fruita Bridge.

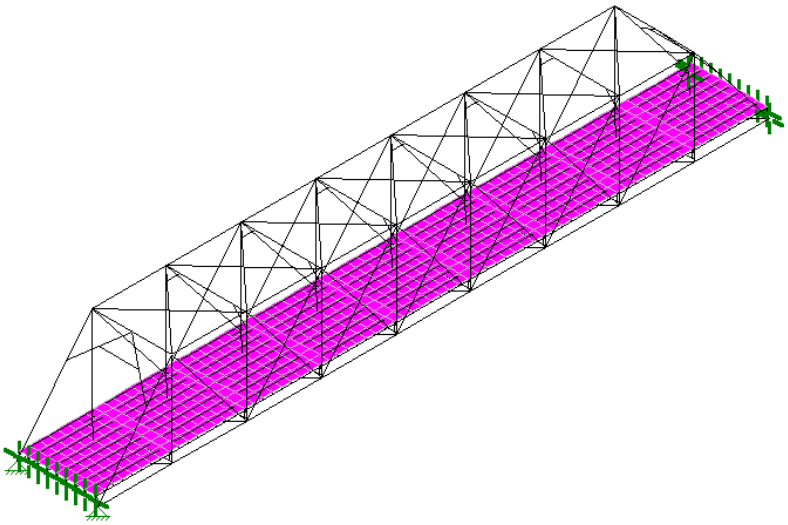

Figure 2.35. San Miguel Bridge: Skeleton model with stringers and deck.

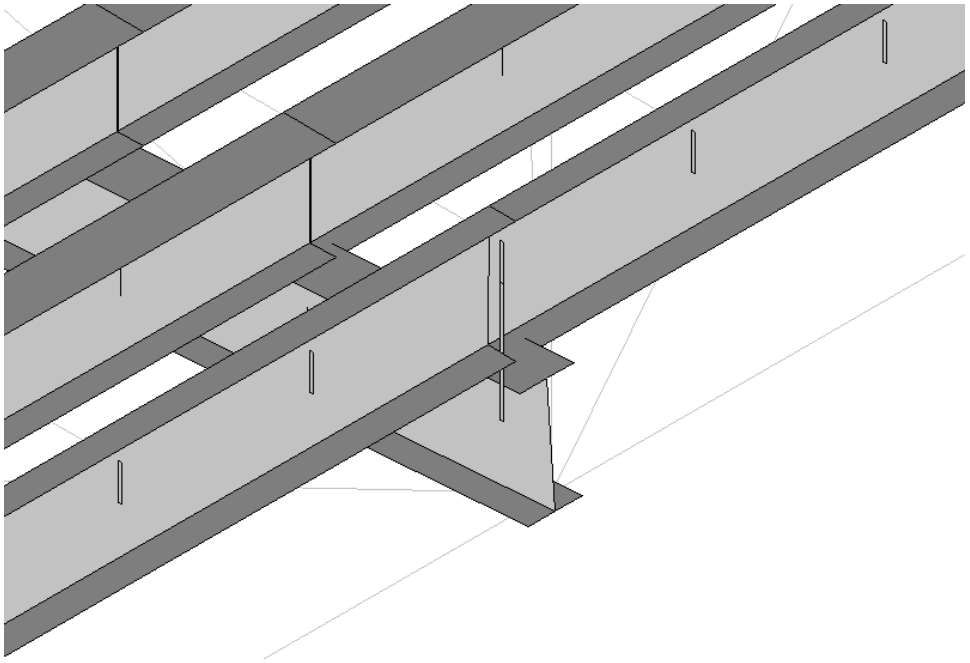

Figure 2.36. San Miguel Bridge: Rendering of Floor beam and stringers. The interior stringers are 12 inch deep wide flange beams while the outer stringer is a 15 inch deep channel, all of which is intended to model the floor system that was installed in 1964.

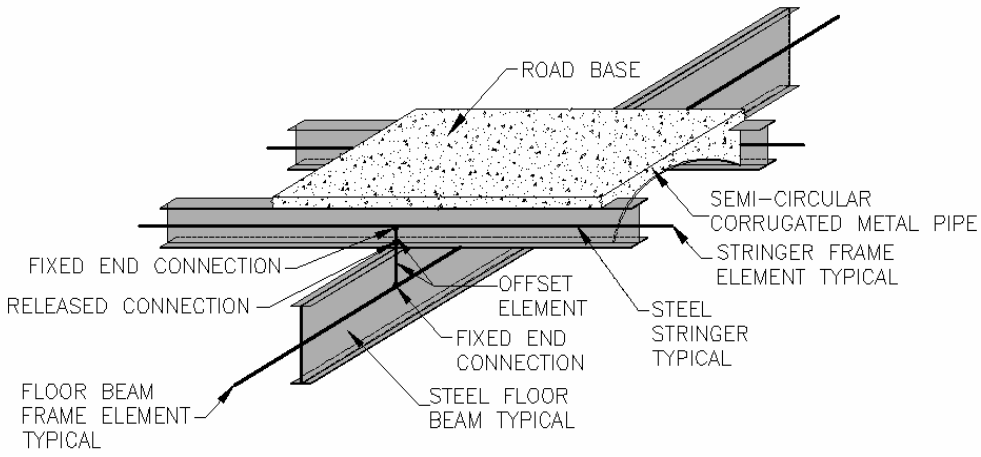


Figure 2.37. San Miguel Bridge: Offset members and release locations.

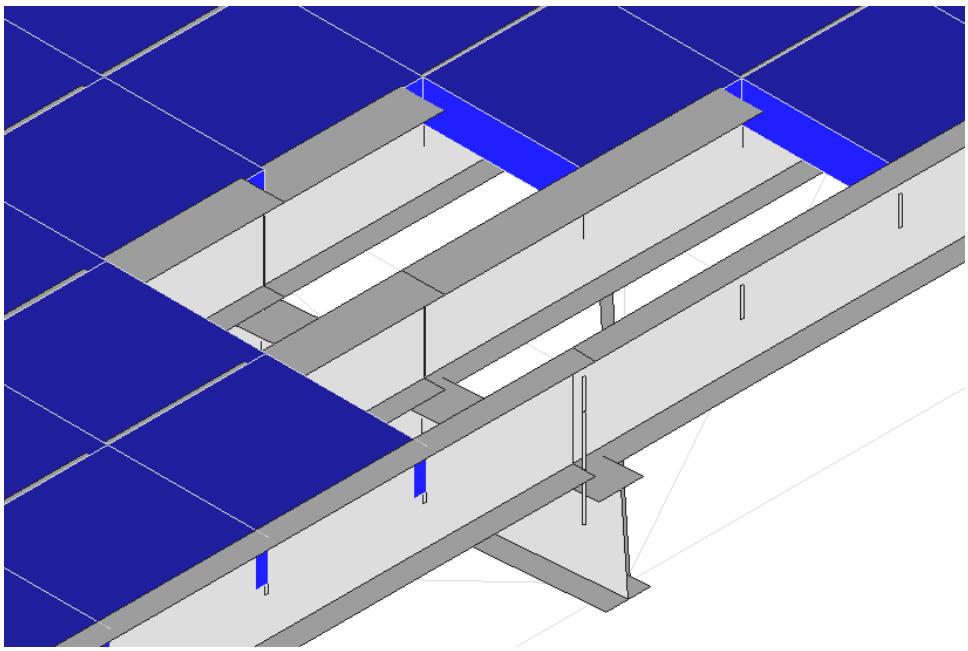

Figure 2.38. San Miguel Bridge: Rendering of floor beam, stringers, and deck. Note that the deck is represented as centered on the top flange of the stringers, intended to approximate the actual roadbase material, which envelops the stringer top flanges.

Compare the model representations shown in Figures 2.36 – 2.38 to the actual deck shown in Figure 1.10. Note the gravel roadbase and the semicircular corrugated metal pipe segments which support it were modeled as an elastic solid that enveloped the top flange of the stringers, as shown in Figure 2.38.

The San Miguel Bridge deck, with its large amount of gravel roadbase, has an unusually heavy dead load. Dead load due to the gravel is approximately 75 psf, much higher than any of the other decks in the study. It is clearly much higher than the original (1886) timber deck.

Table 2.4. San Miguel Bridge: Summary of Maximum Axial Compressive Forces in Bottom Chord Eyebars. Forces are for windward side and are expressed in kN (kips), followed by percent reduction (or increase in tension) compared to the traditional skeleton value. (Positive = tension; negative = compression).

| Model | Axial force due to dead load only | Axial compression due to wind load only | Net axial force due to wind plus dead load* |
|---|---|---|---|
| Case 1: Skeleton (Figure 2.30) | 399 (89.7) | -222 (-49.9) | 180 (40.5) |
| Case 2: Deck (Figure 2.35) | 317 (71) 21% | -105 (-23.7) 53% | 209 (46.9) 16% |
| Case 3: Diaphragm | 316 (71.1) 21% | -32.1 (-7.2) 86% | 292 (65.6) 62% |

* Note values are not necessarily identical to (D-W) because tension–only members may not be the same for the (D+W) case as for the individual D or W cases.

The percent change from the skeleton case was determined for the deck model from:

$$\% \text{ change} = 100 \times \left| \frac{F_{skeleton} - F_{deck}}{F_{skeleton}} \right| \quad (2.1)$$

and for the diaphragm model from:

$$\% \text{ change} = 100 \times \left| \frac{F_{skeleton} - F_{diaphragm}}{F_{skeleton}} \right| \quad (2.2)$$

where:

$F_{skeleton}$ = calculated force in windward bottom chord from the skeleton model

$F_{deck}$ = calculated force in windward bottom chord from the deck model

$F_{diaphragm}$ = calculated force in windward bottom chord from the diaphragm model

## 2.6 Rifle Bridge

Unlike the other four bridges in this study, the Rifle bridge was analyzed using RAM Advanse software (RAM 2005). RAM Advanse is similar to RISA 3D in that it is a tool that is readily available to engineers. Other 3D structural analysis software is also available. The Rifle Bridge was modeled as shown in Figures 2.39 through 2.46.

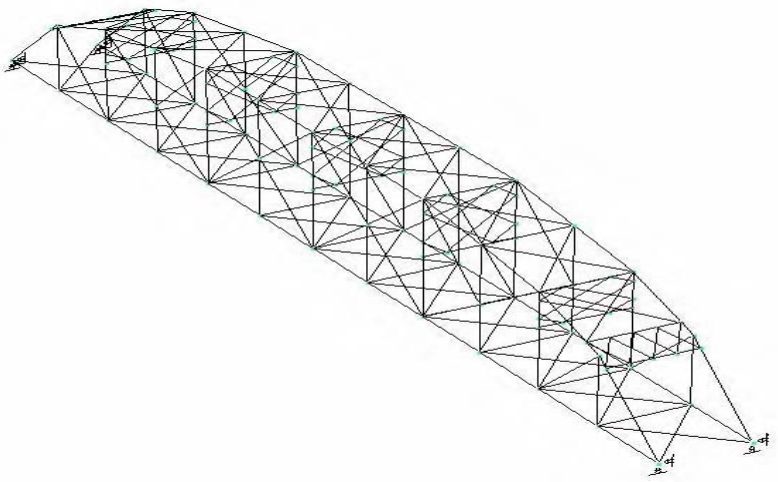

Figure 2.39. 3D model of the Rifle Bridge, illustrating the traditional skeleton based on the steel members only. The 3D structural engineering software RAM Advanse was used for this bridge.

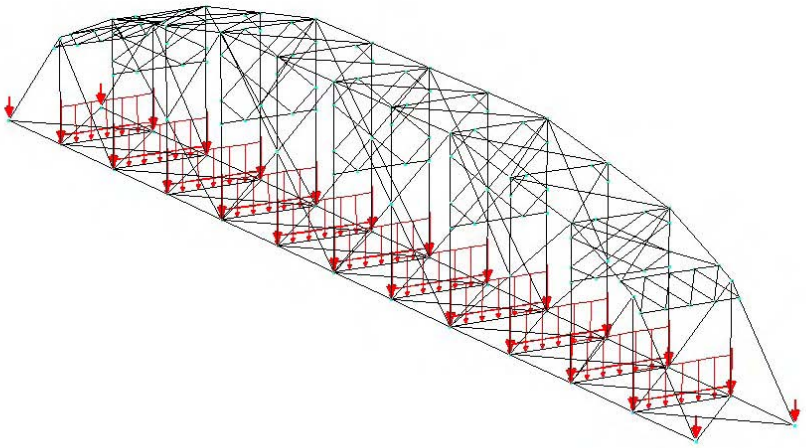

Figure 2.40. Rifle Bridge: Representation of superimposed gravity loads (D + L).

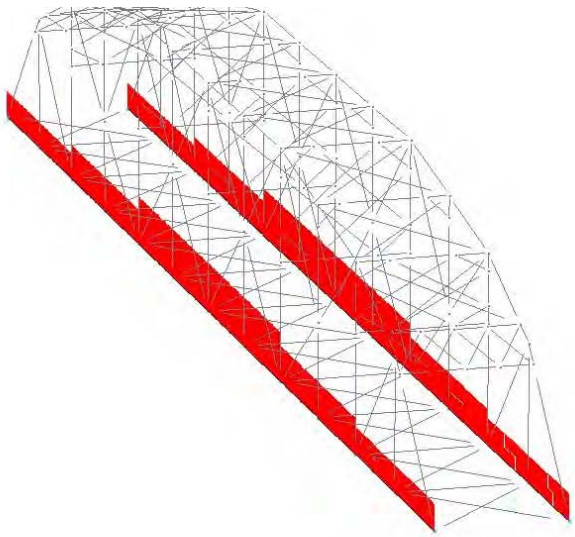

Figure 2.41. Rifle Bridge: Relative axial forces in the bottom chord eyebars due to gravity loads for the skeleton structure.

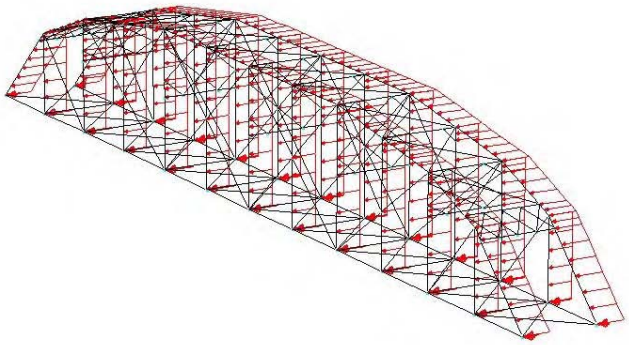

Figure 2.42. Rifle Bridge: Representation of wind pressure on the bridge.

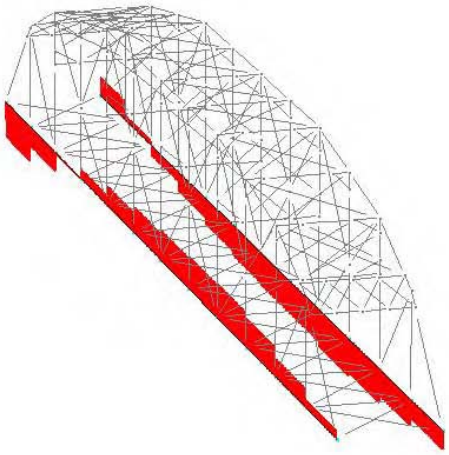

Figure 2.43. Rifle Bridge: Graphical representation of axial forces in the bottom chord eyebars due to wind for the skeleton structure. Note the reversal in sign for the bottom chords near the pinned ends.

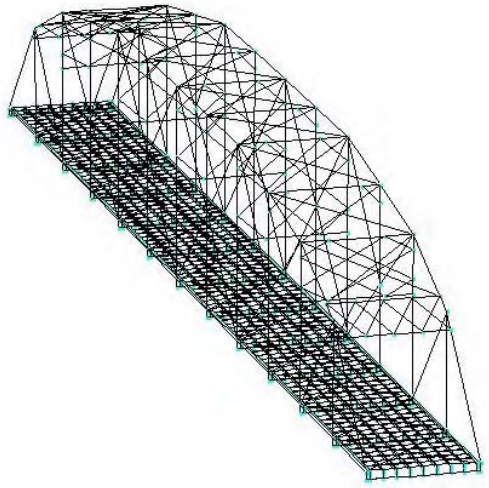

Figure 2.44. Rifle Bridge: Skeleton model with stringers and deck

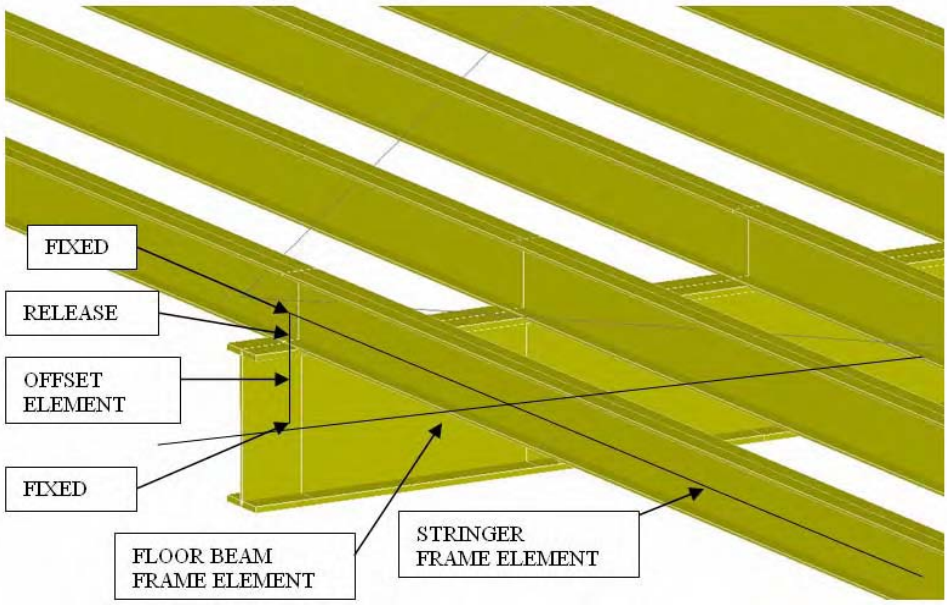


Figure 2.45. Rifle Bridge: Rendering of stringers on a steel floor beam. The rendering was produced by RAM Advanse 3D. The dummy offset elements used to connect the floor beam and stringer have a rotational release at the beam-to-stringer interface.

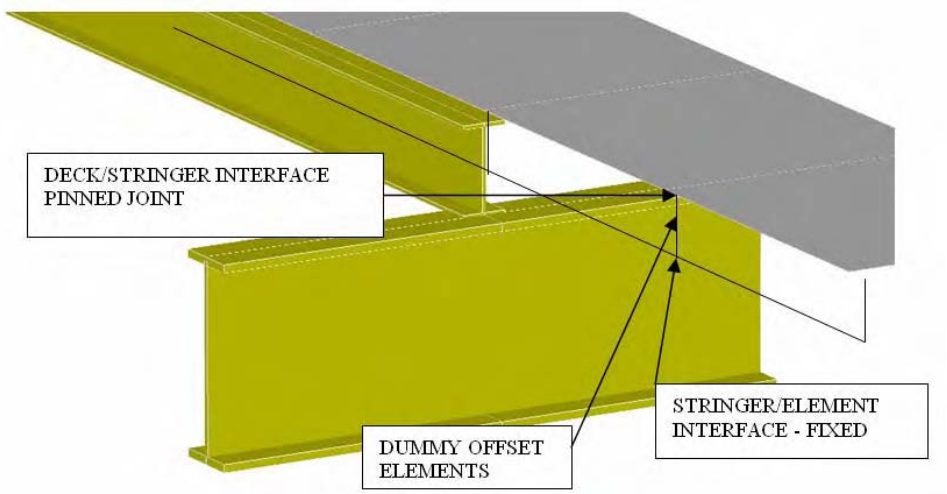


Figure 2.46. Rifle Bridge: Rendering of the 2" asphalt paving over 2.25" steel deck planks on steel floor beam. For clarity, near stringers have been intentionally not shown. Offset elements, from the beam centerline to the beam/stringer intersection to the stringer centerline to the deck/stringer interface were used. The rendering was produced by RAM Advanse.

Compare the modeled representations of Figures 2.45 and 2.46 to the actual deck shown in Figure 1.13. As can be seen by the comparison of the figures, the corrugated metal bridge deck was topped with an asphalt pavement, all of which was modeled as plate elements – shown in Figure 2.46.

Table 2.5. Rifle Bridge. Summary of Maximum Axial Compressive Forces in Bottom Chord Eyebars. Forces are for windward side and are expressed in kN (kips), followed by percent reduction (or increase in tension) compared to the traditional skeleton value. (Positive = tension; negative = compression).

| Model | Axial force due to dead load only | Axial force on windward side due to wind load only | Net axial force due to wind plus dead load* |
|---|---|---|---|
| Case 1: Skeleton (Figure 2.39) | 572 (129) | -565 (-127) | 23 (5.2) |
| Case 2: Deck (Figure 2.44) | 551 (124) 4% | -342 (-77) 40% | 203 (46) 777% |
| Case 3: Diaphragm | 541 (122) 2% | -151 (-34) 56% | 388 (87) 1579% |

* Note values are not necessarily identical to (D-W) because tension–only members may not be the same for the (D+W) case as for the individual D or W cases.

The percent change from the skeleton case was determined for the deck model from:

$$\% \text{ change} = 100 \times \left| \frac{F_{skeleton} - F_{deck}}{F_{skeleton}} \right| \quad (2.1)$$

and for the diaphragm model from:

$$\% \text{ change} = 100 \times \left| \frac{F_{skeleton} - F_{diaphragm}}{F_{skeleton}} \right| \quad (2.2)$$

where:

$F_{skeleton}$ = calculated force in windward bottom chord from the skeleton model

$F_{deck}$ = calculated force in windward bottom chord from the deck model

$F_{diaphragm}$ = calculated force in windward bottom chord from the diaphragm model

## 2.7 Conclusions

In the foregoing, the alternative load path of the deck as a lateral diaphragm has been introduced. It is concluded that the combination of "skeleton" plus plus deck stiffens the bridge in the lateral direction, resulting in a significant reduction of axial forces in the bottom chord eyebars compared to those calculated using a traditional "skeleton" model. The results for the five bridges are summarized in Table 2.6.

Table 2.6. Summary of Net Axial Force due to Wind Plus Dead Load in Bottom Chord. Forces are for windward side and are expressed are in kN (kips), followed by percent reduction in compression (or increase in tension) compared to the traditional skeleton value.

| Bridge | Skeleton Model | Deck Model | Diaphragm Model |
|---|---|---|---|
| Fruita | -168 (-37.8) | -90 (-19.9) | 87 (19.4) |
| Prowers | 70 (15.7) | 130 (29.2) | 261 (58.6) |
| Blue River | 1.4 (0.3) | 9.4 (2.1) | 13.2 (3.0) |
| San Miguel | 180 (40.5) | 209 (46.9) | 292 (65.6) |
| Rifle | 23 (5.2) | 203 (46) | 388 (87.0) |

Historically, these bridges were built with timber decks. The Fruita Bridge still has a timber deck (a replacement) in its original configuration. Blue River Bridge has longitudinal running boards added to its original deck configuration. The other bridges have replacement decks, all heavier than the original timber deck. Deck loads are summarized in Table 2.7.

Table 2.7. Deck Dead Load. Both an estimate of the original timber deck plus stringers dead load and the dead load of the existing (as-built) deck plus stringers is listed.

| Bridge | Timber DL | Existing DL |
|---|---|---|
| Fruita | 733 Pa (15 psf) | 733 Pa (15 psf) |
| Blue River | 733 Pa (15 psf) | 833 Pa (17 psf) |
| Rifle | 733 Pa (15 psf) | 1915 Pa (40 psf) |
| Prowers | 733 Pa (15 psf) | 2346 Pa (49 psf) |
| San Miguel | 733 Pa (15 psf) | 3543 Pa (74 psf) |

For deck models, the bridges with heavier decks have both windward and leeward bottom chords in tension, even when wind is included in the load combination. However, for skeleton models with assumed original (timber) decks, all of the bridges, even those with heavy decks, have bottom chord compression on the windward side. The results are listed in Table 2.8.

Table 2.8. Windward Bottom Chord Force for Original Timber Deck and Existing Deck. All values are from Skeleton models.

| Bridge | Bottom Chord Force - Timber Deck | Bottom Chord Force – Existing (As-Built) Deck |
|---|---|---|
| Fruita | -168 kN (-38 k) | -168 kN (-38 k) |
| Blue River | -6 kN (-1 k) | 1.4 kN (0.3 k) |
| Rifle | -197 kN (-43 k) | 23 kN (5 k) |
| Prowers | -136 kN (-30 k) | 70 kN (16 k) |
| San Miguel | -198 kN (-44 k) | 180 kN (41 ) |

The following graphs examine the case of axial force in the mid-span bottom chord on the windward side. The results from the skeleton, deck, and diaphragm models for all five bridges are examined.

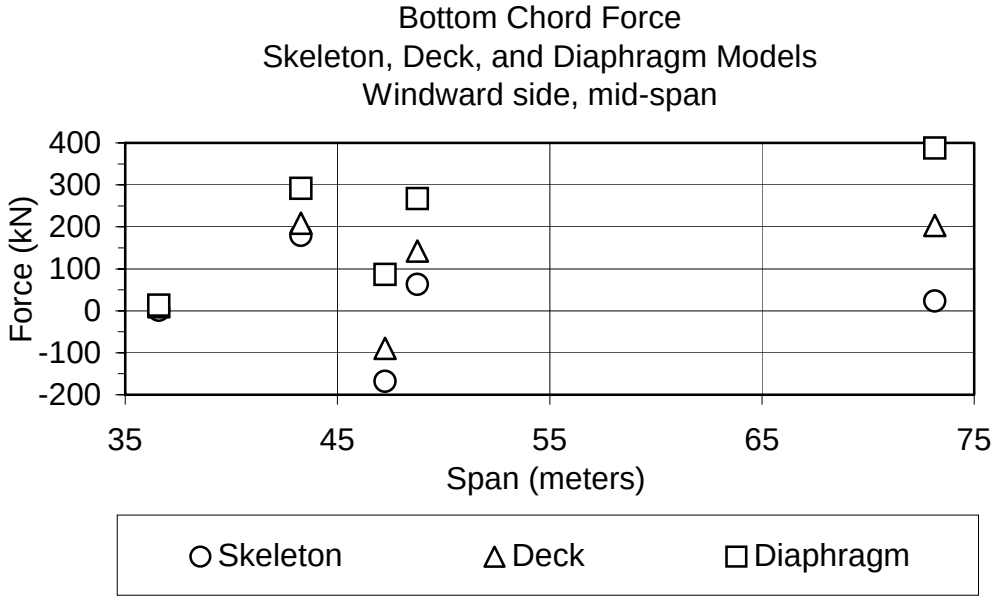


Figure 2.47. Windward Bottom Chord Force vs. Span. The spans are:
Blue River: 36.6 m.(120 ft.)
San Miguel: 43.3 m.(142 ft.)
Fruita: 47.2 m.(155 ft.)
Prowers: 48.2 m.(160 ft.)
Rifle:73.2 m.(240 ft.)

No particular correlation is observed in Figure 2.47, therefore it was concluded that (D+W) force in bottom chords is independent of span.

However, as is seen in Figures 2.48 – 2.51, there is was correlation between force in the windward bottom chords due to (D+W) and dead load of the deck/stringer system.

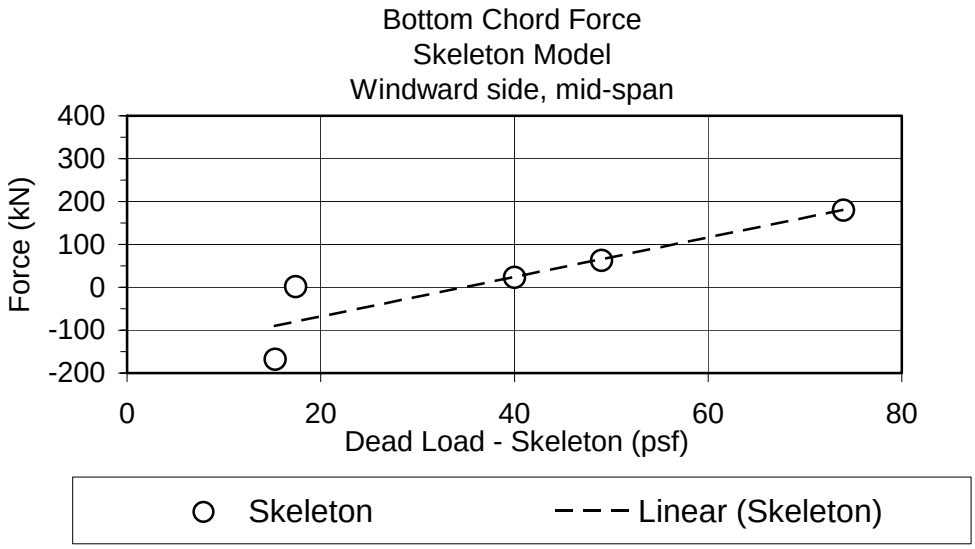


Figure 2.48. Force vs. Deck Dead Load for skeleton models shows a relationship. High deck dead loads have high bottom chord forces. A linear regression curve for the skeleton data is shown.

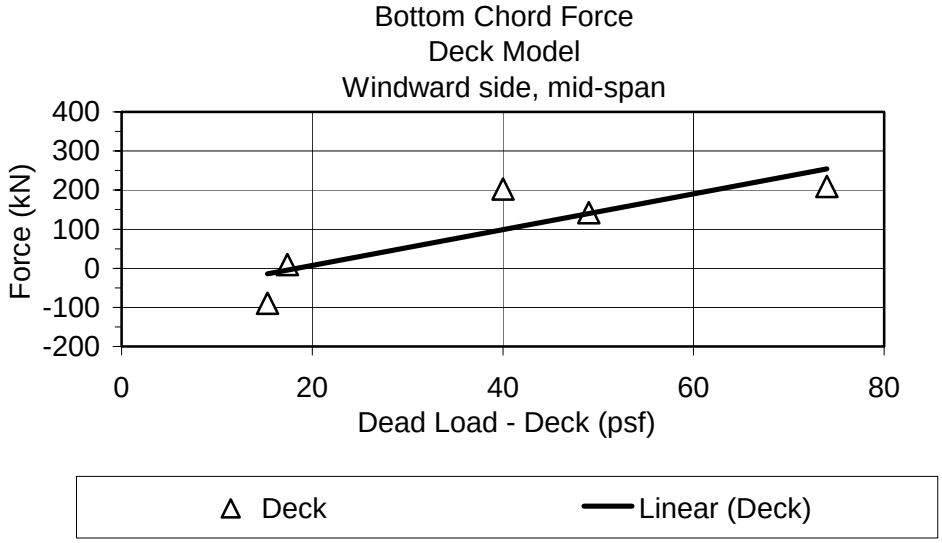


Figure 2.49. Force vs. Deck Dead Load for deck models shows a relationship similar to Figure 2.48. A linear regression curve for the deck data is shown.

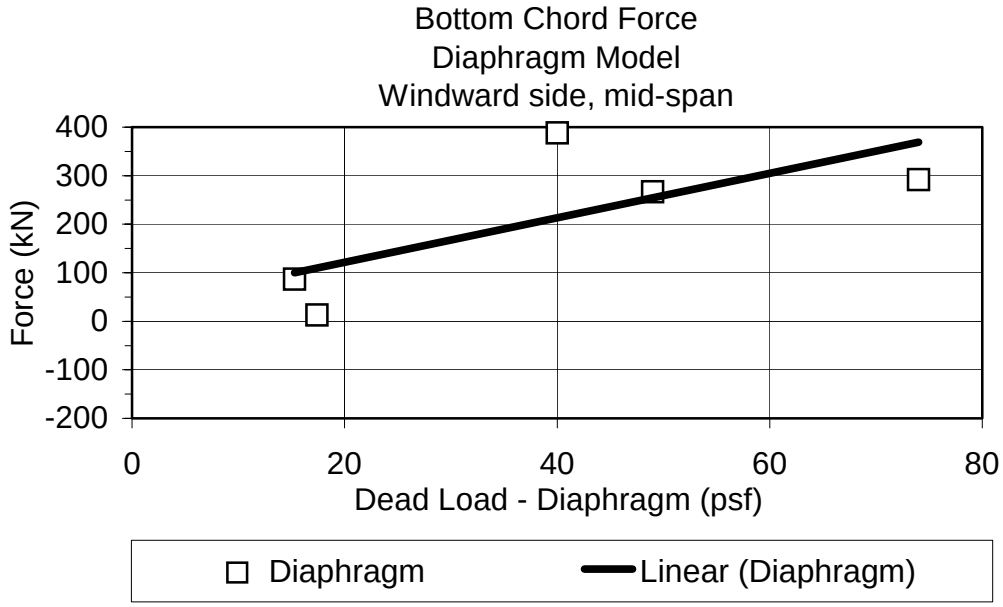


Figure 2.50. Force vs. Deck Dead Load for diaphragm models shows a relationship similar to Figure 2.48 and Figure 2.49. A linear regression curve for the deck data is shown.

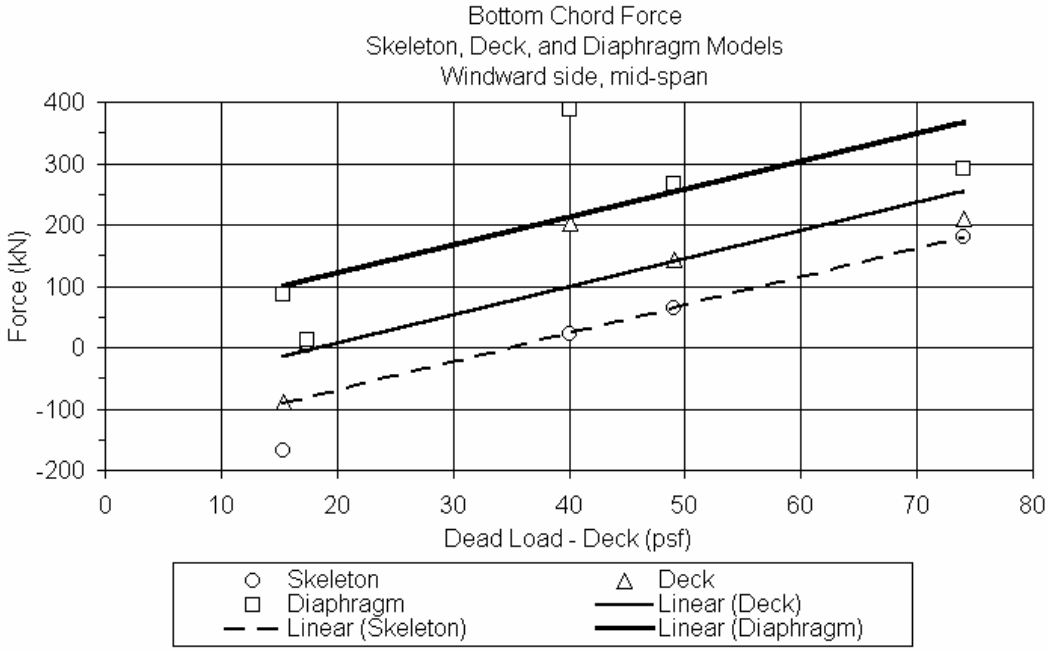


Figure 2.51. Force vs. Deck Dead Load for skeleton, deck, and diaphragm models shown on the same graph. A linear regression curve for each data set is shown.

Figure 2.52 shows the relationship of the force in the windward bottom chord for the Deck models vs. those for the Diaphragm models. The Diaphragm models, in which the plane of the deck was locked to prohibit deformation, were examined because they represent an upper bound on deck lateral stiffness.

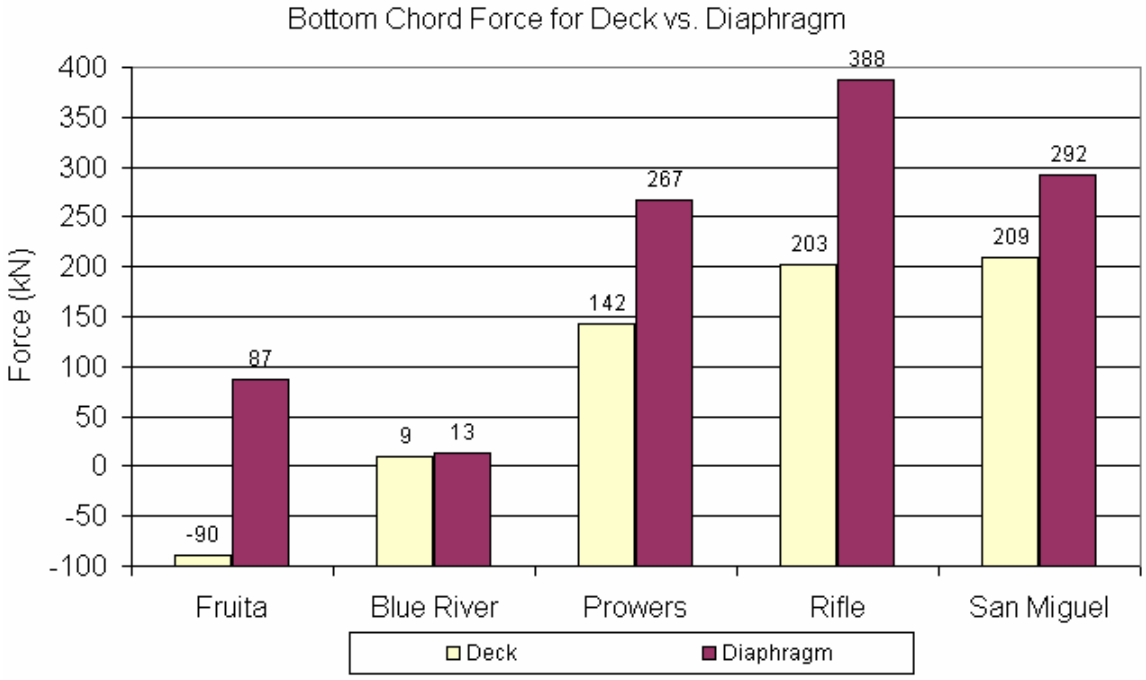


Figure 2.52. Windward Bottom Chord Force vs. Deck Dead Load for Deck and Diaphragm. Small differences between the deck and diaphragm values indicate that the deck is about as laterally stiff as theoretically possible, such as for Blue River Bridge. Large differences indicate that the deck is not nearly as stiff as theoretically possible, such as for Fruita Bridge or Rifle Bridge.

Figure 2.53 shows the relationship of the force in the windward bottom chord for decks of different dead loads. Forces from analyses with the original timber decks, with relatively light dead loads, are plotted next to forces from analyses made using the current and higher deck dead load. The problem of compression in the windward bottom chords is clearly more pronounced in the lighter, timber deck models

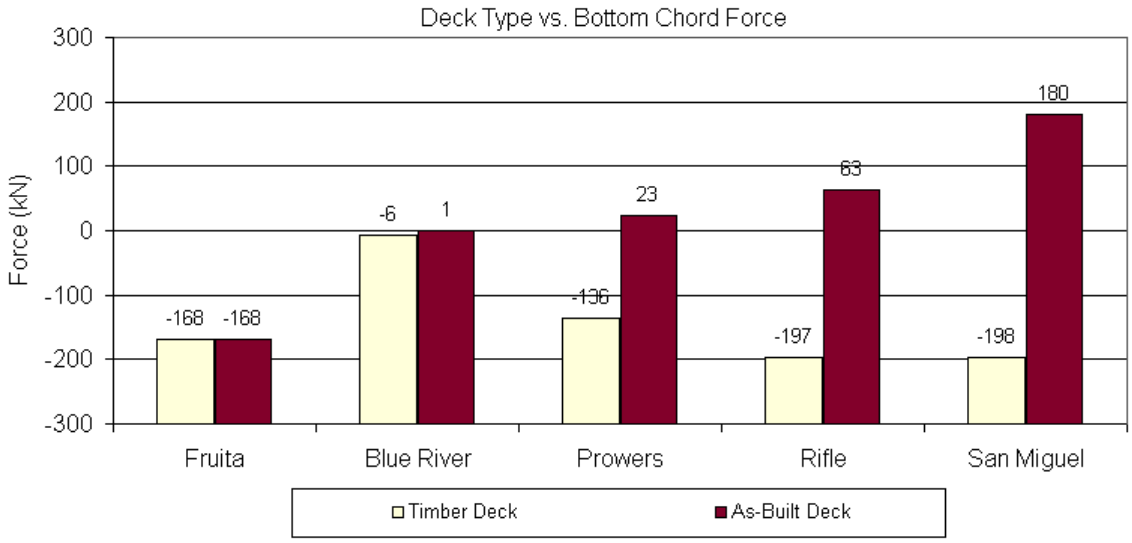


Figure 2.53. Windward Bottom Chord Force for Timber Decks and for As-Built Decks. Fruita Bridge has the same values for both cases because the existing (as-built) deck is the same configuration as its original timber deck. The other bridges have higher forces in the windward bottom chord because the higher as-built deck weights increase tension in both the windward and leeward bottom chords.

## 2.8 Recommendations

The problem of high calculated compression in windward bottom chord eyebars under (D + W) can be addressed two ways:

- Account for the stiffening effect of the deck. As the deck stiffens the structure, the windward bottom chord force increases in tension. Depending on the deck dead load, this may be sufficient. Note that there is no construction cost; this approach was entirely analytical.
- Add dead load to the deck. Increasing the deck dead load increases the tensile force in both bottom chords. Use of skeleton models to study this effect will lead to artificially low (i.e. artificially high compressive) bottom chord tensile forces. Use of deck models will more accurately predict the actual forces. There is an upper bound to the amount of additional dead load – at some point member stresses under (L + D) will be limiting. There will be construction cost.

## PART 3 VERIFICATION RESULTS

The bridges were instrumented such that strain data from selected members could be collected simultaneously with wind speed and direction data. The data was used to verify the deck models. The field tests and results are reported in this part. A detailed description of the instrumentation is in Appendices A and B.

### 3.1 Fruita Bridge

Figures 3.1 through 3.11 and Tables 3.1 and 3.2 show the location of instruments and results for Fruita Bridge.

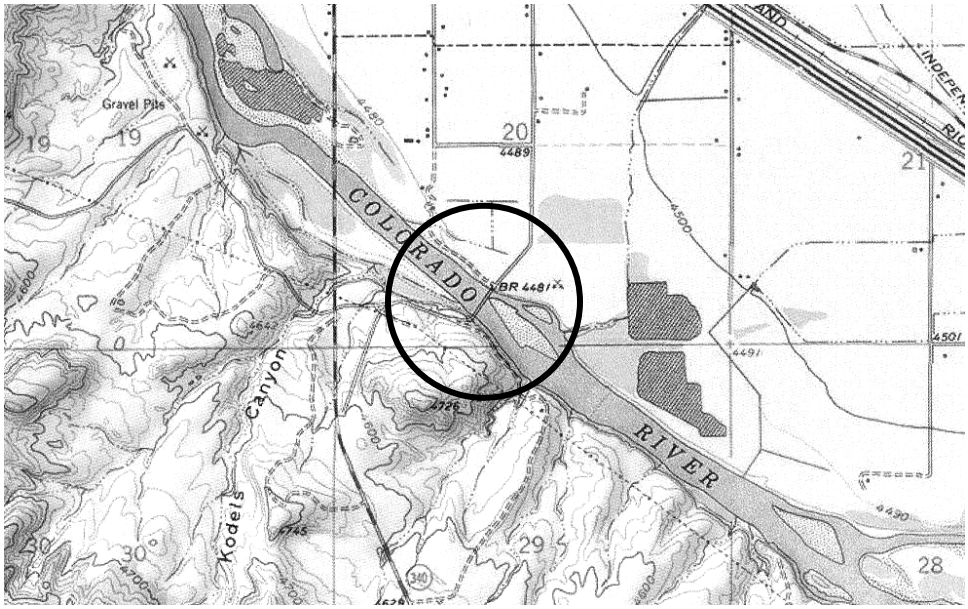


Figure 3.1. Location of Fruita Bridge. It is approximately 2.5 kilometers (1.5 miles) south of City of Fruita, CO. While the bridge is oriented approximately southwest to northeast, the wind direction sensor was oriented parallel to the bridge's longitudinal axis, making the local north direction the equivalent of global northeast. Note that the local topography is relatively flat north of the Colorado River, but hilly to the south. However, wind from the northwest (local west) will be directed approximately broadside to the bridge (USGS 1973).

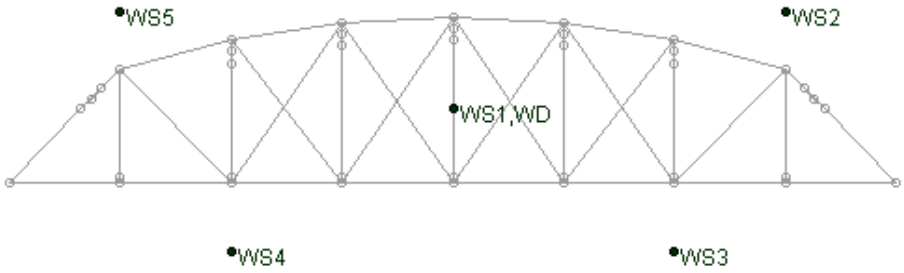


Figure 3.2. Diagram of Fruita Bridge, illustrating the locations of anemometers (WS1 – WS5) and wind direction sensor (WD). North is to the left. WS1 was positioned directly upwind of the centroid of the wind intercept area. WS2 and WS5 were located 3 meters (approximately 10 feet) above the top of the end diagonal members in the portals. WS3 and WS4 were positioned 3.5 meters (11.5 feet) below the bridge deck, at an elevation mid-height between the bridge deck and the water surface below.

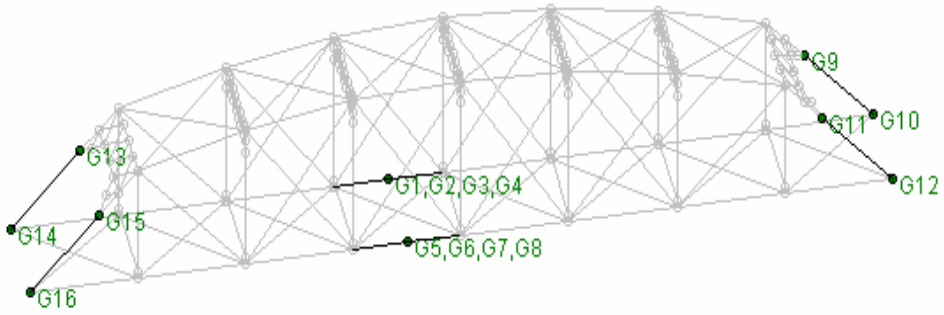


Figure 3.3. Diagram of Fruita Bridge, illustrating the locations of the strain transducers. North is to the left. The wind direction was from the west, orthogonal to the bridge. Strain transducer numbers G1 – G4 were clamped to the leeward bottom chord eyebars. G5 – G8 were clamped to the windward bottom chord eyebars. G9 – G12 were clamped to the end diagonals at the south portal. G13 – G16 were clamped to the end diagonals at the north portal.

Table 3.1. Fruita Bridge Wind Velocities, Quadrant Average Velocities, and Quadrant Pressures.

| Anemometer | Location | Velocity m/s (mph) | Average velocity for quadrant m/s (mph) | Average pressure for quadrant $P_a$ (psf) |
|---|---|---|---|---|
| WS1 | Central | 11.5 (25.8) | | |
| WS2 | South upper | 10.2 (22.7) | 10.9 (24.3) | 121 (2.53) |
| WS3 | South lower | 10.4 (23.2) | 11.0 (24.5) | 124 (2.58) |
| WS4 | North lower | 7.2 (16.1) | 8.9 (20.0) | 90.3 (1.72) |
| WS5 | North upper | 6.3 (14.2) | 9.4 (21.0) | 82.2 (1.89) |

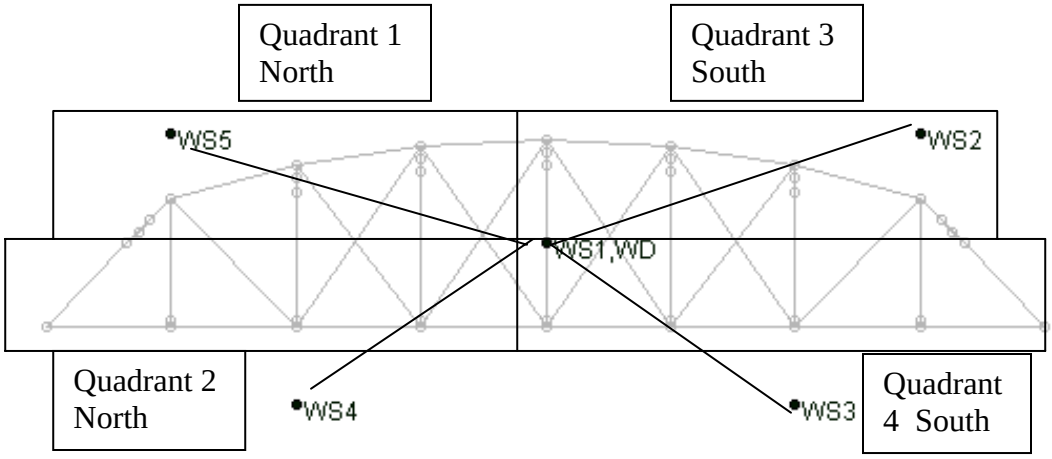


Figure 3.4. Quadrants subjected to different uniformly distributed wind pressures. Wind pressure on Quadrant 1 was determined from a weighted average from the velocities measured at WS5 and WS1. Wind pressure at the other quadrants were similarly determined.

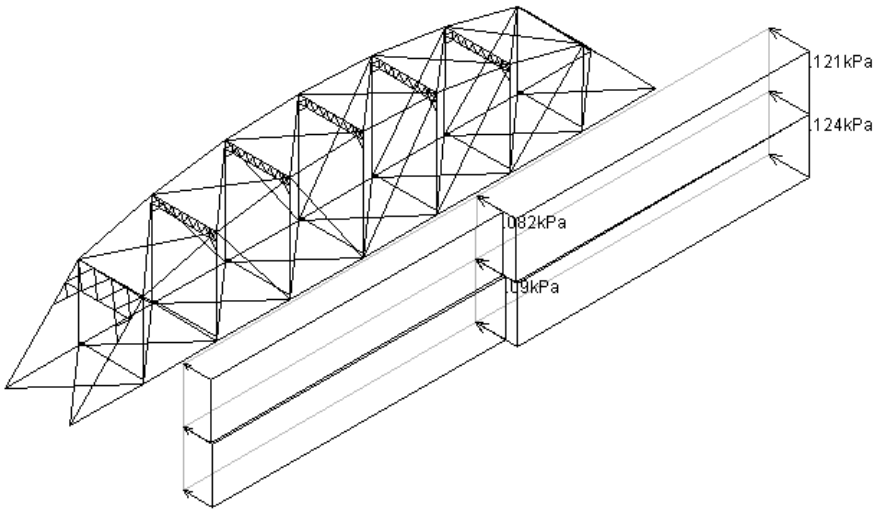


Figure 3.5. Wind pressure applied to the four quadrants for analysis. North is to the left.

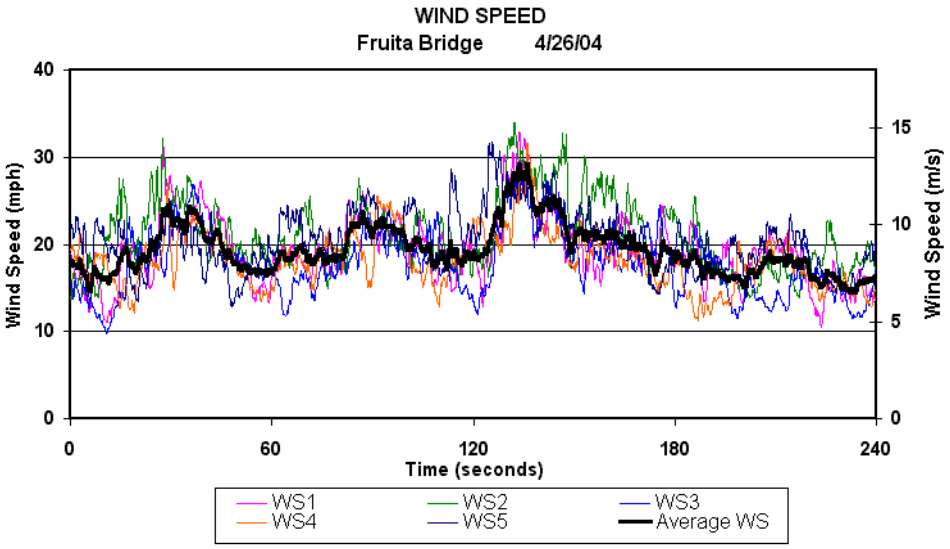


Figure 3.6. Fruita Bridge: Wind Speed as measured by the five anemometers. The bold line shows the average of all five anemometers.

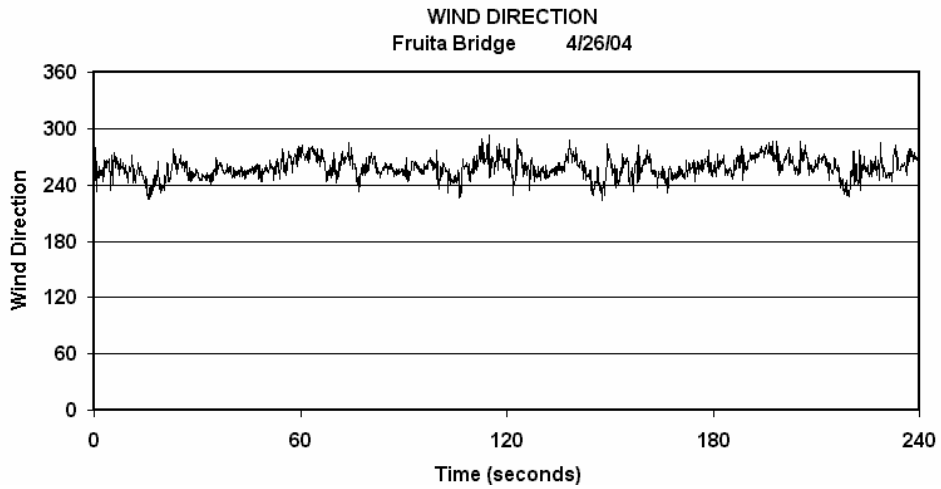


Figure 3.7. Fruita Bridge. Wind direction as measured during the test.

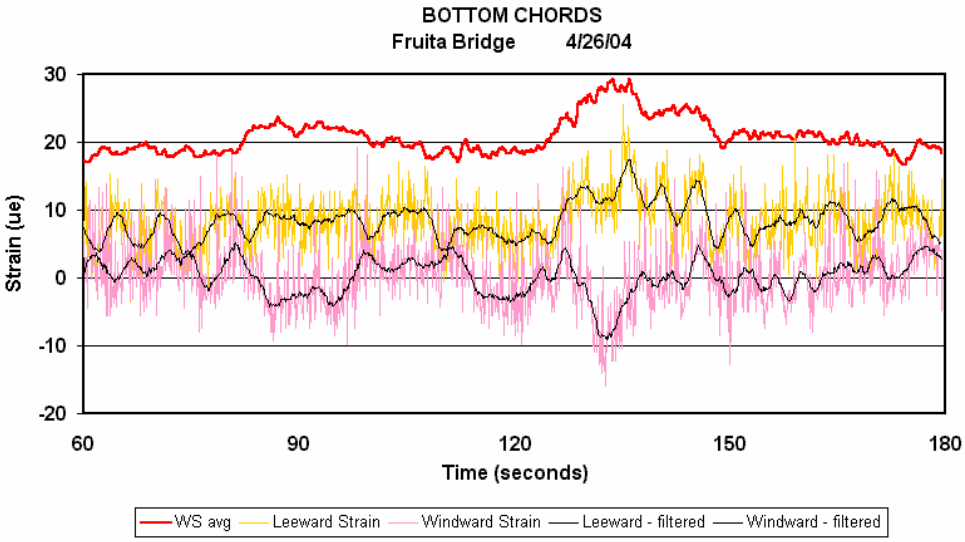


Figure 3.8. Fruita Bridge. Strain measurements for the windward and leeward bottom chord eyebars. The bold trace at the top is the average wind speed, to an arbitrary scale. Measured strain in the leeward eyebar is shown above measured strain in the windward eyebar. Both the raw data and a filtered line that removes much of the signal noise are shown.

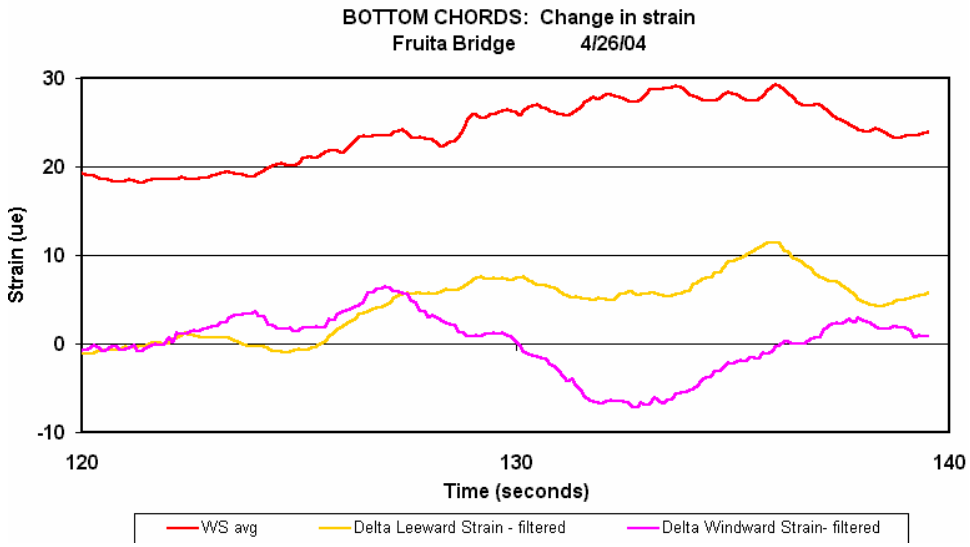


Figure 3.9. Fruita Bridge. Enlargement of the traces for windward and leeward bottom chord eyebar measured strains. Both are baseline traces of the filtered data. Thus, they represent the change in measured strain starting from the same point in time as the corresponding change in wind velocity. The wind velocity is shown for reference at the top of the graph to an arbitrary scale.

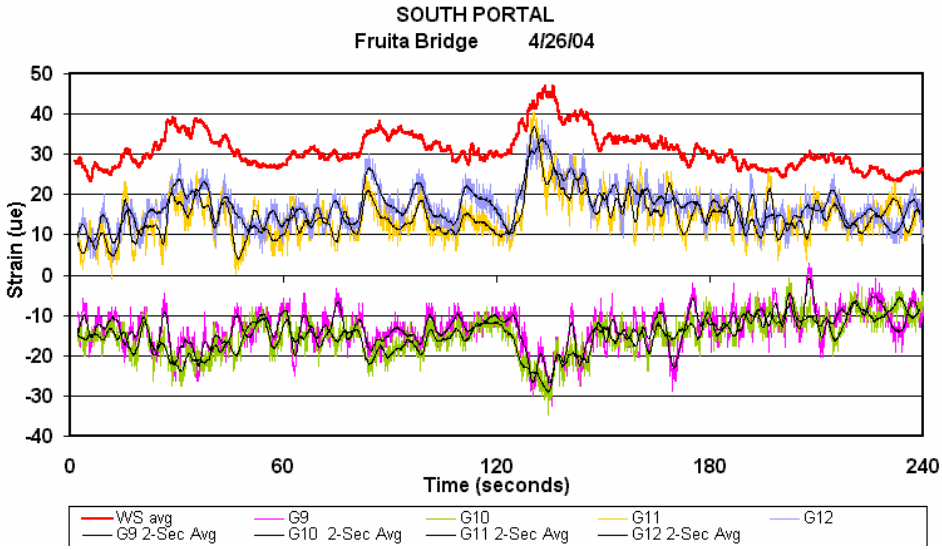


Figure 3.10. Fruita Bridge. Measured strains at the south portal are shown.

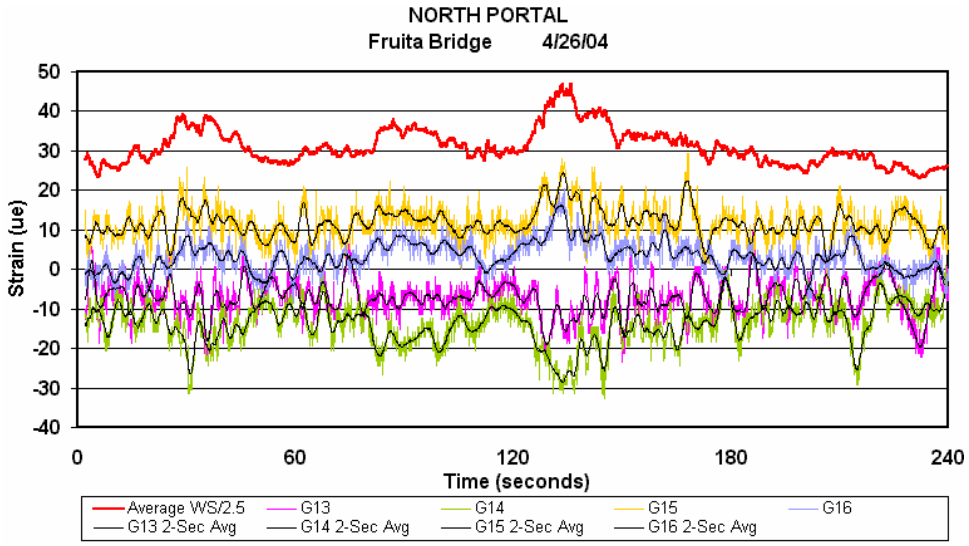


Figure 3.11. Fruita Bridge. Measured strains at the north portal are shown.

Table 3.2. Fruita Bridge Verification Summary. Comparison of calculated forces to measured forces expressed in kN (kips) and kN-m (foot-kips)

| Member | Calculated Force | Measured Force | Correlation: % difference |
|---|---|---|---|
| Windward bottom chord | -1.37 kN (-0.31 kips) | -1.44 kN (-0.32 kips) | 5% |
| Leeward bottom chord | 2.09 kN (0.46 kips) | 2.95 kN (0.66 kips) | 41% |
| North portal upper | 1.77 kN-m (1.29 ft-k) | 1.60 kN-m (1.17 ft-k) | 17% |
| North portal lower | 2.34 kN-m (1.71 ft-k) | 1.79 kN-m (1.31 ft-k) | 24% |
| South portal upper | 1.29 kN-m (0.94 ft-k) | 1.81 kN-m (1.32 ft-k) | 40% |
| South portal lower | 1.92 kN-m (1.40 ft-k ) | 1.19 kN-m (0.87 ft-k) | 38% |

Fruita Conclusion:

Good correlations were achieved for the windward bottom chord and the north portal. Study of Figure 3.9 suggested that the weaker correlation for the leeward bottom chords can be explained as a probable anomaly in the field data. The weaker correlations for the south portal may be because the calculated values are based on boundary conditions at the portal bases, which may not be entirely correct. The actual portal bases were on roller nests that were broken, rusted, and contained dirt. While they were treated as shown in Appendix C in the calculations they may have permitted some small rotation, that is they may have exhibited some degree of partial fixity, which would affect the portal correlations; this would increase bending moment at the upper portal and decrease it at the lower portal, both tending to improve the correlations.

## 3.2 Prowers Bridge

Figures 3.12 through 3.22 and Tables 3.3 and 3.4 show the location of instruments and results for Prowers Bridge.

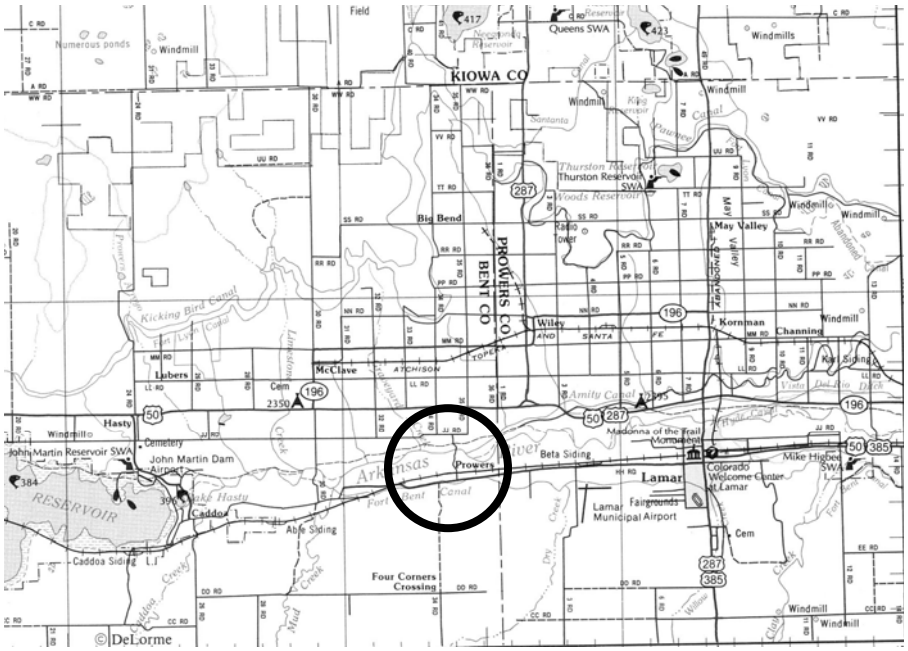


Figure 3.12. Prowers Bridge. Location of Prowers Bridge. It is approximately 16.1 kilometers (10 miles) west of City of Lamar, CO (Delorme 1997a). The bridge is oriented approximately north to south, the wind directions sensor was oriented parallel to the bridge's longitudinal axis, making the local north direction the equivalent of global north. The wind from the west would be directed approximately broadside to the bridge.

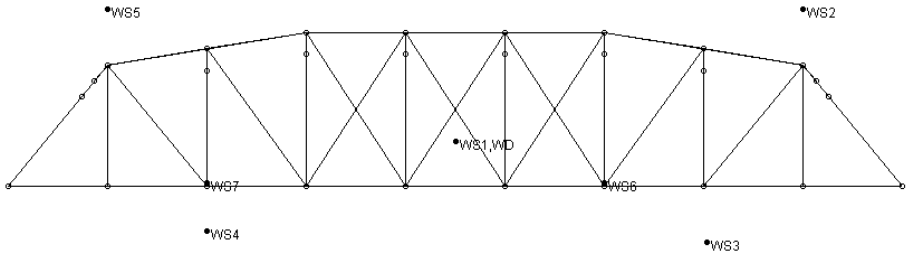


Figure 3.13. Diagram of Prowers Bridge illustrating the locations of the anemometers (WS1-WS7) and wind direction sensor (WD). North is to the left. WS1 was positioned directly upwind of the centroid of the wind intercept area. WS2 and WS5 were located 3 meters (approximately 10 feet) above the top of the end diagonal members in the portals. WS3 was positioned 3 meters (approximately 10 feet) below the bridge deck, at an elevations mid-height between the bridge deck and the water surface below. WS4 was positioned 2.5 meters (approximately 8 feet) below the bridge deck, at an elevations mid-height between the bridge deck and the existing ground below. WS6 and WS7 were positioned approximately at the deck elevation.

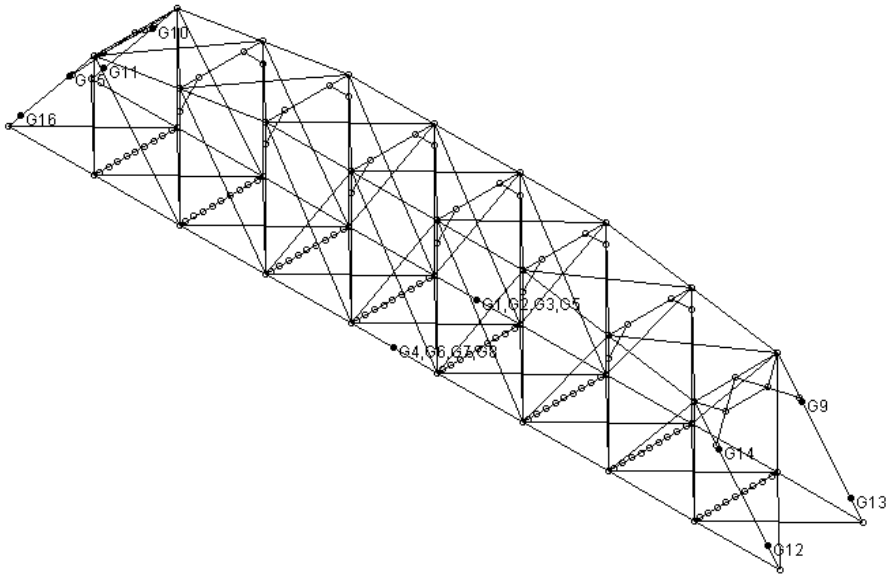


Figure 3.14. Diagram of Prowers Bridge. Ilustrating the locations of the strain transducers. North is to the left. The wind direction was from the west, orthogonal to the bridge. Strain transducer numbers, G1-G3, G5 were clamped to the leeward bottom chord eyebars. G4, G6-G8 were clamped to the windward bottom chord eyebars. G9, G12-G14 were clamped to the end diagonals at the south portal. G10-G11, G15-G16 were clamped to the end diagonals at the north portal.

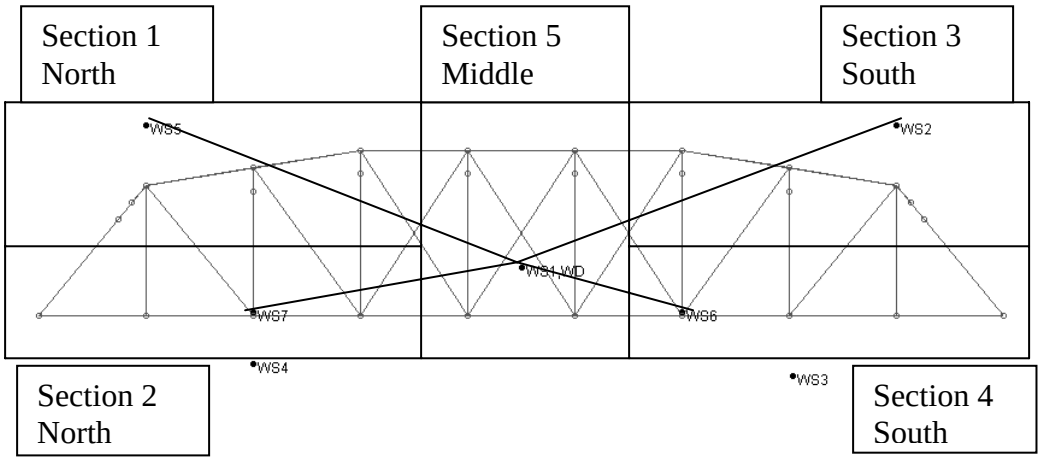


Figure 3.15. Sections subjected to different uniformly distributed wind pressures. Wind pressure on Section 1 was determined from a weighted average from the velocities measured at WS5 and WS1. Wind pressures at the other sections were similarly determined except for Section 5. Section 5 was determined from WS1 only.

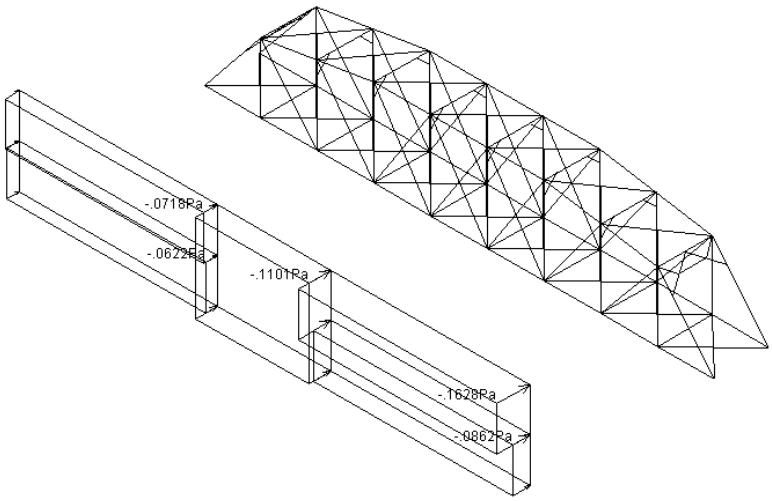


Figure 3.16. Wind pressure applied to the five sections for analysis. North is to the left.

Table 3.3. Prowers Bridge. Wind Velocities, Section Average Velocities, and Section Pressures.

| Anemometer | Location | Velocity m/s (mph) | Average velocity for section m/s (mph) | Average pressure for section Pa (psf) |
|---|---|---|---|---|
| WS1 | Central | 10.0 (22.3) | 10.0 (22.3) | 110.1 (2.3) |
| WS2 | South Upper | 14.1 (31.6) | 12.1 (27.0) | 162.8 (3.4) |
| WS3 | South Lower | 7.1 (15.8) | Not used in any section | Not used in any section |
| WS4 | North Lower | 1.0 (2.2) | Not used in any section | Not used in any section |
| WS5 | North Upper | 5.5 (12.2) | 7.7 (17.3) | 71.8 (1.5) |
| WS6 | South Middle | 7.5 (16.7) | 8.7 (19.5) | 86.2 (1.8) |
| WS7 | North Middle | 3.2 (7.2) | 3.5 (7.9) | 62.2 (1.3) |

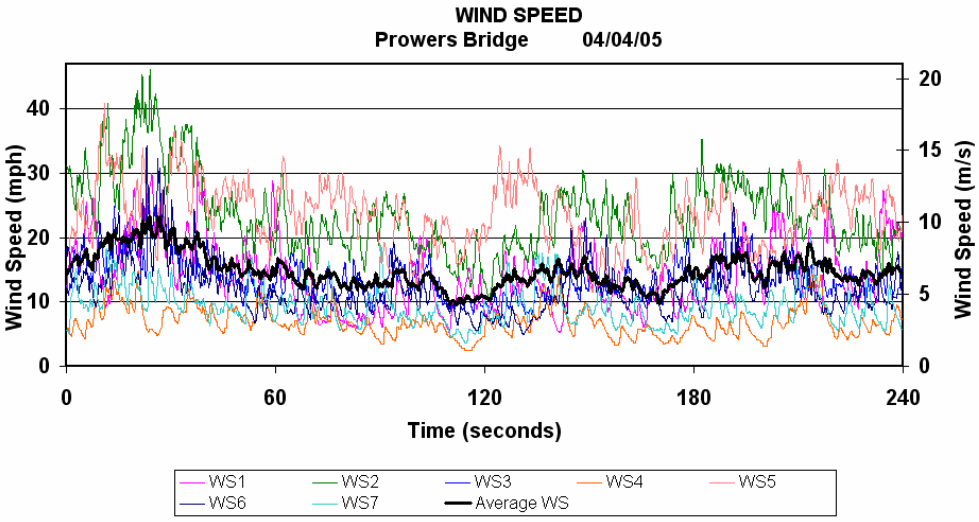


Figure 3.17. Prowers Bridge. Wind speed as measured by the seven anemometers. The bold line shows the average of all seven anemometers.

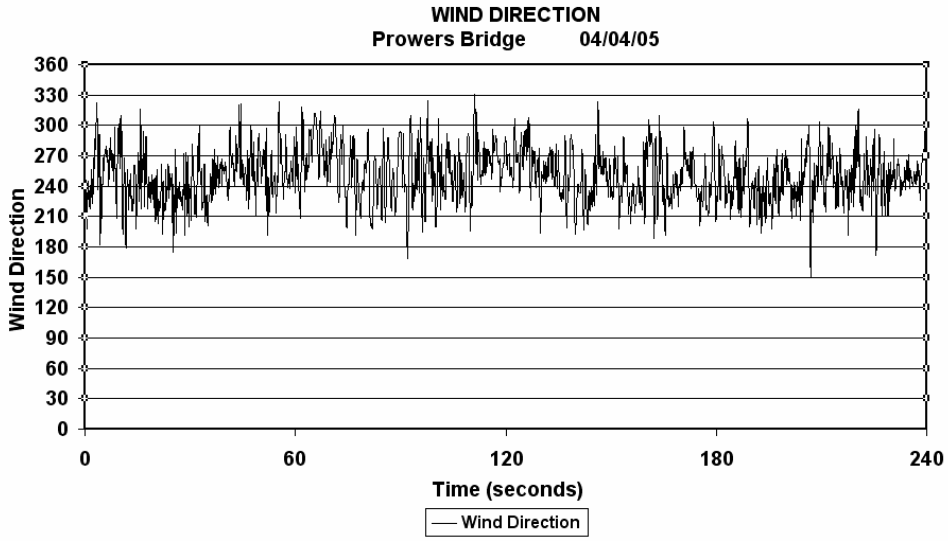


Figure 3.18. Prowers Bridge. Wind direction as measured during the test.

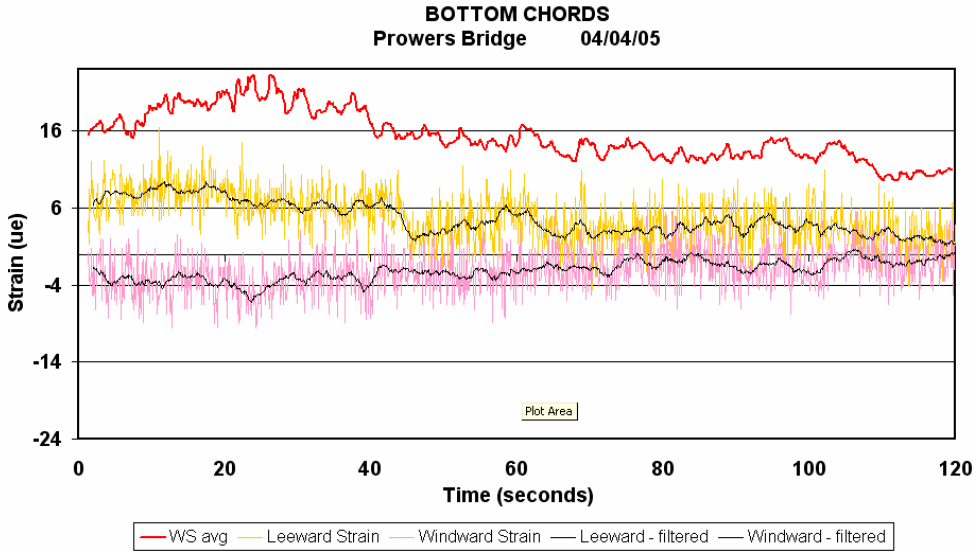


Figure 3.19. Strain measurements for the windward and leeward bottom chord eyebars. The bold trace at the top is the average wind speed, to an arbitrary scale. Measured strain in the leeward eyebar is shown above measured strain in the windward eyebar. Both the raw data line and a filtered line that removes much of the signal noise shown.

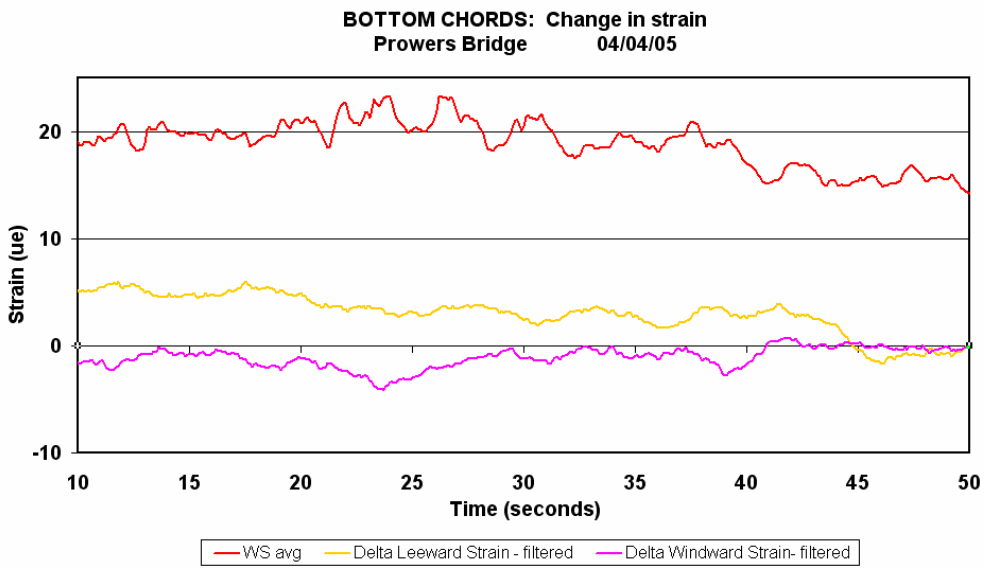


Figure 3.20. Prowers Bridge. Enlargement of the traces for windward and leeward bottom chord eyebar measured strains. Both are baseline traces of the filtered data. Thus, they represent the change in measured strain starting from the same point in time as the corresponding change in wind velocity. The wind velocity is shown for reference at the top of the graph to an arbitrary scale.

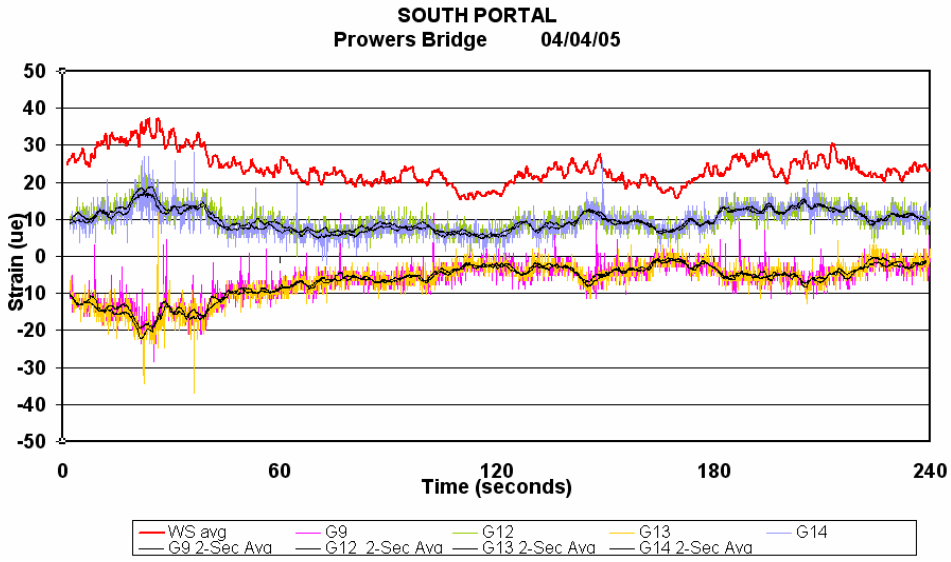


Figure 3.21. Prowers Bridge. Measured strains at the south portal are shown.

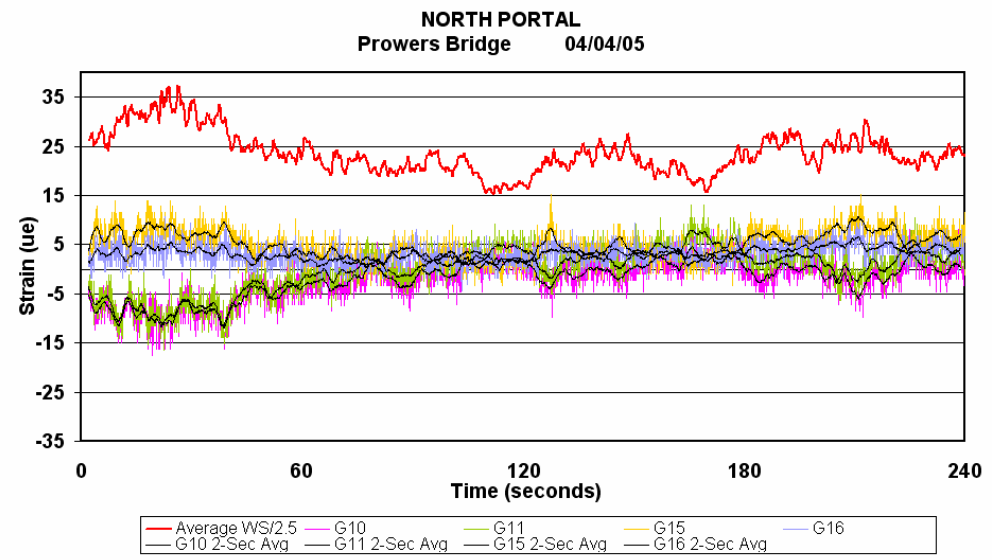


Figure 3.22 Prowers Bridge. Measured strains at the north portal are shown.

Table 3.4. Prowers Bridge Verification Summary. Comparison of calculated forces to measures forces expressed in kN (kips) and m-kN (foot-kips).

| Member | Calculated Force | Measured Force | Correlation: % Difference |
|---|---|---|---|
| Windward Bottom Chord | -2.71 kN (-0.61 kips) | -3.11 kN (-0.70 kips) | 14% |
| Leeward Bottom Chord | 2.74 kN (0.62 kips) | 3.10 kN (0.70 kips) | 13% |
| North Portal Upper | 1.52 m-kN (1.12 ft-k) | 0.67 m-kN (0.50 ft-k) | 56% |
| North Portal Lower | 1.76 m-kN (1.30 ft-k) | 0.47 m-kN (0.36 ft-k) | 73% |
| South Portal Upper | 2.44 m-kN (1.80 ft-k) | 1.33 m-kN (0.98 ft-k) | 45% |
| South Portal Lower | 2.54 m-kN (1.87 ft-k) | 1.48 m-kN (1.09 ft-k) | 42% |

Prowers Conclusion:

A good correlation is observed for all the bridge members except for the North Portal. A reason for a weak correlation for the North Portal is that the actual roller bearing in the field is shifted off the roller, which could allow possibly rotation in any direction. In the RISA-3D model, the roller is released about the pin and restrained in other two directions similar to the Fruita Bridge boundary conditions as shown in Appendix C. Lower portions of the North Portal members were also shielded wind due an existing embankment of a newer, adjacent bridge about 15 meters (50 feet) to the west. The wind pressure in RISA-3D model could possibly be higher than the bridge really experienced in the field due to shielding effects of the embankment.

## 3.3 Blue River Bridge

Figures 3.23 through 3.32 and Tables 3.5 and 3.6 show the location of instruments and results for Blue River Bridge.

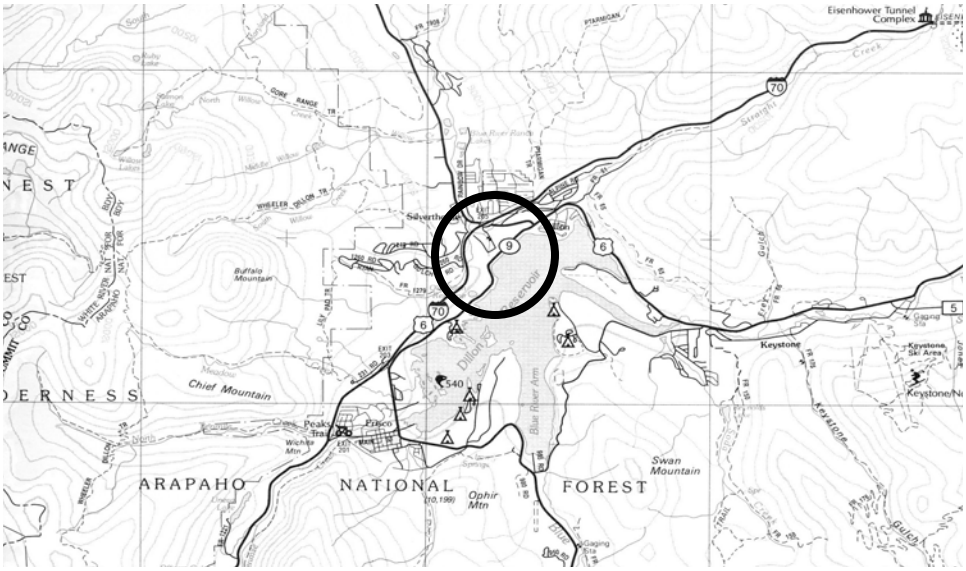


Figure 3.23. Location of Blue River Bridge. It is located over the Blue River near Silverthorne/Dillon, Colorado (DeLorme 1997b). It is believed that the bridge was built approximately 1895 as the Two-Mile bridge near Breckenridge, Colorado and moved to this site at a later date.

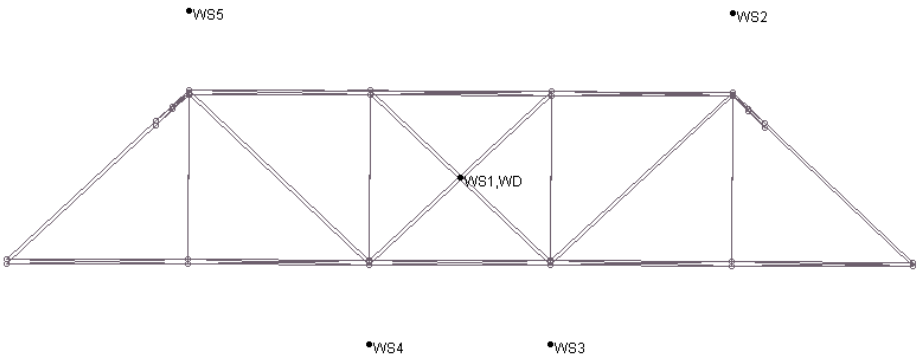


Figure 3.24. Diagram of Blue River Bridge, illustrating the locations of anemometers (WS1-WS5) and wind direction sensor (WD). North is to the left. WS1 was positioned at the approximate center of the wind intercept area. WS2 and WS5 were located above the end diagonal in the portals. WS3 and WS5 were located below the bridge an the elevation mid-height between the bridge deck and the water surface below.

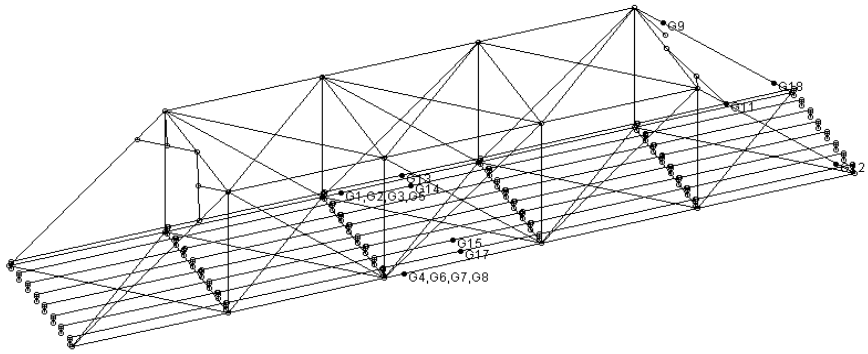


Figure 3.25. Diagram of Blue River Bridge, illustrating the locations of the strain transducers. North is to the left. The wind direction was from east to west, orthogonal to the bridge. Strain transducers G1, G2, G3 and G5 were clamped to the windward bottom chord eyebars. G4, G6, G7 and G8 were clamped to the leeward bottom chord eyebars. G9 and G11 were clamped to the top of the south portals. G12 and G18 were clamped to the bottom of the south portals. G13 and G14 were clamped to the east stringers in the middle bay and G15 and G17 were clamped to the west stringers.

Table 3.5. Blue River Bridge Wind Velocities, Quadrant Average Velocities, and Quadrant Pressures.

| Anemometer | Location | Velocity m/s (mph) | Average velocity for quadrant m/s (mph) | Average pressure for quadrant $P_a$ (psf) |
|---|---|---|---|---|
| WS1 | Central | 14.06 (31.46) | | |
| WS2 | South upper | 15.31 (34.24) | 14.69 (32.85) | 230.30 (4.81) |
| WS3 | South lower | 11.16 (24.96) | 12.61 (28.21) | 110.12 (2.30) |
| WS4 | North lower | 10.64 (23.81) | 12.35 (27.64) | 121.62 (2.54) |
| WS5 | North upper | 16.69 (37.33) | 15.38 (34.40) | 205.89 (4.30) |

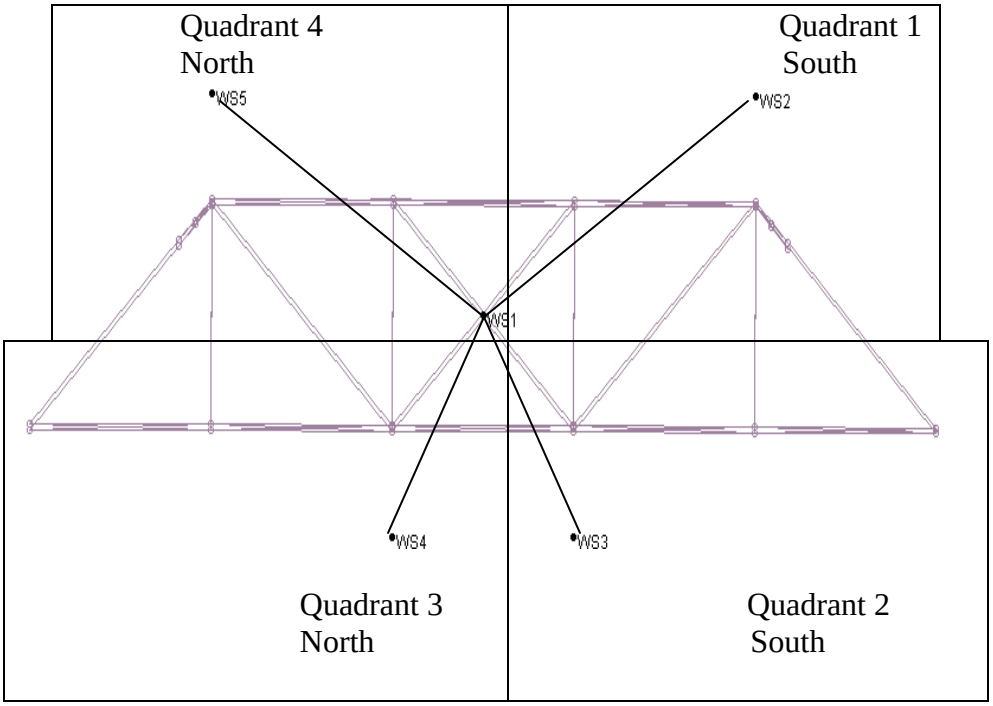


Figure 3.26. Blue River Bridge. Quadrants subjected to different uniformly distributed wind pressures. Wind pressure on quadrant 1 was determined from a weighted average from the velocities measured at WS1 and WS2 . Wind pressure at the other quadrants were similarly determined.

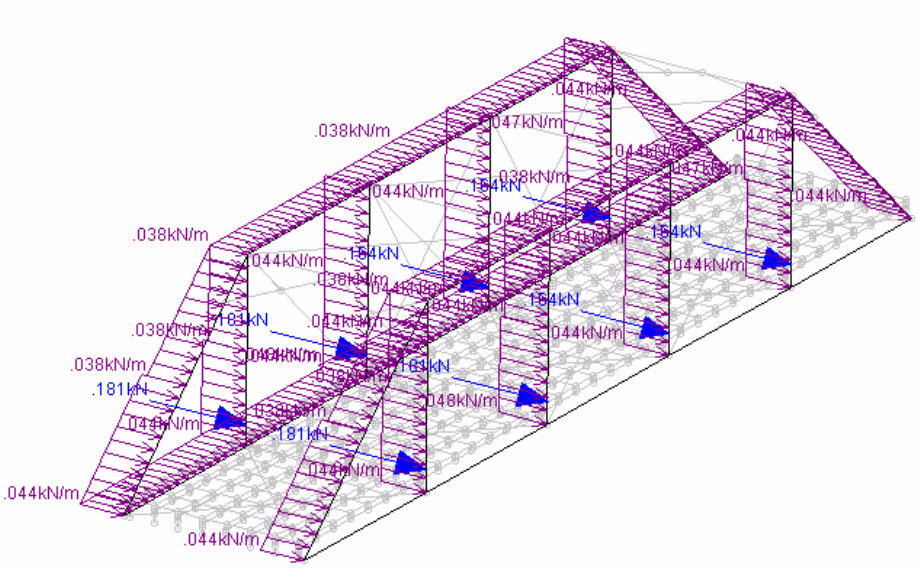


Figure 3.27. Wind pressure applied to the four quadrants for analysis. North is to the right.

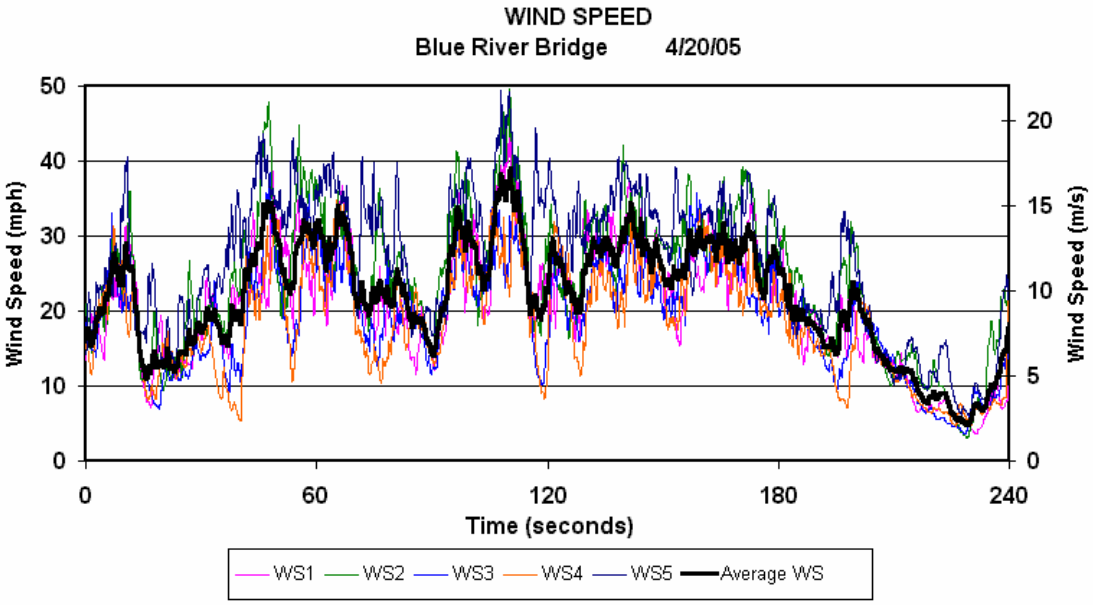


Figure 3.28. Blue River Bridge: Wind Speed as measured by the five anemometers. The average of all five anemometers is shown in bold line.

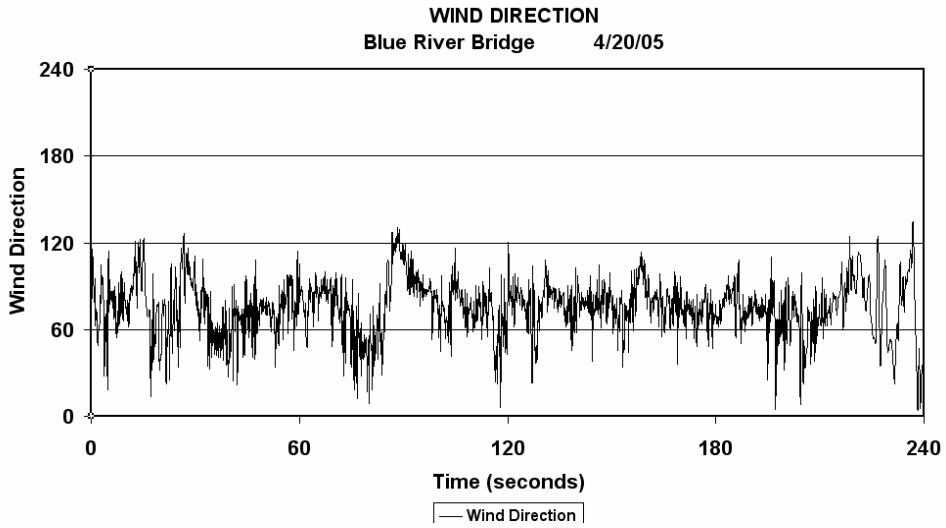


Figure 3.29. Blue River Bridge: Wind direction as measured during the test. Unlike all the other bridges, the wind direction was from the east.

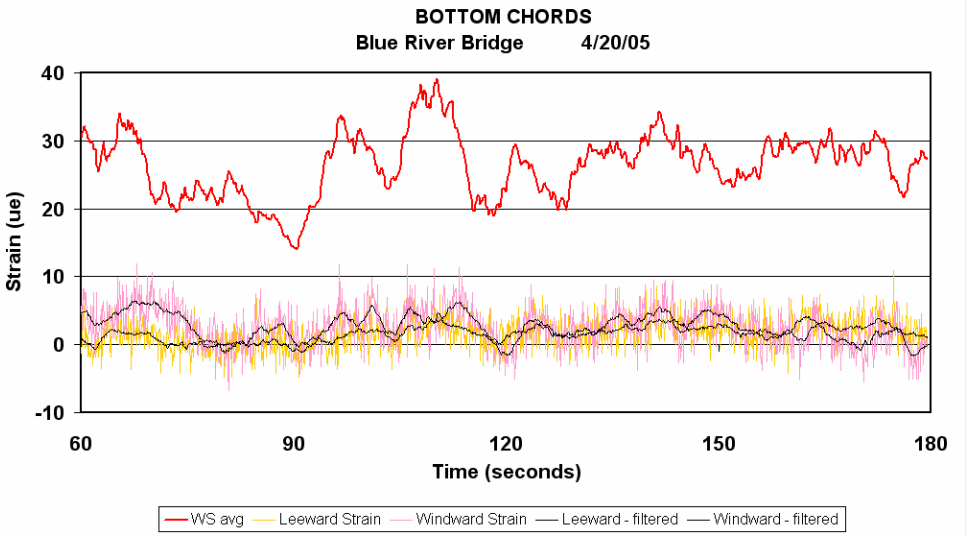


Figure 3.30. Blue River Bridge. Strain measurements for the windward and leeward bottom chord eyebars. The average wind speed, to an arbitrary scale, is also shown as the bold line at the top. Strain in the leeward eyebar is shown above strain in the windward eyebar. Both the raw data and a filtered line that removes much of the signal noise are shown.

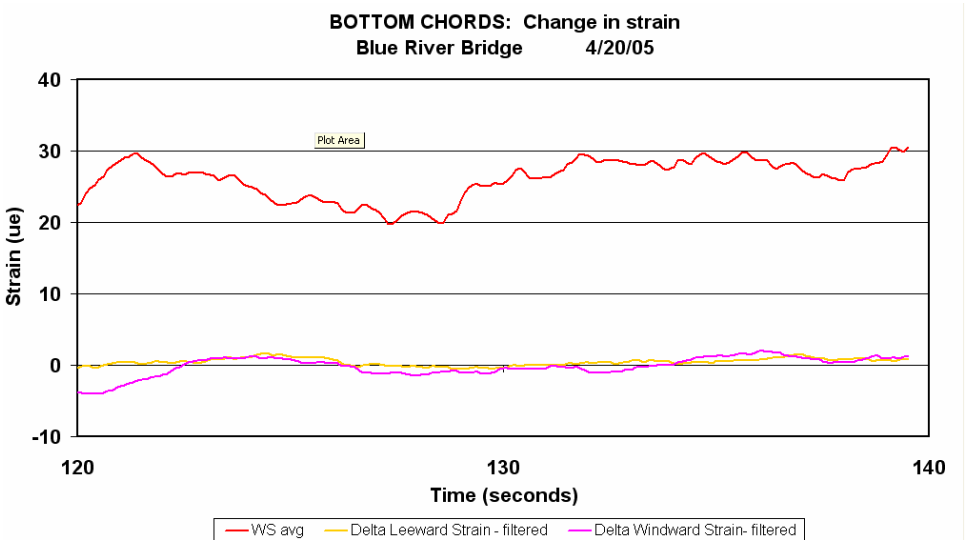


Figure 3.31. Blue River Bridge. Enlargement of the trace for windward and leeward. Bottom chord eyebar measured strains. Both are baseline traces of the filter data. Thus, they represent the change in measured strain starting from the same point in time as the corresponding change in wind velocity. The wind velocity is shown for reference at the top of the graph to an arbitrary scale.

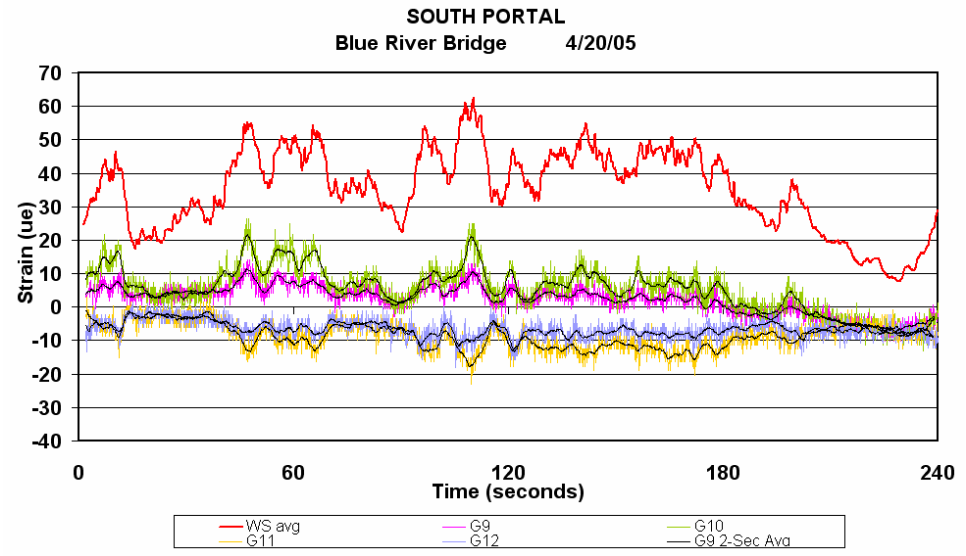


Figure 3.32. Blue River Bridge. Measured strains at the south portal are shown.

Table 3.6. Blue River Bridge Verification Summary. Comparison of calculated forces to measured forces expressed in kN (kips) and kN-m (ft-kips). The north portal was not instrumented.

| Member | Calculated Force | Measured Force | Correlation: % difference |
|---|---|---|---|
| Windward bottom chord | -0.44 kN (-0.1 kips) | -0.54 kN (-0.122 kips) | 23% |
| Leeward bottom chord | 1.44 kN (0.32 kips) | 0.78 kN (0.18 kips) | 45% |
| South portal upper | 0.77 kN-m (0.56 ft-k) | 0.70 kN-m (0.51 ft-k) | 15% |
| South portal lower | 1.25 kN-m (0.91 ft-k ) | 0.55 kN-m (0.40 ft-k) | 56% |

* $E = 10.34 \times 10^6$ KPa ($1.5 \times 10^3$ ksi) and $E = 13.79 \times 10^6$ KPa ($2.0 \times 10^3$ ksi) were both used in RISA-3D modeling and both gave the same results, therefore the deck stiffness had little or no effect on member forces. $E = 13.79 \times 10^6$ KPa ($2.0 \times 10^3$ ksi) is considered an upper bound on the stiffness of the wood in the deck, so higher stiffnesses were not considered.

Blue River conclusion:

Good correlations were achieved for the windward bottom chord and the south upper portal, suggesting that the deck model is a reasonable approximation. The weaker correlation for the leeward bottom chord may have been influenced by the buckled existing condition of those eyebars. The actual bearings could not be observed because they were buried in soil. The bearings were presumed to be rusted to a “frozen” condition and were treated as fixed in the calculations. However, they may have permitted some small rotation, that is they may have exhibited some small degree of partial fixity, which would have altered the calculated results.

## 3.4 San Miguel Bridge

Figures 3.33 through 3.43 and Tables 3.7 and 3.8 show the location of instruments and results for San Miguel Bridge.

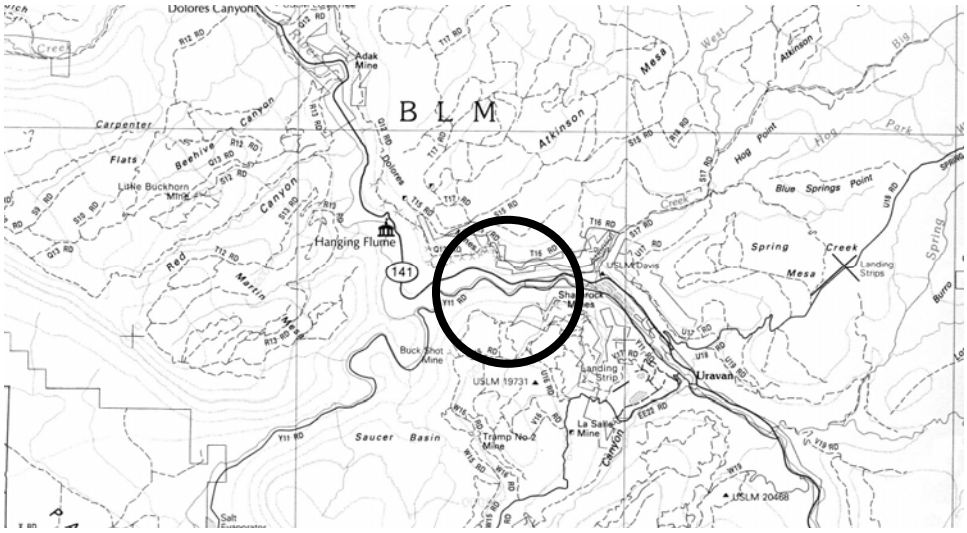


Figure 3.33 – San Miguel Bridge, Location Map. One of the five original spans was relocated from Grand Junction, CO to a now abandoned County Road northwest of Uravan in Montrose County, CO spanning the San Miguel River (DeLorme 1997c). The bridge still resides in this location, but was closed to vehicular traffic in 1988 (Fraser, 2000c).

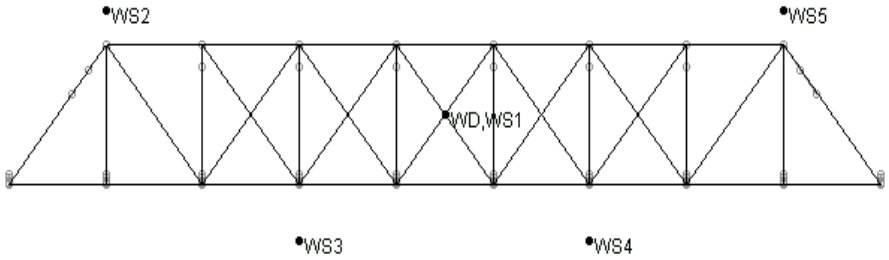


Figure 3.34 – Diagram of San Miguel Bridge, illustrating the locations of anemometers (WS1 – WS5) and wind direction sensor (WD). North is to the left. WS1 was positioned directly upwind of the approximate center of the wind intercept area. WS2 and WS5 were located 1.5 meters (approximately 5 feet) above the top of the end diagonal members in the portals. WS3 and WS4 were positioned 2 meters (approximately 7 feet) below the bridge deck, at an elevation mid-height between the bridge deck and the water surface below.

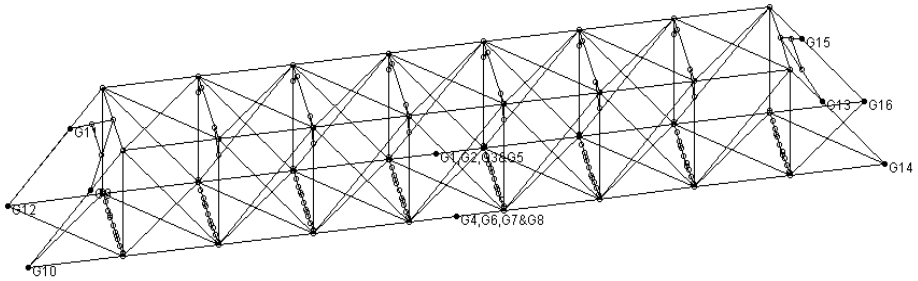


Figure 3.35. Diagram of San Miguel Bridge, illustrating the locations of the strain transducers. North is to the left. The wind direction was from the west, orthogonal to the bridge. Strain transducer numbers G1, G2, G3 & G5 were clamped to the leeward bottom chord eyebars. G4, G6, G7 & G8 were clamped to the windward bottom chord eyebars. G9 – G12 were clamped to the end diagonals at the north portal. G13 – G16 were clamped to the end diagonals at the south portal.

Table 3.7. San Miguel Bridge Wind Velocities, Quadrant Average Velocities, and Quadrant Pressures.

| Anemometer | Location | Velocity m/s (mph) | Average velocity for quadrant m/s (mph) | Average pressure for quadrant $P_a$ (psf) |
|---|---|---|---|---|
| WS1 | Central | 11.5 (25.8) | | |
| WS2 | South upper | 10.2 (22.7) | 10.9 (24.3) | 121 (2.53) |
| WS3 | South lower | 10.4 (23.2) | 11.0 (24.5) | 124 (2.58) |
| WS4 | North lower | 7.2 (16.1) | 8.9 (20.0) | 90.3 (1.72) |
| WS5 | North upper | 6.3 (14.2) | 9.4 (21.0) | 82.2 (1.89) |

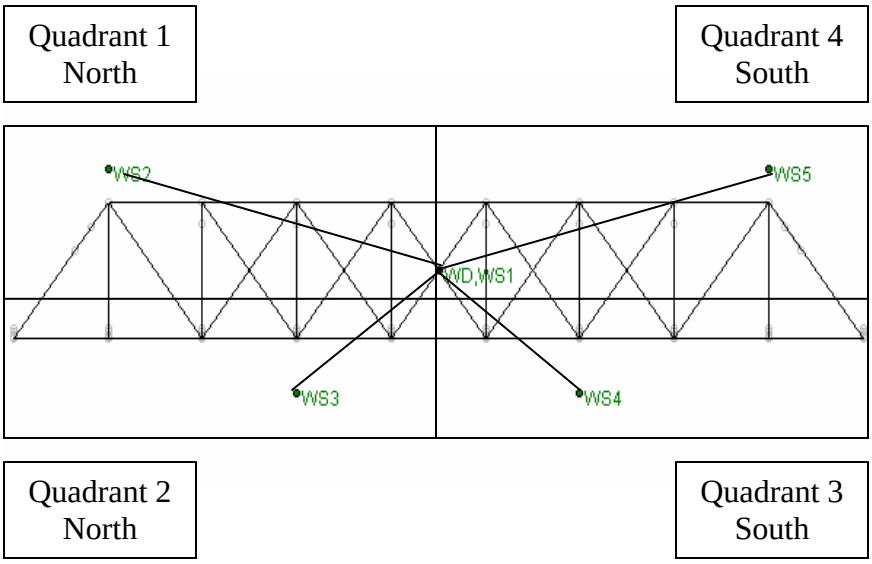


Figure 3.36. Quadrants subjected to different uniformly distributed wind pressures. Wind pressure on Quadrant 1 was determined from a weighted average from the velocities measured at WS2 and WS1. Wind pressure at the other quadrants were similarly determined.

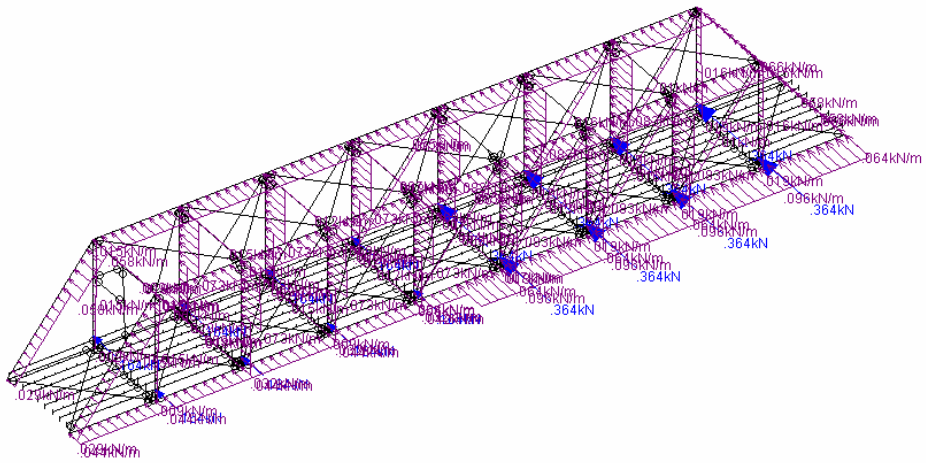

Figure 3.37. Wind Pressure applied to the four quadrants for analysis. North is to the left. Adding another component of wind pressure from the south (not shown here) to simulate the measured wind direction from the southwest was also investigated but the result was inconclusive.

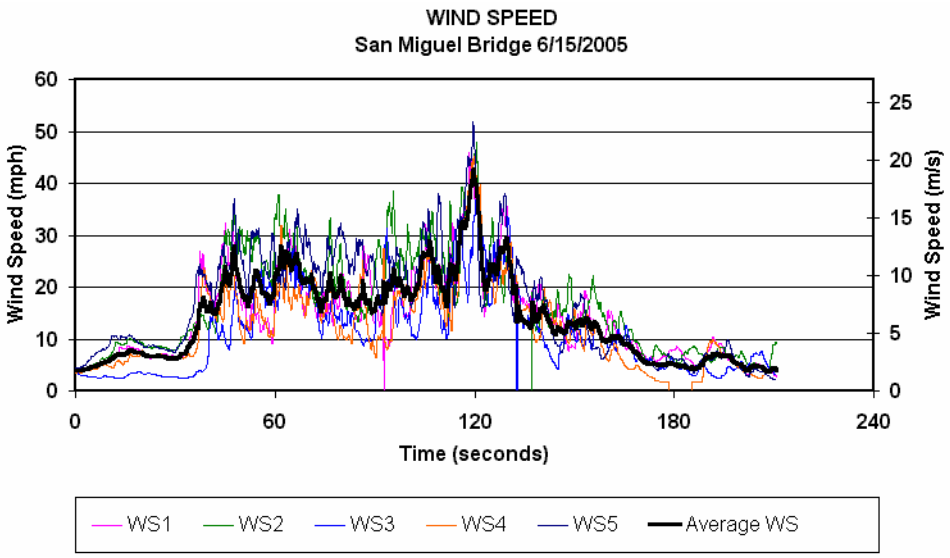


Figure 3.38. San Miguel Bridge: Wind Speed as measured by the five anemometers. The bold line shows the average of all five anemometers.

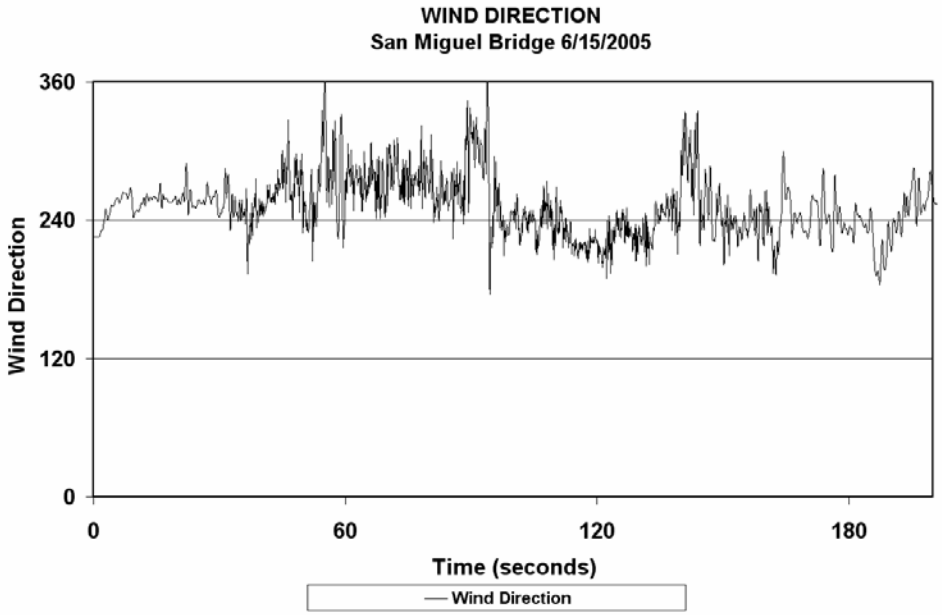


Figure 3.39. San Miguel Bridge. Wind direction as measured during the test.

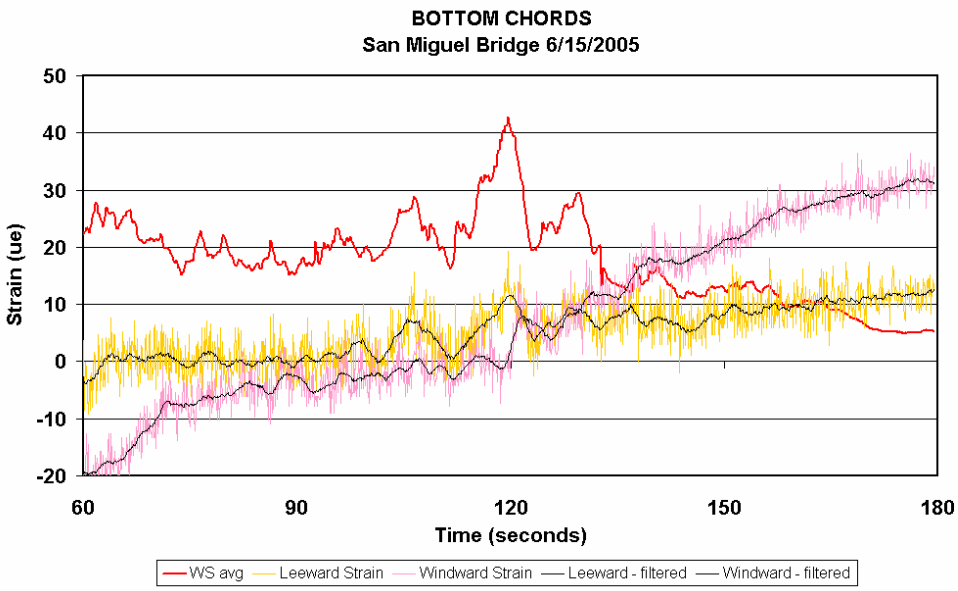


Figure 3.40. San Miguel Bridge. Strain measurements for the windward and leeward bottom chord eyebars. The bold trace at the top is the average wind speed, to an arbitrary scale. Measured strain for bot leeward and windward bottom chords is shown. Both the raw data and a filtered line that removes much of the signal noise are shown. (Note: The increase in the strain value beyond 120 second time is most likely due to some signal drift – it does not appear to be due to mechanically-induced strain because the wind pressure is diminishing in this range).

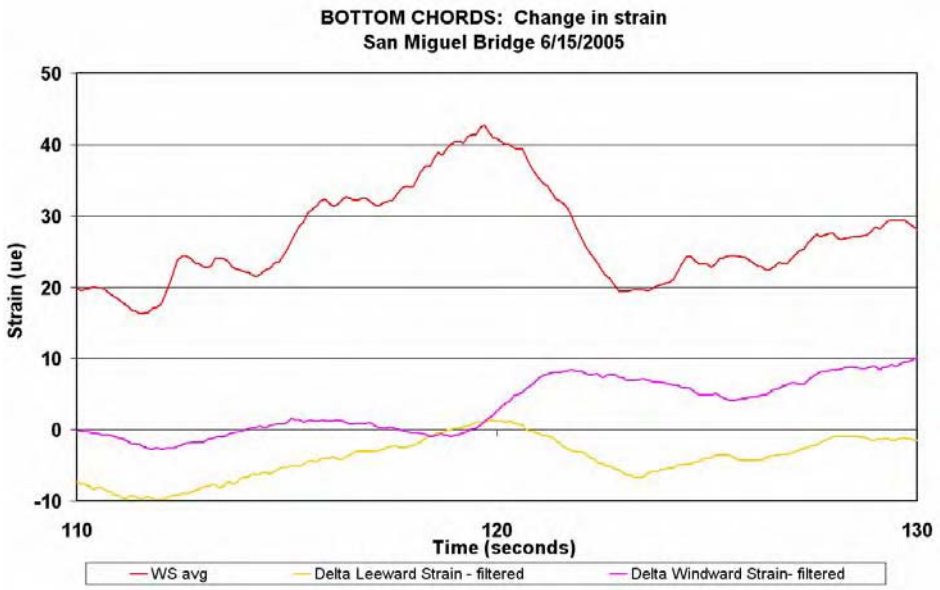


Figure 3.41. San Miguel Bridge. Enlargement of the traces for windward and leeward bottom chord eyebar measured strains. Both are baseline traces of the filtered data. Thus, they represent the change in measured strain starting from the same point in time as the corresponding change in wind velocity. The wind velocity is shown for reference at the top of the graph to an arbitrary scale.

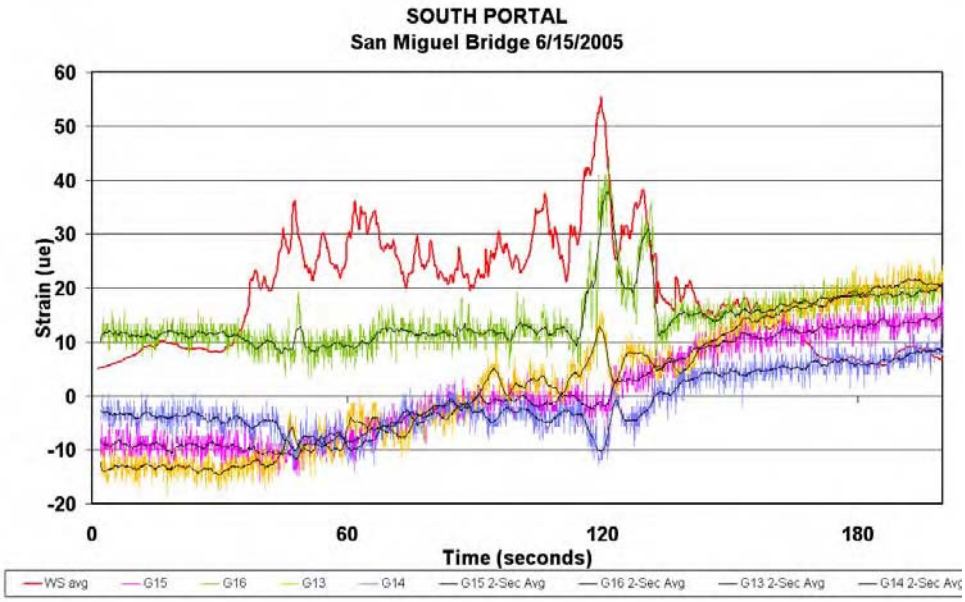


Figure 3.42. San Miguel Bridge. Measured strains at the south portal are shown. Signal drift can be seen.

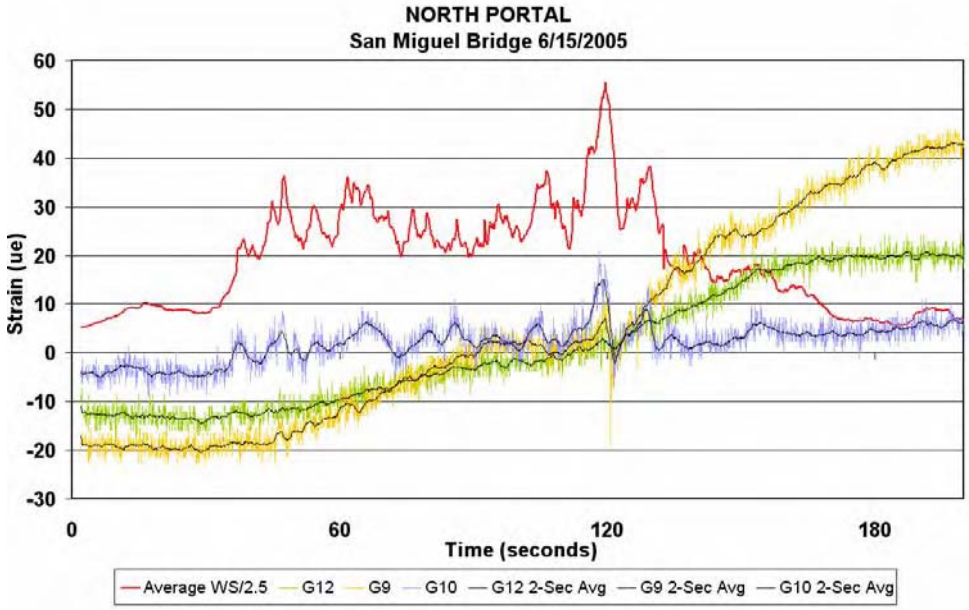


Figure 3.43. San Miguel Bridge. Measured strains at the north portal are shown. (Gage 11 was eliminated from the graph due to aberrant strain behavior, attributed to the gage being mounted adjacent to a broken member on the north portal). Signal drift can be seen.

Table 3.8. San Miguel Bridge Verification Summary. Comparison of calculated forces to measured forces expressed in kN (kips) and kN-m (foot-kips)

| Member | Calculated Force | Measured Force | Correlation: % difference |
|---|---|---|---|
| Windward bottom chord | -1.5 kN (-0.3 kips) | 0.22 kN * ( 0.05 kips) | 114% * |
| Leeward bottom chord | 4.3 kN ( 1 kips) | 9.61 kN (2.16 kips) | 55% |
| North portal upper | Broken Member | n/a | n/a |
| North portal lower | 3.9 kN-m (2.9 ft-k) | 0.99 kN-m (0.73 ft-k) | 75% |
| South portal upper | 3.1 kN-m (2.3 ft-k) | 0.92 kN-m (0.68 ft-k) | 70% |
| South portal lower | -4.6 kN-m (-3.4 ft-k ) | -2.58 kN-m (-1.9 ft-k) | 39% |

* Study of Figure 3.35 suggests the weak correlation for the bottom chords may be attributable to a probable anomaly in the field data, particularily for the windward bottom chord.

San Miguel Conclusion:

The weak correlation between calculated and measured data at windward bottom chord is due to different factors. The first factor affecting the reading is the possible drift at the time of collecting the data, possibly from slipping or movement of the the C-clamps at the transducers following the wind velocity spike. Additionally, the wind event studied was not perpendicular to the bridge; the poor correlations at the portals may be an indication of the difficulty in modeling the longitudinal components of wind pressure.

## 3.5 Rifle Bridge

Figures 3.44 through 3.54 and Tables 3.9 and 3.10 show the location of instruments and results for Rifle Bridge.

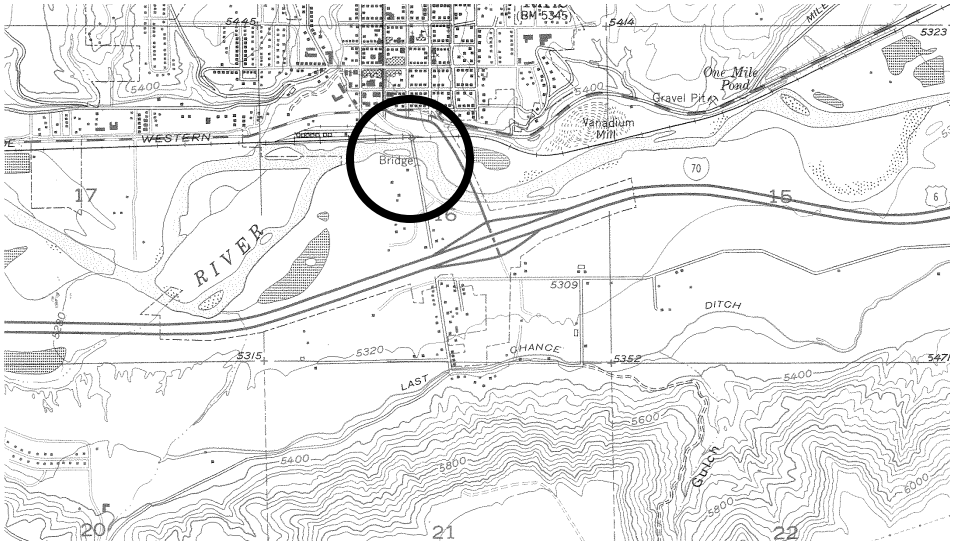


Figure 3.44. Location of Rifle Bridge. It is located between the City of Rifle, CO on the north, and Interstate 70 on the south (USGS 1982). The bridge is oriented 10° to the west from north, so local north was assumed to be global north. The winds are predominately from the west, and the Colorado River Valley in this area is very open and flat both east and west.
The bridge has been barricaded to prevent access by vehicles and pedestrians for the last 20 years.

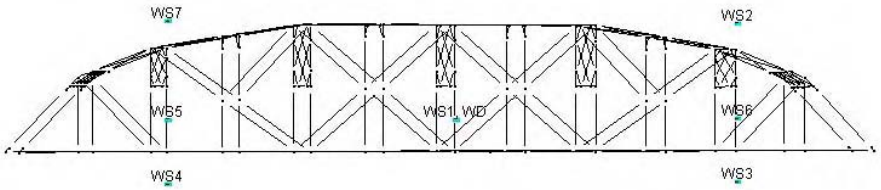


Figure 3.45. Diagram of Rifle Bridge, illustrating the locations of anemometers (WS1-WS7) and wind direction sensor. North is to the left. WS1 was positioned directly upwind of the centroid of the wind intercept area. WS2 and WS7 were located approximately 3 meters above the top of the second diagonal frame from the end, near the portals. WS3 and WS4 were positioned 2.5 meters below the bridge deck, at an elevation mid-height between the bridge deck and the water surface below.

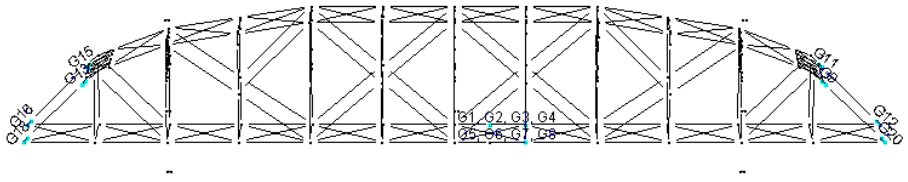


Figure 3.46. Diagram of Rifle Bridge, illustrating the locations of the strain transducers. North is to the left. The wind direction was from the west, orthogonal to the bridge. Strain transducer numbers G1-G4 were clamped to the leeward bottom chord eyebars. G5-G8 were clamped to the windward bottom chord eyebars. G9, G20, G11, and G12 were clamped to the end diagonals at the south portal. G13, G18, G15, and G16 were clamped to the end diagonals at the north portal. Although G18 replaced G16, and G20 replaced G12, G12 and G16 were used in subsequent graphs for consistency.

Table 3.9. Rifle Bridge Wind Velocities, Quadrant Average Velocities, and Quadrant Pressures.

| Anemometer | Location | Velocity m/s (mph) | Average velocity for quadrant m/s (mph) | Average pressure for quadrant Pa (psf) |
|---|---|---|---|---|
| WS1 | Central | 5.9 (13.1) | n/a | n/a |
| WS2 | South upper | 2.4 (5.4) | 3.5 (7.9) | 129 (2.70) |
| WS3 | South lower | 14.9 (33.3) | 7.7 (17.2) | 249 (5.19) |
| WS4 | North lower | 1.5 (3.3) | 4.4 (9.8) | 144 (3.01) |
| WS5 | North central | 5.8 (13) | Not used in any quadrant | Not used in any quadrant |
| WS6 | South central | 2.3 (5.2) | Not used in any quadrant | Not used in any quadrant |
| WS7 | North upper | 5.6 (12.5) | 5.8 (12.9) | 212 (4.44) |

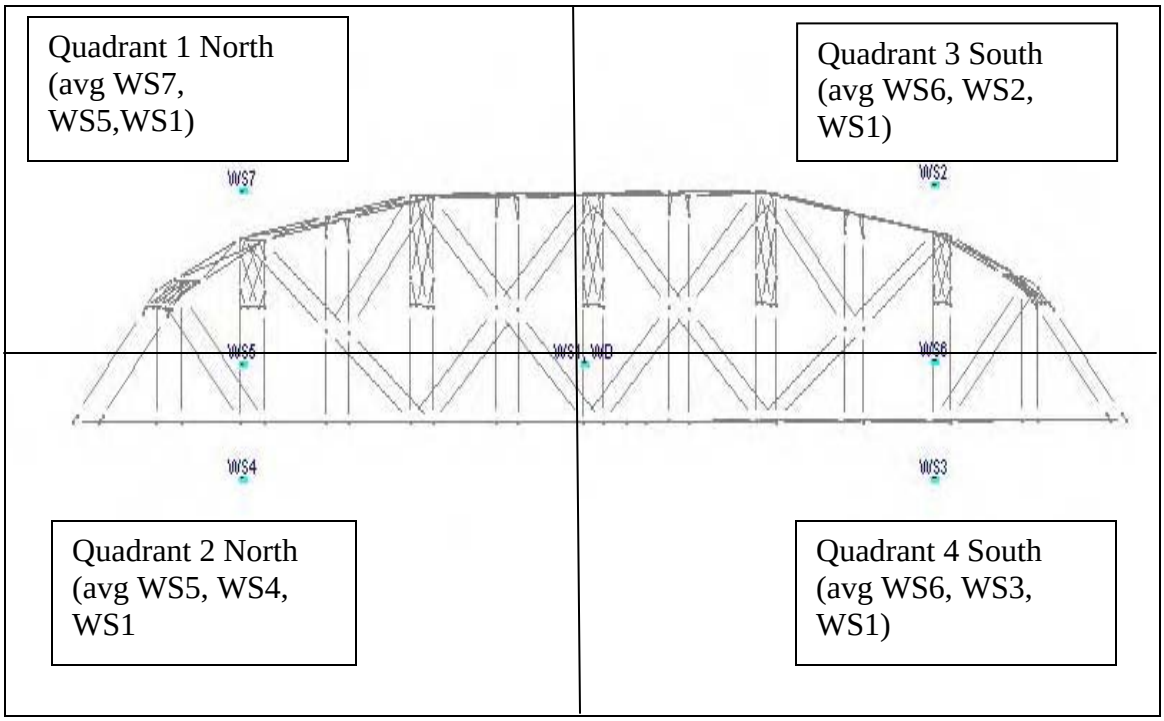


Figure 3.47. Quadrants subjected to different uniformly distributed wind pressures. Wind pressure on Quadrant 1 was determined from a weighted average from the velocities measured at WS7, WS5, and WS1. Wind pressure at the other quadrants were similarly determined.

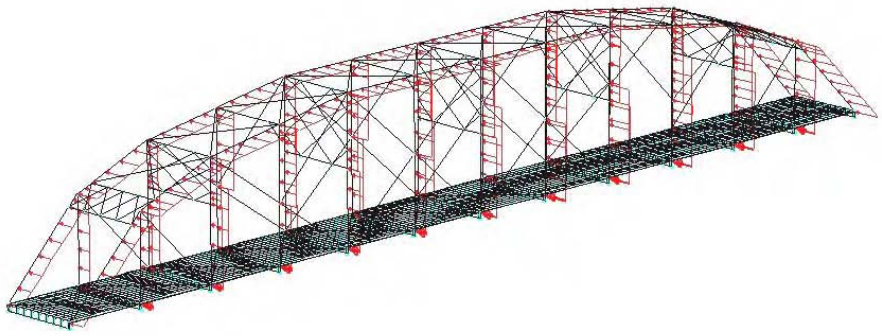

Figure 3.48. Wind pressure applied to the four quadrants for analysis. North is to the left. Another component of wind pressure from the north (not shown here) was also applied to simulate the measured wind direction from the northwest.

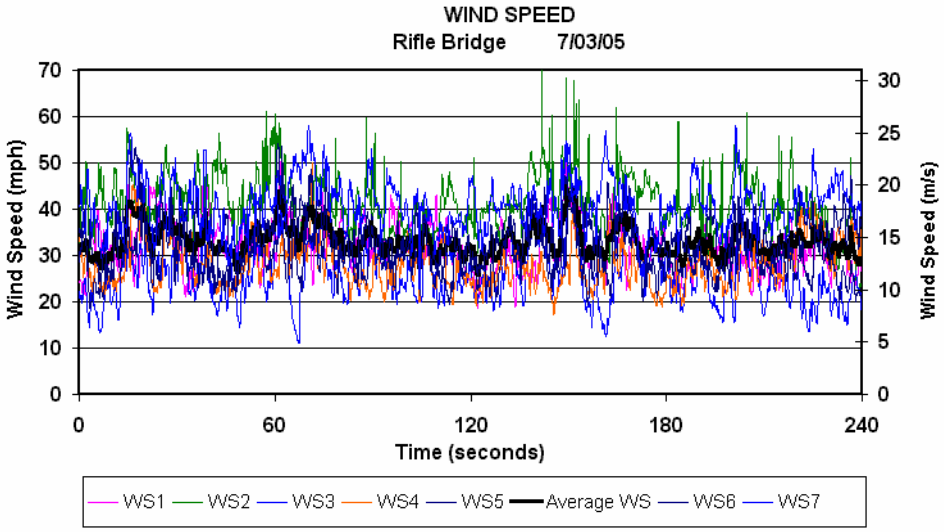


Figure 3.49. Wind speed data from seven anemometers. The heavy trace is the average of all seven, and will be used as a reference in all subsequent graphs.

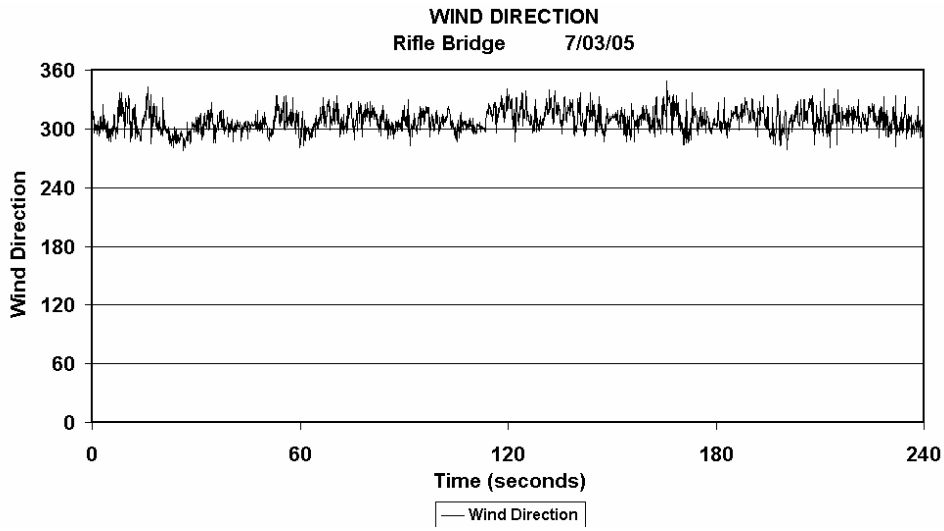


Figure 3.50. Wind direction was from the approximate northwest (310 degrees).

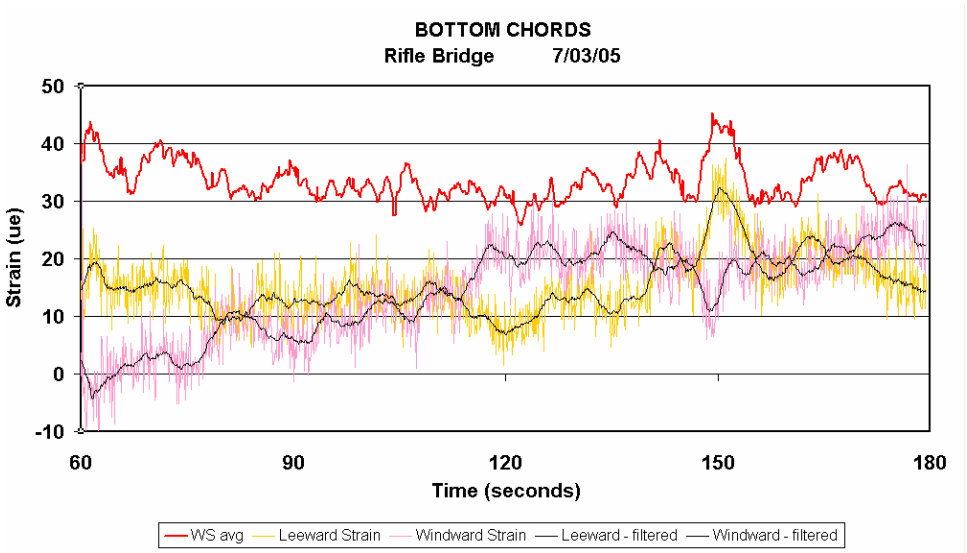


Figure 3.51. Rifle Bridge. Strain measurements for the windward and leeward bottom chord eyebars. The bold trace at the top is the average wind speed, to an arbitrary scale. Measured strain in the leeward eyebar is shown above measured strain in the windward eyebar. Both the raw data and a filtered line that removes much of the signal noise are shown.

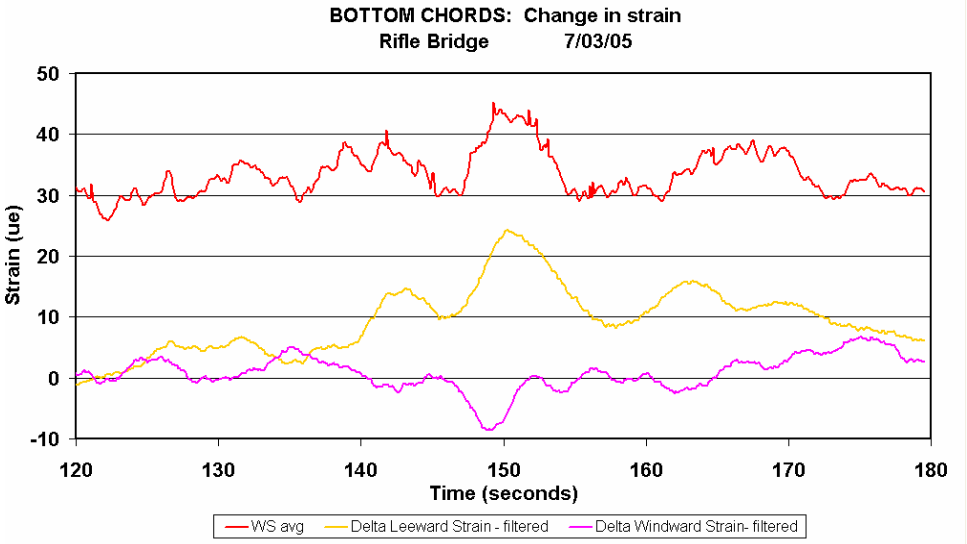


Figure 3.52. Rifle Bridge. Enlargement of the traces for windward and leeward bottom chord eyebar measured strains. Both are baseline traces of the filtered data. Thus, they represent the change in measured strain starting from the same point in time as the corresponding change in wind velocity. The wind velocity is shown for reference at the top of the graph to an arbitrary scale.

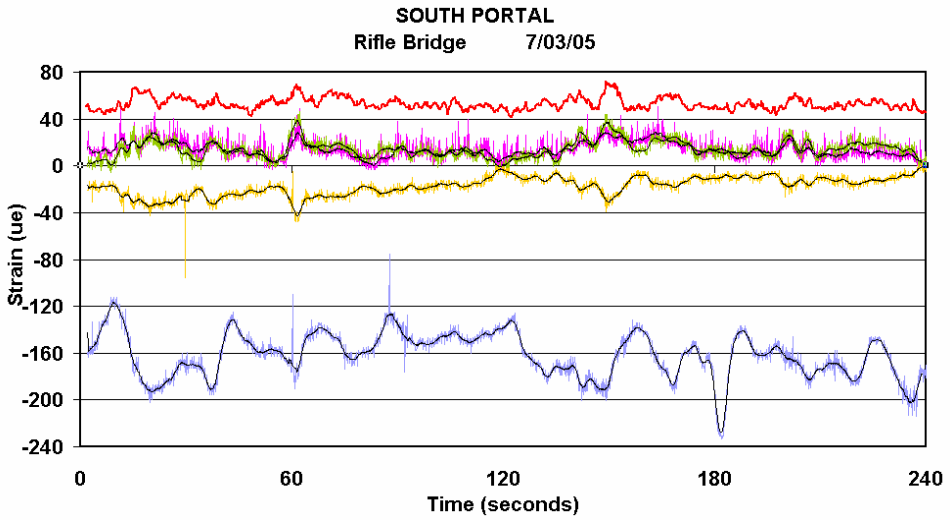


Figure 3.53. Rifle Bridge. Measured strains at the south portal are shown. Note the erratic behavior of G12, the bottom trace on the graph. It has been discounted as an anomaly.

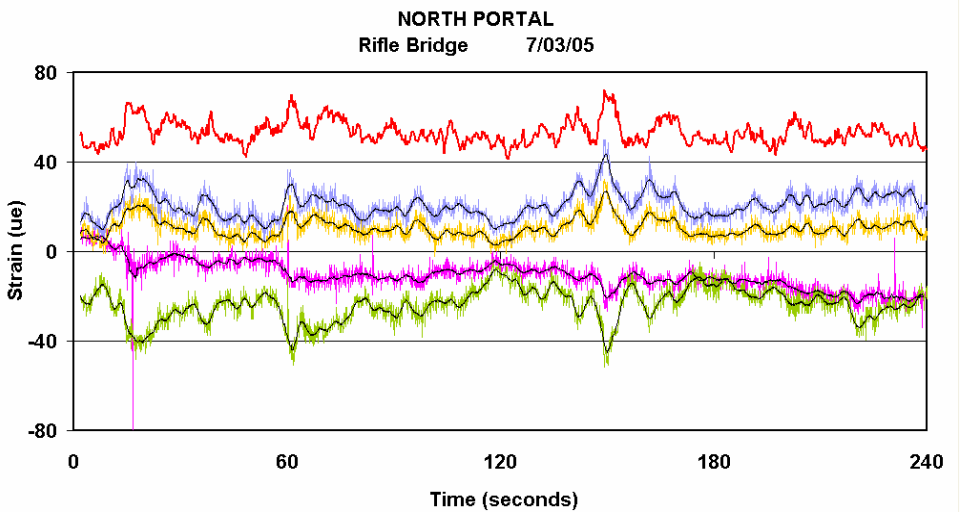


Figure 3.54. Rifle Bridge. Measured strains at the north portal are shown.

Table 3.10. Rifle Bridge Verification Summary.
Comparison of calculated forces to measured forces expressed in kN (kips) and m-kN (foot-kips).

| Member | Calculated Force | Measured Force | Correlation: % difference |
|---|---|---|---|
| Windward bottom chord | -7.34 (-1.65) | -8.41 (-1.89) | 14% |
| Leeward Bottom Chord | 8.94 (2.01) | 16.8 (3.78) | 88% |
| North portal upper | 6.01 (4.43) | 2.24 (1.65) | 168% |
| North portal lower | 10.80 (7.97) | 3.97 (2.93) | 172% |
| South portal Upper | 4.85 (3.58) | 2.13 (1.57) | 128% |
| South portal lower | 10.11 (7.46) | 5.15 (3.8) | 96% |

Rifle Conclusion:

While the windward bottom chord forces correlated well, measured forces did not correlate well with other calculated forces. Measured forces in the leeward bottom chord eyebar differed from calculated forces by 88%, suggesting a possible non-symmetry in the structure – possibly due to an outboard sidewalk on the east (leeward) side that complicated the model. Field verification of the boundary conditions at the bearings could not be field verified within the scope of this study, however boundary conditions at the north end were modeled as shown in Appendix C and at the south end similar to Appendix C with an additional translation release in the longitudinal direction. Additionally, the wind event studied was not perpendicular to the bridge; the poor correlations at the portals may be an indication of the difficulty in modeling the longitudinal components of wind pressure.

## 3.6 Conclusions

Table 3.11. Calculated vs. measured values for windward bottom chord for all five bridges (summarized from Tables 3.2, 3.4, 3.6, 3.8, and 3.10).

| Bridge | Calculated Force kN(kips) | Measured Force kN (kips) | Correlation (% difference) |
|---|---|---|---|
| **Fruita** Timber deck on timber stringers | -1.37 (-0.31) | -1.44 (-0.32) | 5 % |
| **Prowers** Asphalt pavement on corrugated metal decking on steel stringers | -2.71 (-0.61) | -3.11 (-0.70) | 14 % |
| **Blue River** Orthogonal timber deck on steel stringers | -0.44 (-0.1) | -0.54 (-0.12) | 23 % |
| **San Miguel** Gravel roadbase on CMP segments on steel stringers | -1. 5 (-0.35) | 0.22 (0.05) * | 114% * |
| **Rifle** Asphalt pavement on corrugated metal decking on steel stringers | -7.34 (-1.65) | -8.41 (-1.89) | 14 % |

* Probably field data anomaly.

Bottom Chords: The correlations shown in Table 3.11 suggest the deck models are reasonable representations of the skeleton plus deck for use as analytical models. As we accept the deck models as accurate, it can be concluded that the decks provide additional lateral stiffening and help resist wind load.

Portals: In all cases, field measurements revealed bending moments in the lower portals. This suggests restraint from rotation at the bearings as shown in Appendix C. The common assumption of pinned boundary conditions, at least for the (relatively low) wind velocities experienced in these tests, is shown to be inaccurate.

## APPENDICES

# APPENDIX A VERIFICATION METHOD

## A.1 Verification Testing

Field measurements were made at each of the bridges to verify that the deck models were reliable. While the AASHTO-specified wind pressure of 3.59 kPa (75 psf) – which corresponds to approximately 194 km/hr (121 mph) – would not occur, the actual wind velocity could be measured during a test, and the actual test pressure deduced from that. Strains at selected members were measured at the same time. The deck models were then run using the measured wind pressures instead of AASHTO –specified wind pressure. The deck models were further modified to reflect actual configurations. Such modifications included:

- Wind pressures deduced from the measured velocities were input as the lateral load.
- Input of boundary conditions to better reflect the actual conditions at the supports.
- Removing internal member-to-member releases to better reflect the actual end rotations of internal members.

In these ways, the analytical models were adjusted to approximate the conditions at the time of the measurements. Then the measured strains were compared to the calculated strains. This was compared to actual strain measurements.

## A.2 Test Set-Up

Instrumentation was set up at the bridges and data was collected during windy conditions. The instrumentation system was designed to obtain measurements of wind

speed, wind direction, and strains from selected members all at a rapid sampling interval. The instrumentation system at each bridge was similar, and is described below.

A total of five (or seven) anemometers were used to obtain wind speed data at multiple locations virtually simultaneously. A wind direction sensor was used to determine the direction of the wind with respect to the bridge orientation. A single wind direction sensor was used because the wind direction was expected to remain consistent over the length of the bridge span. Strain data was obtained at sixteen different locations. The locations of greatest interest were the bottom chord eyebars at mid-span and potential high-moment regions of the portal frames. These locations were selected because of relatively high anticipated axial forces or moments due to lateral load.

## A.3 Instrumentation System

A schematic diagram of the instrumentation system is shown in Figure A.1.

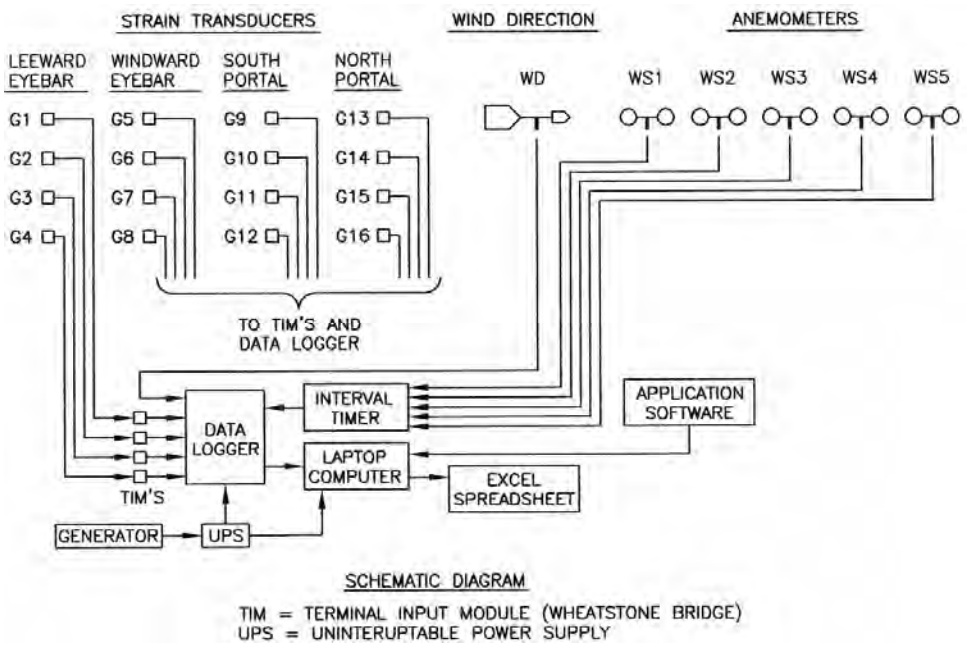


Figure A.1. Schematic diagram of instrumentation system.

## A.4 Instrumentation Components

The individual instruments are described below.

### A.4.1 Strain Transducers

Each strain transducer consisted of a steel ring with a strain gage adhered to the inside surface as shown in Figure A.2. Model CEA-06-250UW-120 strain gages, manufactured by Vishay Micro Measurements Group, were used. The gage factor for all strain gages was 2.065. The ring was attached to two steel angles, which were used for clamping the transducer to the member being studied. Fundamentally, the transducers sense axial strain, which is amplified by flexural deformation of the ring. The true strain in the member under study is obtained by multiplying the transducer strain by a predetermined factor, which had been determined theoretically and confirmed

experimentally by Herrero (Herrero, 2003). The strain gage in the transducer is considered a quarter bridge strain gage because it constitutes one of four resistors in the Wheatstone bridge circuit.

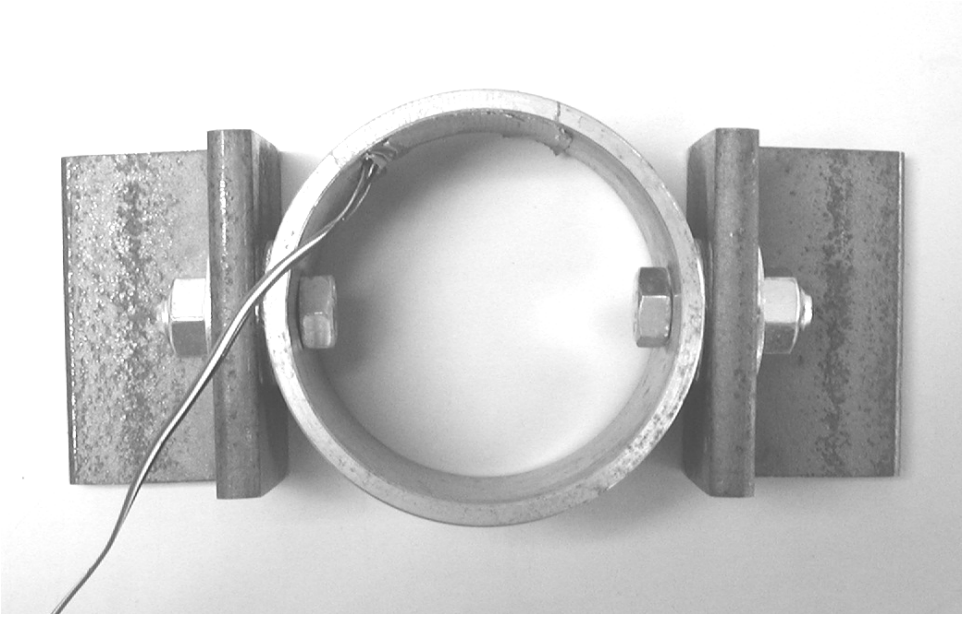

Figure A2. Strain transducer. It consists of a 3" diameter steel ring, bolted to steel angles. The strain gage is on the inside ring surface, 90 degrees from the axis of the bolts.

### A.4.2 Wheatstone Bridge

Each of the sixteen channels for the strain signals had an in-line Wheatstone bridge. The circuitry for the bridges was provided by Campbell Scientific model 4WFB120 Terminal Input Modules (TIM's), shown in Figure A.3. These are 4-wire full bridge devices. They are manufactured as relatively small modules with pins that fit into the channel terminals on the data logger. The resistor in the bridge circuit that matches the nominal resistance of the quarter bridge strain gage has a resistance of 120 ohms plus or minus a tolerance of 0.01% (Campbell Scientific. 1996b). Because the actual change

in resistance of the strain gage is small, a full bridge configuration was used to give the maximum resolution. A "quarter bridge" strain gage is so named because the strain gage becomes one of four resistors that make up a full bridge. The TIM module provides the other three resistors.

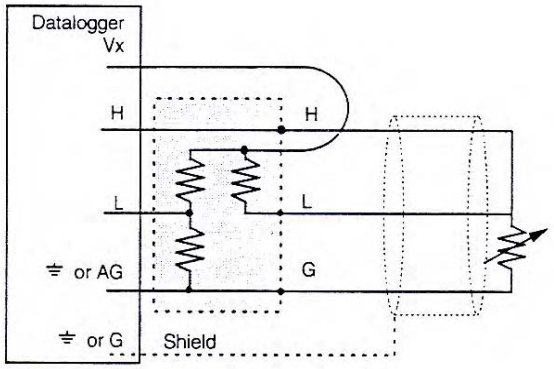


Figure A3. Full bridge wiring diagram for Terminal Input Module (TIM). The variable resistor represents the strain gage. The other three resistors are contained within the TIM. The TIM connects to the data logger via three pins (labeled H, L, and AG in the diagram). Excitation voltage is supplied from the data logger via the lead labeled Vx (Campbell Scientific 1996b).

### A.4.3 Anemometers

R.M. Young model 03101-5 anemometers, shown in Figure A.4, were used. They have three cups connected to wheel on a vertical shaft. The shaft drives an AC generator, which produces a sine wave output voltage signal directly proportional to the wind speed. One complete sine wave cycle is produced for each cup wheel revolution (Campbell Scientific 1996a).

### A.4.4 Wind Direction Sensor

The wind direction sensor, also shown in Figure A.4, was a R.M Young Model 03301-5 Wind Sentry Vane. A vane rotates with the wind, and positions itself parallel to the wind direction. The vane is connected to a shaft that turns a potentiometer. As the vane rotates in the wind, the potentiometer changes electrical resistance. An excitation voltage is applied and from measurement of the voltage drop the wind direction can be determined (Campbell Scientific 1996a). The wind direction sensors were oriented on the bridges such that north (0 degrees and 360 degrees) was aligned with the longitudinal direction of the bridge. Thus the term "north" as used herein is not true north, but local bridge north. Consequently, a wind from the local west direction (270 degrees) would be transverse to the bridge.

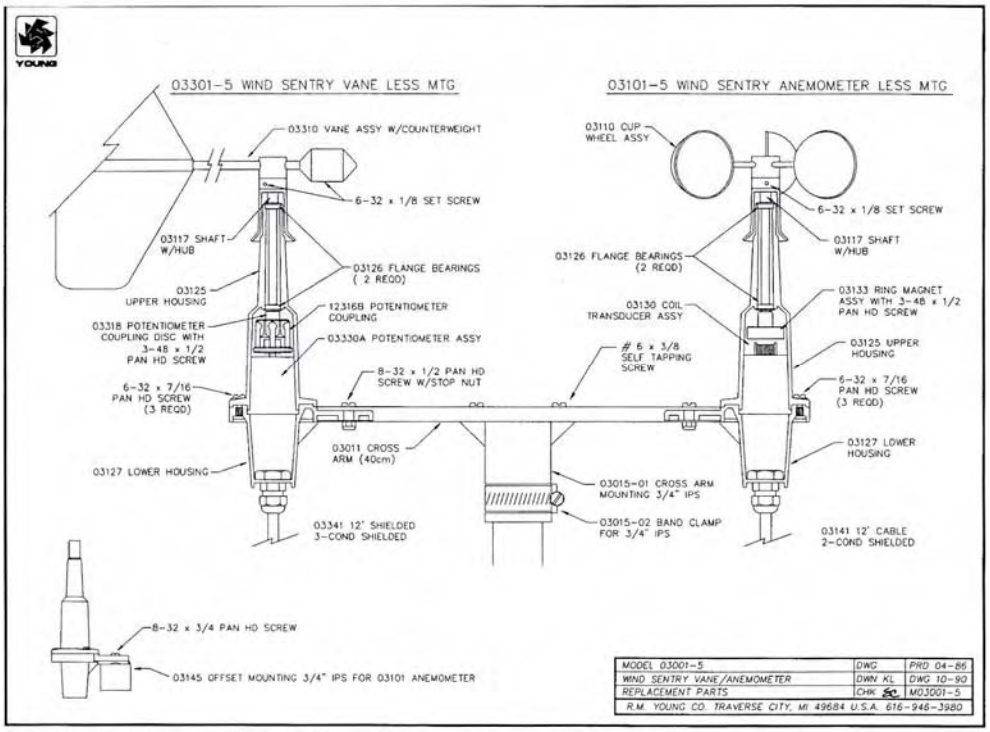


Figure A.4. Anemometer and wind direction sensor. They are of corrosion-resistant construction, with stainless steel shafts, precision instrument ball bearings, and lubricated with a wide temperature range high quality instrument

oil. (Campbell Scientific 1996a).

### A.4.5 Interval Timer

A Campbell Scientific model SDM-INT8 interval timer, shown in Figure A.5 was used to receive and process the continuously-generated AC sine wave voltage signals from the anemometers, and to download processed data to the data logger for logging. Five of its eight channels were used - one for each anemometer. For these tests, the data was processed as follows:

- The rising edges of the sine wave voltage signals were timed.
- The time interval between rising sine waves was then downloaded to the data logger.
- The data logger processed this information into wind velocity, in units of either meters per second or miles per hour.


Figure A.5. Interval Timer.

### A.4.6 Data Logger

A Campbell Scientific model CR5000 data logger was used. The CR5000, shown in Figure A.6, makes measurements from numerous channels at sampling intervals up to 5000 Hz. (Campbell Scientific 2001). For these experiments, 17 channels were used for analog inputs: 16 channels for Wheatstone bridge measurements (associated with the 16 strain transducers) and one channel for wind direction measurements. The logger provided excitation voltage for these devices, and measured the voltage drop. The five anemometers were connected via the interval timer to one of two pulse counters on the data logger. Data was stored in tables in the logger. Each collection of data was stored in a separate table, all of which were downloaded to a laptop computer.

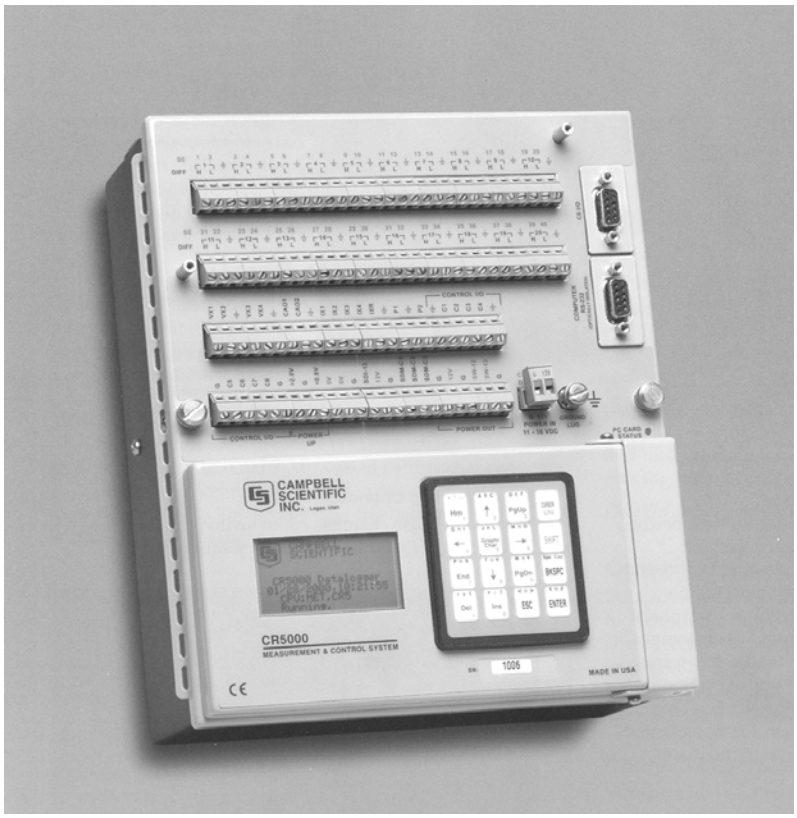


Figure A.6. Campbell Scientific CR5000 Data Logger (Campbell Scientific 2001).

### A.4.7 Software

PC9000, intended for use in conjunction with the CR5000 datalogger and available from Campbell Scientific, was the application software used (Campbell Scientific 2001). In addition to creating the data tables, PC9000 includes various ways to monitor datalogger data files in real-time. PC9000 was accessed from another program, called VALNEW5 that was developed at Campbell Scientific specifically for these experiments. A program listing for VALNEW5 is included in Appendix D. Each data table contained a record date and time stamp, the five wind speeds, the wind direction, and the sixteen strain transducers' outputs, all logged at a sampling rate of 0.1 seconds (10 Hz).

### A.4.8 Cables

Each strain gage had copper lead wires of 26 American Wire Gauge (AWG) soldered to its terminals. Each strain gage lead wire was 2.1 meters (7 feet) long. Thus the resistance of the gage lead wires was the same for all strain gages. Three wires, shown in the wiring diagram in Figure A.3, were used for the circuit at each gage, discussed further in Section A.6.2

The cables used for connecting the lead wires to the data logger consisted of three 18 AWG copper wires with PVC insulation, all wrapped inside a foil shield, and bundled into a PVC sheath. These wires were connected to the three lead wires from the strain gages at one end and to the Terminal Input Modules (TIM's) at the other. The cables

varied in length from 24 meters (80 feet) to 76 meters (250 feet), and were labeled such that a specific length cable served a specific strain transducer. In this way the resistance of each cable was accounted for during the computation of the strains. The foil shield was grounded to the data logger to provide shielding from spurious electrical signals.

The cables for the anemometers and wind direction sensor were specialty items, manufactured specifically for this purpose. They were Campbell Scientific model 9661 with 22 AWG twisted pair lead wires in santoprene, a durable polypropylene insulation. They were all 38 meters (125 feet) long.

### A.4.9 Temperature Measurement

For all the bridge tests except Fruita Bridge, temperature was sensed by a Campbell Scientific thermocouple and the temperature data was logged with all the other data. For the Fruita Bridge tests, a mercury thermometer, manufactured by the Springfield Instrument Company, was used to determine air temperature during the experiments. This data was recorded manually, along with the time of the reading.

Figure A.7. Anemometer (WS1) and Wind Direction sensor (WD) installed at Fruita Bridge. They are located directly upwind of the centroid of the wind intercept area of the bridge.

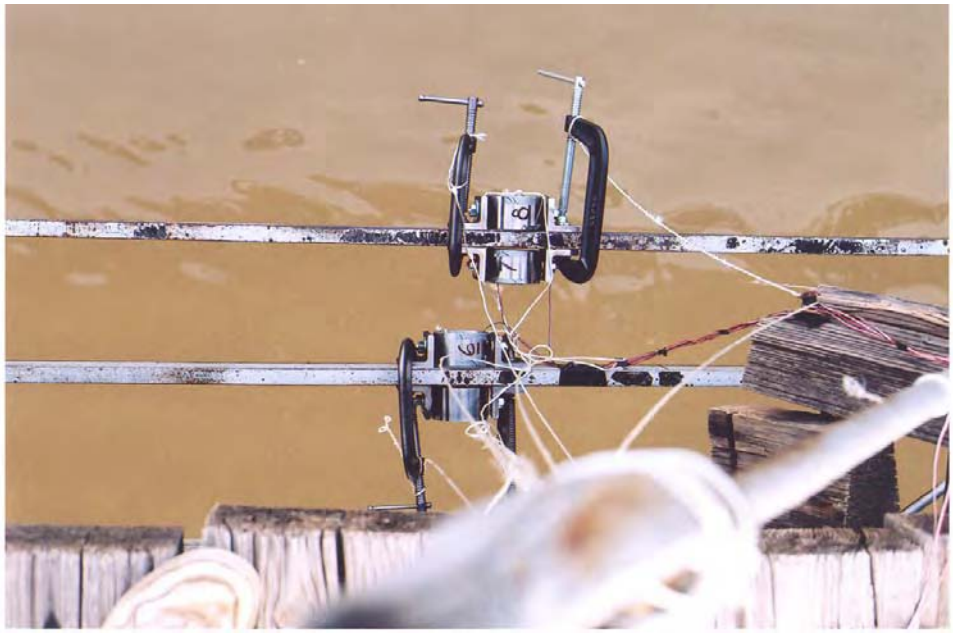

Figure A.8. Strain transducers installed on bottom-chord eyebars at Fruita Bridge. The view is looking down. Each component has a lanyard attached to it, as a precaution against falling into the river below.

Figure A.9. Strain transducer installed on a portal at Fruita Bridge. It is located at the same elevation as the panel point of the portal's knee brace.

## A.5 Wind Speed Data

The data table containing the highest wind speed logged during testing was selected for study. See Part 3 for specific locations of the wind instruments.

With the data being logged at intervals of 0.1 second, the wind speeds from a single anemometer showed considerable fluctuation over very short time intervals.

The wind direction sensor was installed parallel to the bridge orientation, such that its north direction was toward the bridge's northeast portal. The term "north", as used herein, refers to this local north, defined as the northeast end of the bridge.

Rather than use absolute values of wind velocity, the difference between high and low velocities were used in this study. This was done out of a concern that at low wind velocities, the strain measurements might not be accurate owing to potential slack in the many component member connections in the bridge. It was thought that some minimum level of wind pressure, and thus velocity, was necessary to displace the members sufficiently to remove "slack" from connections. Until all the "slack" is taken up, the strains would not be proportional to wind pressure and thus to the wind velocity. Differential velocities associated with the maximum measured wind velocity were selected to reduce the potential for "slack" as much as possible.

- The "low" velocity corresponds to the average of 20 consecutive data measurements (over a two-second interval). The two-second intervals were selected to coincide with "low" values at the base of the spike and "high" values were selected to coincide with the peak of the spike.

## A.6 Strain Data

Data from the strain transducers required processing to:

- Make a temperature correction for the gage factor.
- Make a temperature correction for thermal effects on the strain transducers.
- Make a correction for the resistance of the lead wire that was outside of the arms of the Wheatstone bridge.
- Filter out signal noise.

- Zero the data.

The methodology for making these corrections is discussed in the following sections.

### A.6.1 Cable Resistance

Because of their length, the resistances of the lead cables were significant with respect to the resistance of the strain gages. The additional resistance of the cable, called "lead wire," reduces the sensitivity of the Wheatstone bridge output. The resistance of the lead cables was accounted for by modifying the gage factor as follows:

$$GF_{revised} = GF_{initial}\left[\frac{R_g}{(R_g + R_l)}\right] \quad \text{(A.1)}$$

where:
$GF_{initial}$ = Gage factor of "stand alone" strain gage after temperature correction
$GF_{revised}$ = Adjusted gage factor that accounts for lead resistance
$R_g$ = Resistance of strain gage (120 ohms for this case)
$R_l$ = Resistance of lead wire (Vishay 2004)

The resistance of the 26 AWG copper strain gage lead is 0.138 ohms/meter (0.041 ohms/foot). The resistance of 18 AWG copper cable is 0.0209 ohms/meter (0.006385 ohms/ foot). (Belove 1986).

Lead wires were connected with one wire to one gage terminal, and two to the other terminal. The lead wires for each gage were the same length and routed together so all experienced similar temperature fluctuations. By use of this wiring method, shown in Figure A.3, the resistance of the two lead wires within the two arms of the Wheatstone

bridge and the resistance changes of the leads due to temperature fluctuations were self-compensating (Campbell Scientific 1996b).

### A.6.2 Strain Computation

Strain was computed as:

$$\varepsilon = \frac{4V_r}{GF(1-2V_r)} \qquad \text{(A.2)}$$

With: $$V_r = \frac{V_{out}}{V_{ex}} \qquad \text{(A.3)}$$

Where:
$\varepsilon$ = Strain
$GF$ = Gage Factor, after temperature adjustment and adjustment to account for lead wire resistance
$V_{out}$ = Measured bridge output voltage
$V_{ex}$ = Excitation voltage (Campbell Scientific 1996b)

The ratio of output voltage to excitation voltage, $V_r$, was used because:

- The data logger uses a ratiometric measurement technique that allows this ratio to be more accurate than a simple measurement of output voltage.
- This ratio can be conveniently used in the strain calculation.

The derivation of Equations A.2 and A.3 can be found in the *Instruction Manual for 4WFB120* (Campbell Scientific. 1996c).

### A.6.3 Rolling Averages

Variations in the strain signals were apparent. These were attributed to electrical noise because the strain measurements were in the milli-volt and micro-volt range, very

low voltages that are subject to disruption from even the slightest of disturbances. Similar electrical noise had been previously identified and isolated in the laboratory work that preceded the field experiments. In contrast, the anemometer measurements were in the 0.1 – 0.3 volt range, several orders of magnitude higher.

The raw data was filtered to reduce the effect of noise and to clarify overall trends in the data. This was accomplished by taking a rolling average (sometimes called running average) of several consecutive data points and advancing the average by the sampling interval of 0.1 second. A 0.5-second rolling average would include five consecutive data points at 0.1 sec intervals adding up to 0.5 seconds, and advancing the average at intervals of 0.1 second. A 10-second rolling average would include 100 consecutive data points at 0.1 sec intervals adding up to 10 seconds, and advancing the average at intervals of 0.1 second. As an example, the raw data for Gage 5, located at the upper southeast portal at the Fruita Bridge, which includes all recorded noise, is shown in Figure A.11. The same data is shown in Figures A.12, A.13, and A.14 at rolling averages of 0.5-seconds, 3-seconds, and 10-seconds respectively. Note that the data curve becomes smoother as the duration of the rolling average increases. This has the effect of filtering out noise, but caution must be exercised, because the technique can also filter out valuable signal information.

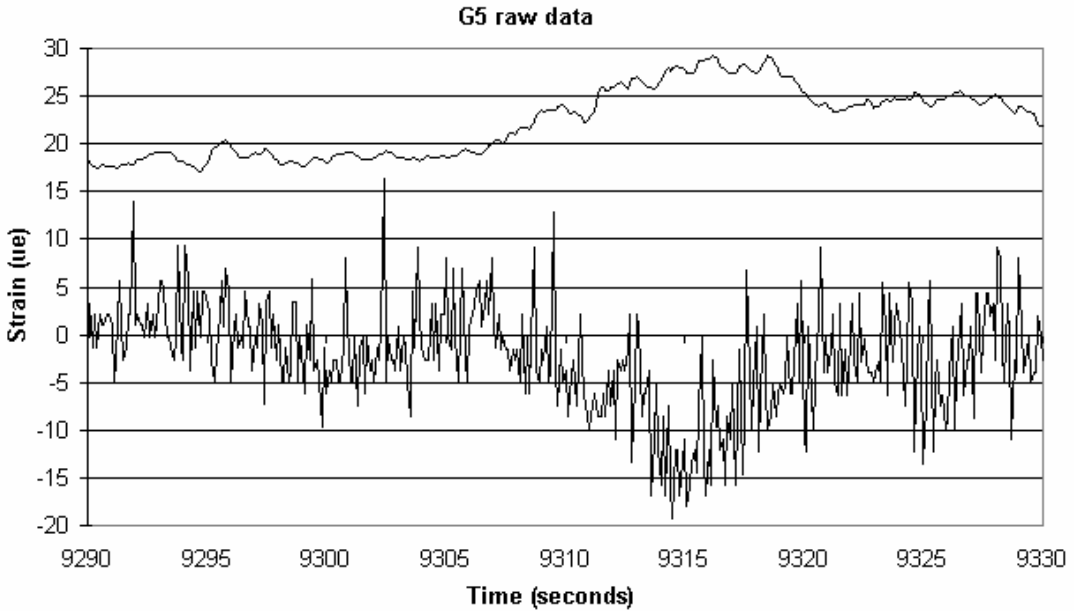


Figure A.11. Raw data from G5, unfiltered. The average wind velocity is shown at the top of the graph, to an arbitrary scale. Both the amplitude and frequency of the variations in the G5 data are greater than the variations in the wind velocity data. It seems very improbable that actual strain (a mechanical response to load) in the member varies at a rate greater than the rate of variation in wind pressure (which, as a function of velocity, would vary at the same rate as the wind velocity shown here). The difference in rate of variation is attributed to electrical noise.

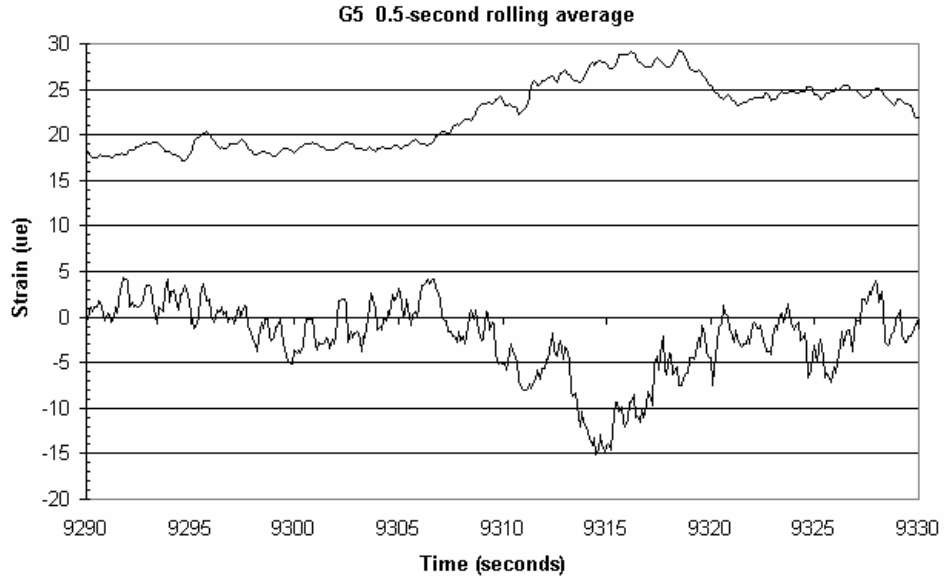


Figure A.12. Same data from G5 filtered by use of a 0.5-second rolling average. Again, the wind velocity is shown at the top. The amplitude and frequency of variations is reduced from those of Figure A.11, but both are still greater than the variations in wind velocity.

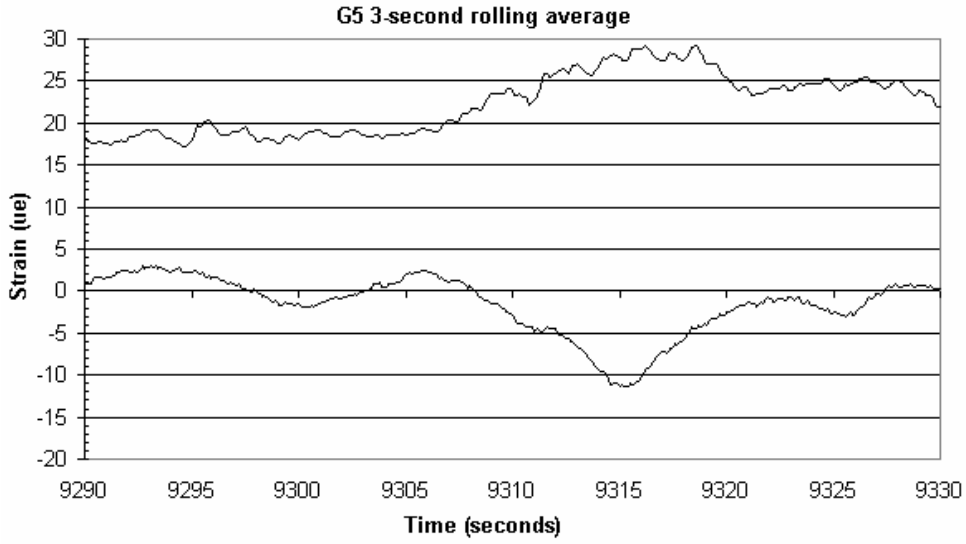


Figure A.13. The same G5 data, filtered by use of a rolling average over 3 seconds. The amplitude and frequency of variations are of a similar order as those of the wind velocity, shown at the top of the graph.

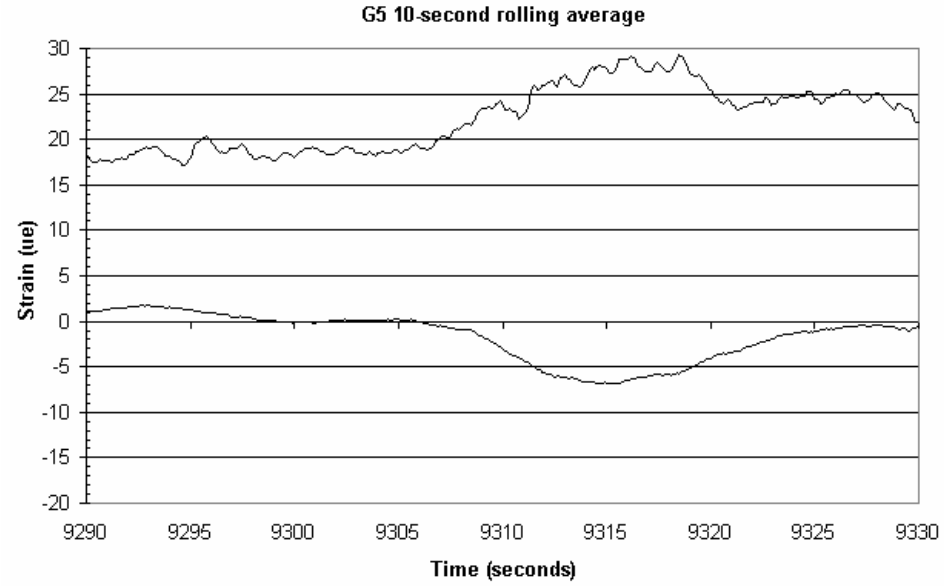


Figure A.14. The same G5 data filtered by use of a 10-second rolling average. The variations in the strain data are now less than those of the wind velocity. The strain trace now appears to be "smoothed out" too much. (If this were taken to an extreme, the G5 data could be averaged over the entire period of the graph, resulting in a straight line – the average of all the G5 data points.)

After study of durations (including others not shown above) from 0.5 seconds to 1.0 seconds, the 2-second rolling average represents the closest match to the amplitude and frequency of variations in the wind velocity curve. For the remainder of this study, the 2-second rolling average has been applied to all strain data.

## A.7 Determination of Actual Wind Pressure

The following procedure was used to determine wind pressures for use in the verification models from the wind velocity data that was obtained from the five (or seven) anemometers.

1) Determine wind pressure from wind speed data for each anemometer. Use the same wind speeds for the "high" and "low" points from the data that were used for the strains.

   Method:
   At sea level: $p = 0.00256\ V^2$ (Basic relationship, can be found in many texts)

   where: $p$ = stagnation pressure (psf)
   $V$ = velocity (mph)

   Pressure at the location of each anemometer is determined from:

   $$p = C_d\ C_a\ 0.00256\ V^2$$

   where $C_d$ = 2, which is the Drag Coefficient (also known as Shape Factor) for most "bluff bodies" such as structural shapes (ASCE 1961). $C_a$ is determined from information in ASCE 7-02, Table C6-1 (ASCE 2002).

   $C_a$ = ratio of Average Ambient Air Density for the elevation of the bridge to the Average Ambient Air Density at sea level. $C_a$ is simply a correction for actual air density.

Example: For Fruita Bridge (elevation 4500 feet) for 30 mph:
$C_a$ = 0.06685/0.0765 = 0.87.
(The 0.06685 term was interpolated from Table C6-1 in ASCE7 2002).
$p = C_d\ C_a\ 0.00256\ V^2$ = (2)(0.87)(0.00256)($30^2$) = 4.0 psf

2) A diagram is made to illustrate the relative location of anemometers on the bridge. Ex. Fruita Bridge:

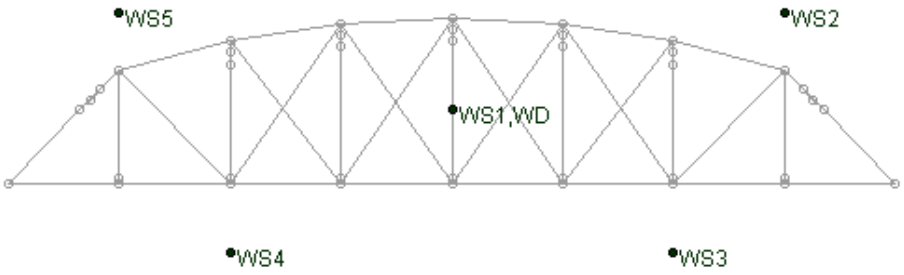


Figure A.15. Example of location of anemometers and wind direction sensors.

Determine reasonable wind pressures for different parts of the bridge. One method is to determine interpolated wind pressure at each of four "Quadrants", illustrated below:

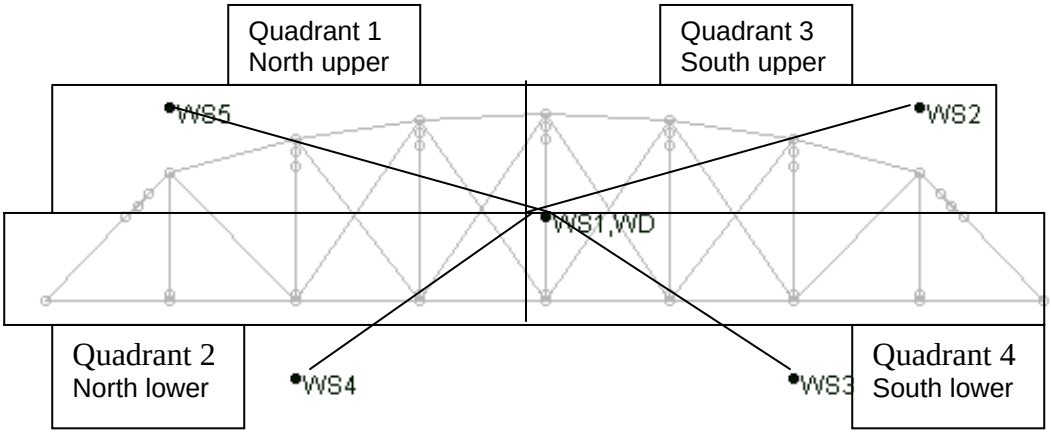


Figure A.16 . Quadrants subjected to different uniformly distributed wind pressures. Wind pressure on Quadrant 1 was determined from a weighted average from the velocities measured at WS5 and WS1. Wind pressure at the other quadrants were similarly determined.

Then apply the wind pressures to the 3D verification model.

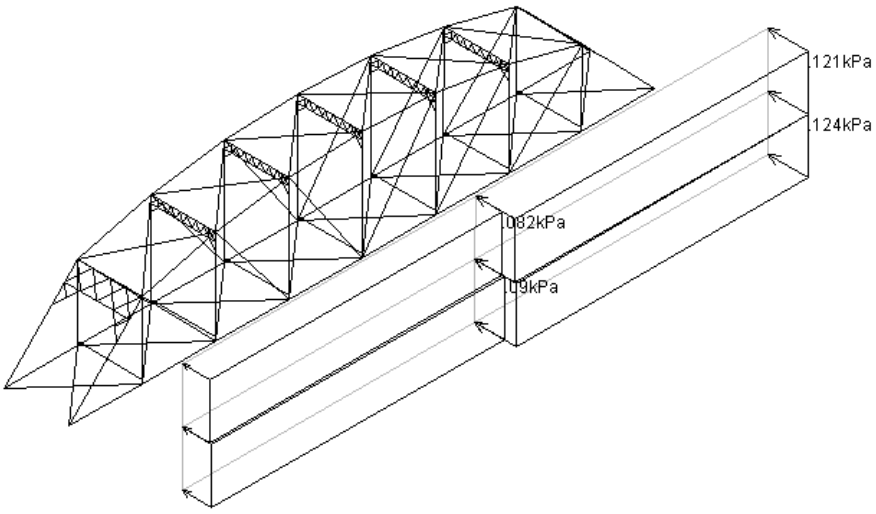


Figure A.17. Wind pressure applied to the four quadrants for analysis. North is to the left.

3) Next, modify the RISA 3D deck model, to more accurately model the actual conditions:
    a. Change the four main bearings to "fixed" if the real bearings are frozen in rust and dirt. Use some other boundary conditions if they better approximate the real conditions.
    b. Leave the bearings at stringers as "rollers" (unless there is reason to think they are something else).
    c. Change the internal releases to "fixed", except for the ends of rods, which are still "released". Note that there is probably no rotation at the ends of riveted or bolted members under the relatively low wind pressures that were measured.

4) Run the verification model.

5) From the result, make a list of the axial forces in the same bottom chord members as were instrumented in the test. Also list axial plus bending moment in the portal members.

6) Compare the verification model results to the results from the measured data.

## APPENDIX B. PC9000 DATA RETREIVAL PROCEDURES FOR DATA ACQUISITION

1. Attach the Serial Cable to the CR5000 Logger in the RS-232 port as shown in Figure B.1.

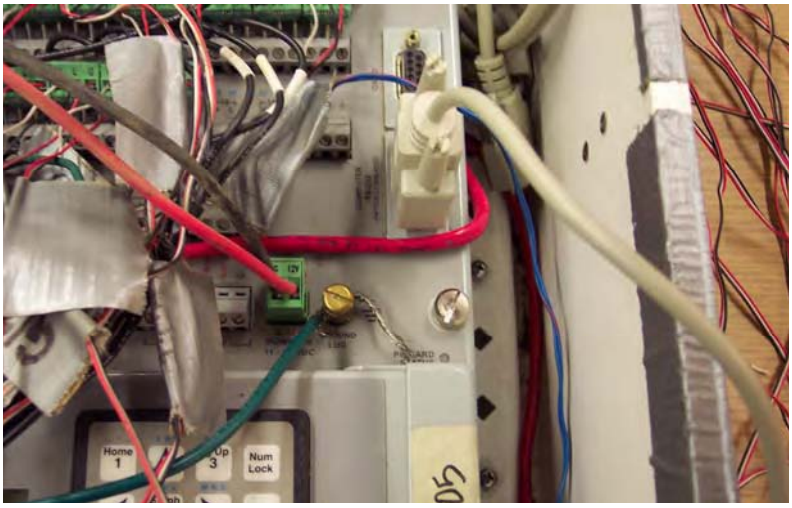


Figure B.1

2. Attach the Serial Cable to the field laptop as shown in Figure B.2.

Figure B.2

3. Turn on the filed laptop and click on the PC9000 icon to open the program as shown in Figure B.3.

Figure B.3

4. Click on the Press To Change Comm Port Button to select the port for communication to the CR5000 logger if the Communication Port does not reads Com1 or Com2. If the Comm Port is correct, click on the OK button as shown in Figure B.4. For the CR5000 logger, use Com1 or Com2 ports only.

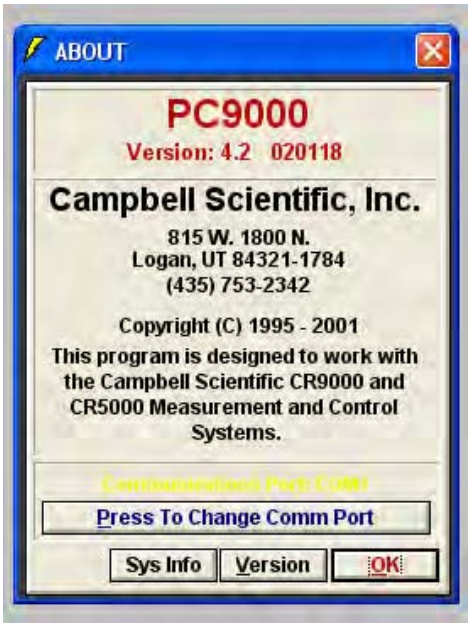


Figure B.4

5. From the pull down menu, click Collect then Data Retrieval as shown in Figure B.5. The Collect Data Screen will appear as shown in Figure B.6.

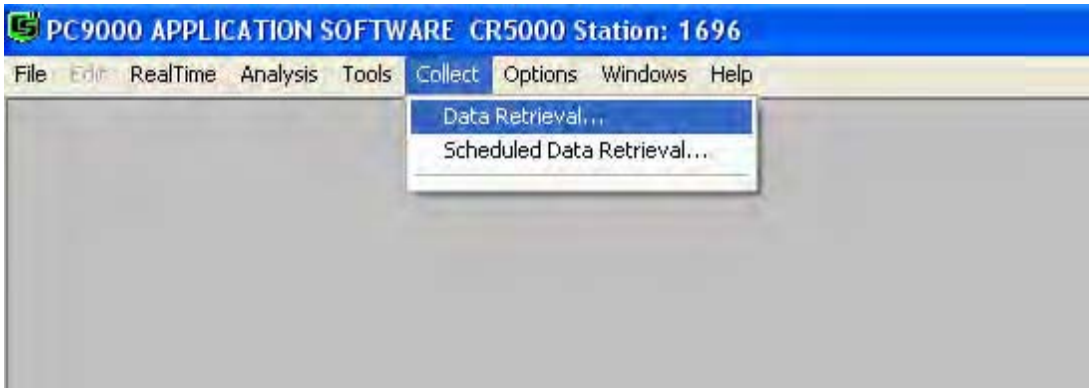


Figure B.5

6. Under the Collection Method, select the Numbers of Records, Create New File. Enter 0 to the Start Field and enter 15550 into the Count Field Box as shown in Figure B.6.

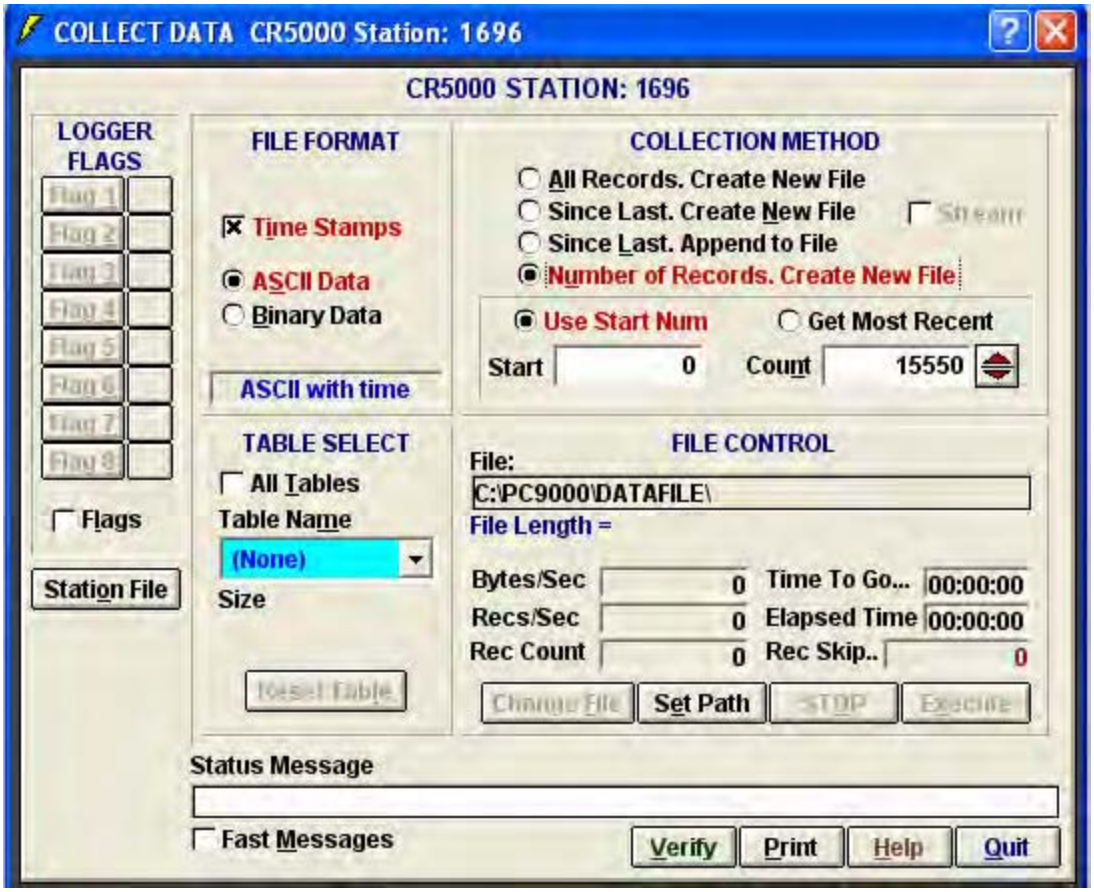


Figure B.6

7. Under the Table Select Section, select Strain20 table. Under the File Control Section, click the execute button as shown in Figure B.7. A status message reads records number during the downloading process. Repeat this step for Strain30, Strain40, Strain50, and Strain60 table.

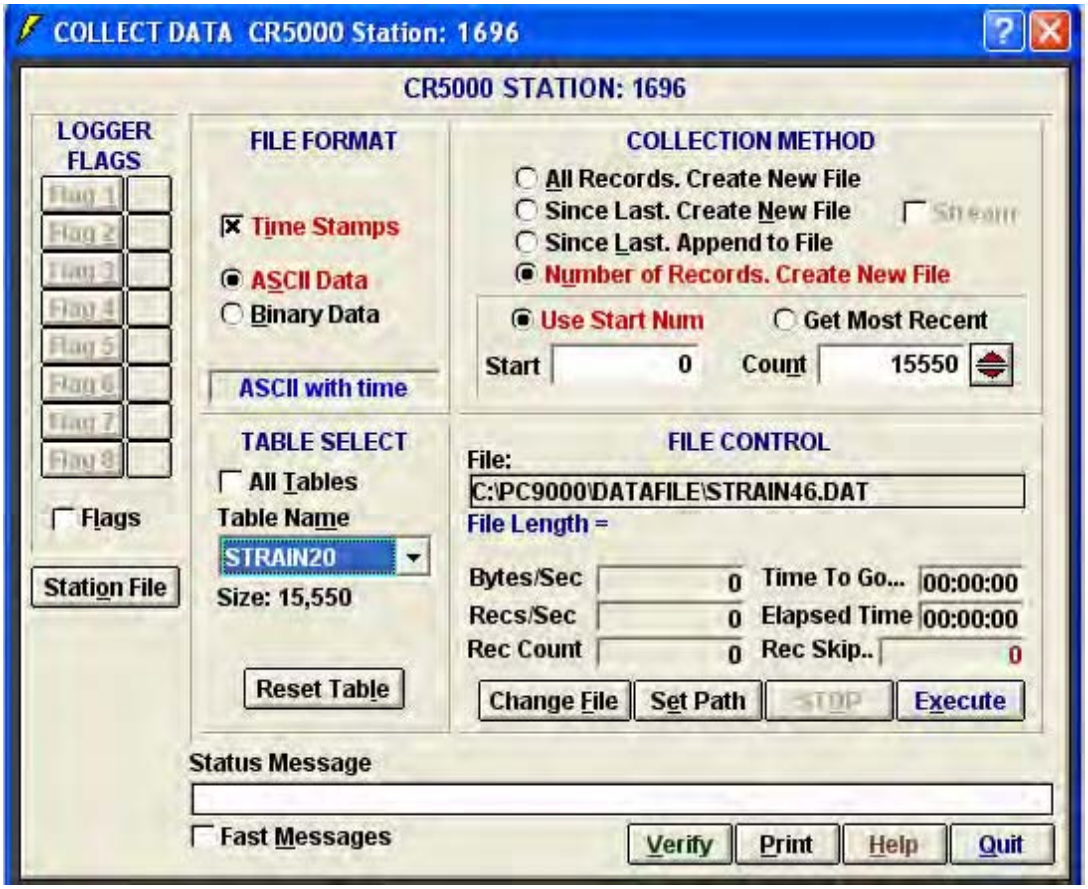


Figure B.7

8. Check each strain data table file with Excel. Each strain table can have five events up to 15550 lines of recorded data. Each event has 3110 records. Make sure each data event table has been downloaded to the field laptop.

9. Under the Table Select Section, select Strain20 table and click on the Reset Table button. A warning message will appear as shown in Figure B.8. Click OK. Repeat this step for Strain30, Strain40, Strain50, and Strain60 tables.

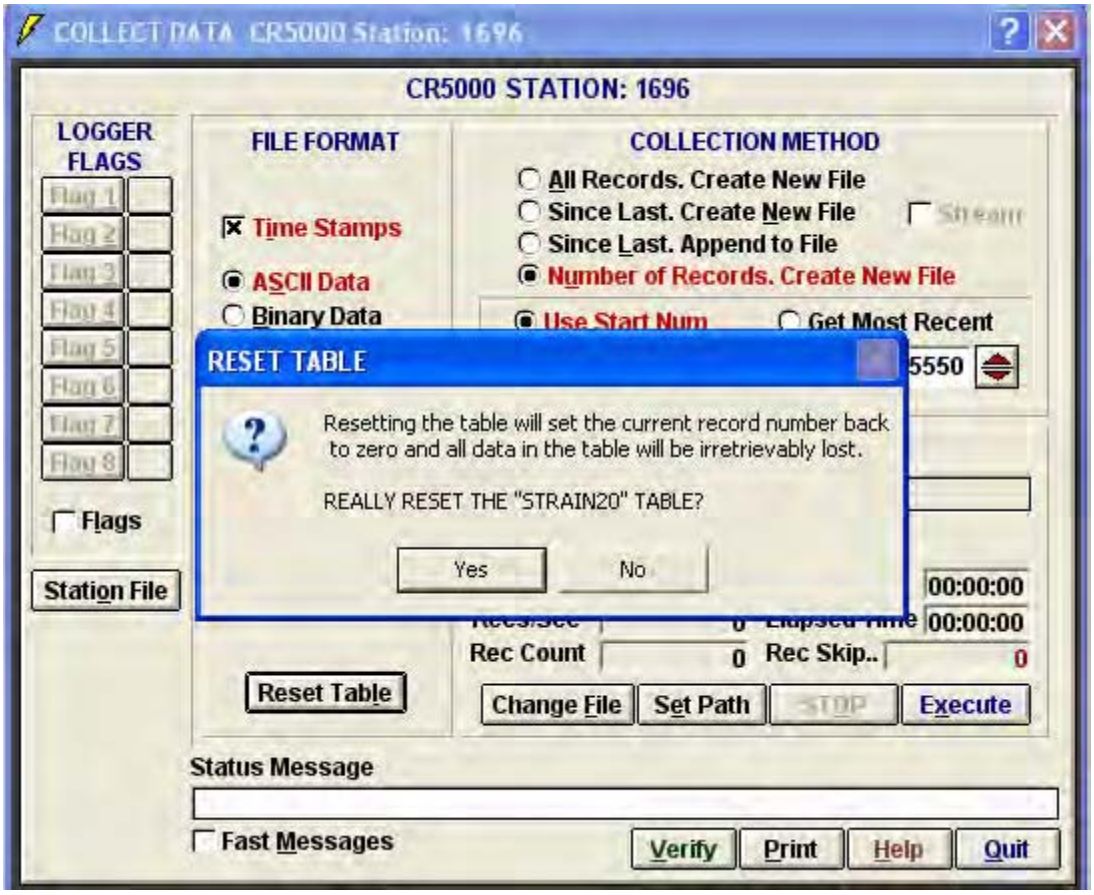


Figure B.8

10. Double check the flag box. Flag1 should read HI as shown in Figure B.9. If Flag1 reads LO, click on the LO box to change to HI. Click on the Quit button on the Collect Data Screen.

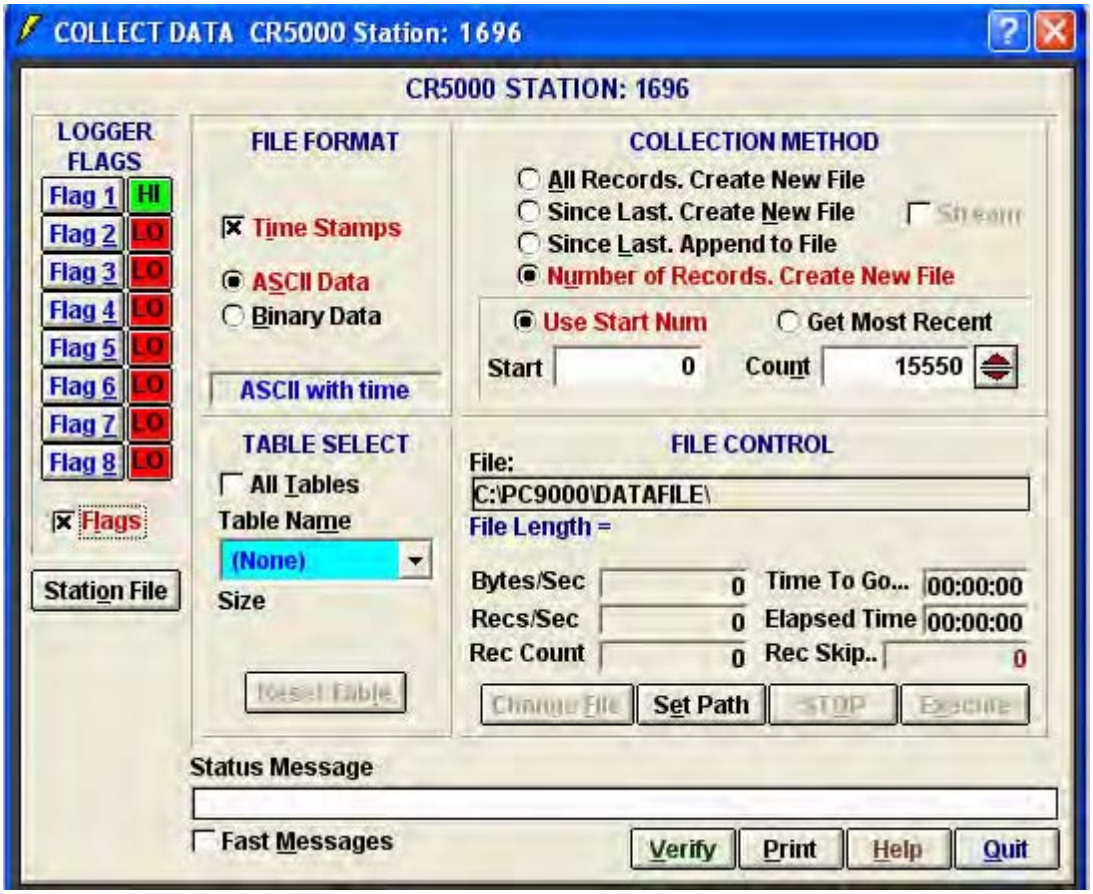


Figure B.9

11. Remove the serial cable from the CR5000 RS-232 port and laptop serial cable port.

12. Power down the laptop and place the CR5000 back into the security box.

## APPENDIX C BOUNDARY CONDITIONS DIAGRAM

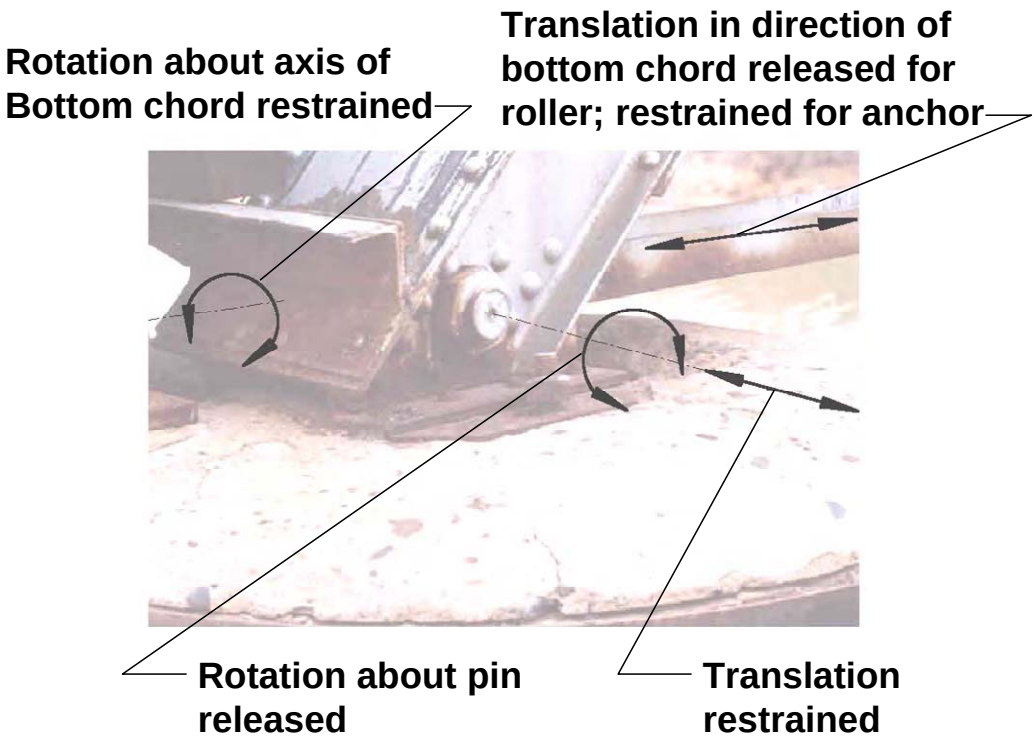


Figure C.1. Illustration of Boundary Conditions for Actual Bearings. The diagram is superimposed on a photograph of the northwest bearing at the Fruita Bridge. The bottom chord eyebars are at the right. One end of the pin can be seen. The boundary conditions illustrated here were used for analytical models for cases where the bearings were supported on concrete piers or abutments. For cases where the bearing were completely buried, and presumably rusted to a "frozen" condition, the boundary condition was treated as fixed.

## APPENDIX D DATA LOGGER PROGRAM LISTING

The program VALNEW5 (refer to Section A.4.8) was downloaded from the laptop computer to the CR5000 data logger. A listing of the program follows:

```
Program name: VALNEW5.cr5
'                    Written by: Name
'                   I.D. number: Number
'                   Date written: 04-21-2004
'                   Time written: 16:34:53
'                 PC5GEN Version: 4.9.0070

' This program was generated using Campbell Scientific's PC5GEN
' Program Generator for the CR5000 Measurement & Control System.

'\\\\\\\\\\\\\\\\\\\\\\\\ TIMING CONSTANTS ////////////////////////

Const PERIOD = 100                'Scan interval number
Const P_UNITS = 1                 'Scan interval units (mSecs)


Public WindSpeed(5), WindInterval(5)
Units Windspeed=MPH

'\\\\\\\\\\\\\\\\\\\\\\\\ BRIDGE CONSTANTS ////////////////////////

'_____________________________ Bridge Block 1 _____________________________
Const BRNG1 = 0                   'Block1 measurement range (mSecs)
Const BREP1 = 1                   'Block1 repetitions
Const BEXCIT1 = 1000              'Block1 excitation mVolts 5000 to 1000 db 3-18
Const BSETL1 = 2000               'Block1 settling time (usecs)
Const BINT1 = 250                 'Block1 integration time (usecs)
Const BMULT1 = 355                'Block1 default multiplier
Const BOSET1 = 0                  'Block1 default offset
Public BBlk1(BREP1)               'Block1 dimensioned source
Units BBlk1 = Volts               'Block1 default units (Volts)
'_____________________________ Bridge Block 2 _____________________________
Const BRNG2 = 40                  'Block2 measurement range (mSecs)
Const BREP2 = 16                  'Block2 repetitions
Const BEXCIT2 = 2500              'Block2 excitation mVolts
Const BSETL2 = 400                'Block2 settling time (usecs)
Const BINT2 = 500                 'Block2 integration time (usecs)
Const BGF2 = 2.065                'Block2 gauge factor
Const BCODE2 = 1                  'Block2 gauge code for 1/4 bridge strain
Const BMULT2 = 1                  'Block2 default multiplier
Const BOSET2 = 0                  'Block2 default offset
Public BBlk2(BREP2)               'Block2 dimensioned source
```

```
Public BBlk2mV(BREP2)
Dim GBBlk2(BREP2)                    'Block2 dimensioned gauge factor
Dim BBlk2ZeroMv(BREP2)                'Block2 zero mV variable
Dim BBlk2ZeroUs(BREP2)                'Block2 zero uStrain variable
Units BBlk2ZeroMv = mVperV            'Block2 default units (mVperV)
Units BBlk2ZeroUs = uStrain           'Block2 default units (uStrain)
Units BBlk2 = uStrain                'Block2 default units (uStrain)
Units BBlk2mV = mVperVolt

'\\\\\\\\\\\\\\\\\ ALIASES & OTHER VARIABLES ////////////////////

Alias BBlk1(1) = WindDir              'Assign alias name "WindDir" to BBlk1(1)
Units WindDir = Degrees               'Assign units "Degrees" to WindDir
Alias BBlk2(1) = Strain1             'Assign alias name "Strain1" to BBlk2(1)
Alias BBlk2(2) = Strain2             'Assign alias name "Strain2" to BBlk2(2)
Alias BBlk2(3) = Strain3             'Assign alias name "Strain3" to BBlk2(3)
Alias BBlk2(4) = Strain4             'Assign alias name "Strain4" to BBlk2(4)
Alias BBlk2(5) = Strain5             'Assign alias name "Strain5" to BBlk2(5)
Alias BBlk2(6) = Strain6             'Assign alias name "Strain6" to BBlk2(6)
Alias BBlk2(7) = Strain7             'Assign alias name "Strain7" to BBlk2(7)
Alias BBlk2(8) = Strain8             'Assign alias name "Strain8" to BBlk2(8)
Alias BBlk2(9) = Strain9             'Assign alias name "Strain9" to BBlk2(9)
Alias BBlk2(10) = Strain10           'Assign alias name "Strain10" to BBlk2(10)
Alias BBlk2(11) = Strain11           'Assign alias name "Strain11" to BBlk2(11)
Alias BBlk2(12) = Strain12           'Assign alias name "Strain12" to BBlk2(12)
Alias BBlk2(13) = Strain13           'Assign alias name "Strain13" to BBlk2(13)
Alias BBlk2(14) = Strain14           'Assign alias name "Strain14" to BBlk2(14)
Alias BBlk2(15) = Strain15           'Assign alias name "Strain15" to BBlk2(15)
Alias BBlk2(16) = Strain16           'Assign alias name "Strain16" to BBlk2(16)

Dim Leadlength(16)
Public Leadresistance(16), AdjGF(16)
Public Flag(8)                       'General Purpose Flags
Dim I                               'Declare I as a variable
Dim Count                            'Declare Count as a variable

'\\\\\\\\\\\\\\\\\\\\\\ OUTPUT SECTION ////////////////////////

'----------------------------- Table 1-----------------------------
DataTable(STRAIN,True,-1)              'Trigger, auto size
  DataInterval(0,0,0,100)             'Synchronous, 100 lapses, autosize
  CardOut(0,-1)                       'PC card , size Auto
  '_____________________________ Bridge Blocks _____________________________
  Sample (5,WindSpeed(),IEEE4)
  Sample (BREP1,BBlk1(),IEEE4)         '1 Reps,Source,Res
  Sample (BREP2,BBlk2(),IEEE4)         '16 Reps,Source,Res
  Sample (BREP2,BBlk2mV(),IEEE4)       '16 Reps,Source,Res
EndTable                              'End of table STRAIN

'--------------- Store zero values from Sub Zero8 ----------------
DataTable(ZERO_8,Count>99,100)         'Trigger on Count 100
  Average(BREP2,BBlk2ZeroMv(),IEEE4,False)'16 Reps,Source,Res,Enabled
  Average(BREP2,BBlk2ZeroUs(),IEEE4,False)'16 Reps,Source,Res,Enabled
EndTable                              'End of table ZERO_8

'\\\\\\\\\\\\\\\\\\\\\\\\\ SUBROUTINES ///////////////////////////
```

```
Sub Zero8                          'Begin zero measure routine
  Count = 0                        'Set Count to zero
  Scan(PERIOD,P_UNITS,0,100)       'Scan 100 times. 10.00 Seconds.

BrFull(BBlk2ZeroMv(),BREP2,BRNG2,2,VX2,6,BEXCIT2,True,False,BSETL2,BINT2,BMULT2,B
OSET2) 'Strain
    StrainCalc(BBlk2ZeroUs(),BREP2,BBlk2ZeroMv(),0,BCODE2,AdjGF(),0)
    Count = Count + 1              'Increment Count
    CallTable ZERO_8               'Go up and run Table ZERO_8
  Next Scan                        'Loop up for the next scan
  For I = 1 To BREP2               'Do this 16 times
    BBlk2ZeroMv(I) = ZERO_8.BBlk2ZeroMv_Avg(I,1)
  Next I                           'Do it again
  Flag(8) = False                  'Reset Flag(8)
End Sub                            'End gauge zero measure routine

'\\\\\\\\\\\\\\\\\\\\\\\\\\ PROGRAM //////////////////////////

BeginProg                          'Program begins here
  'MainSequence
  For I = 1 To BREP2               'Do the following to all of BBlk2
    GBBlk2(I) = BGF2               'Assign default gauge factor (2.065) to GBBlk2
  Next I                           'Repeat above until finished

  'Load Lead lengths( hundreds of feet)
   Leadlength(1) = 1.40
   Leadlength(2) = 1.40
   Leadlength(3) = 1.40
   Leadlength(4) = 1.40
   Leadlength(5) = 1.60
   Leadlength(6) = 1.60
   Leadlength(7) = 1.60
   Leadlength(8) = 1.60
   Leadlength(9) = 2.30
   Leadlength(10) = 2.30
   Leadlength(11) = 2.50
   Leadlength(12) = 2.50
   Leadlength(13) = 0.80
   Leadlength(14) = 0.80
   Leadlength(15) = 1.00
   Leadlength(16) = 1.00

'   Calculate lead resistance (ohms); 18 gague wire - 0.692 ohms per 100  feet
  For  I = 1 to 16
    Leadresistance(I) = Leadlength(I) * 0.692
  Next I

  '  Calculate adjusted gauge factor based on lead resistance: Adjusted GF  = GF *
(RGauge/(RGauge + RLead))
  For  I = 1 to 16
    AdjGF(I) = GBBlk2(I) * 120/(120 + Leadresistance(I))
  Next I


  Scan(PERIOD,P_UNITS,200,0)       'Scan once every 100 mSecs, non-burst
```

```
    '  _____INT8 Wind Speed Measurements_____
  sdmspeed(20)
    INT8 (WindInterval(),0,0002,2222,0001,1111,32768,0,.00059630,0)
'       INT8 (WindSpeed(),0,0002,2222,0002,2222,32768,0,1667,.40)
   For I = 1 to 5
    WindSpeed(I) = 1/WindInterval(I) + 0.4
    If WindSpeed(I) < 1.6 then WindSpeed(I) = 0
   Next I


  'Wire Wind Direction into channel SE1
 ' Use excitation channel 1.

      '_____ Bridge Blocks _____
    BrHalf(BBlk1(),BREP1,BRNG1,1,VX1,1,BEXCIT1,True,BSETL1,BINT1,BMULT1,BOSET1)

BrFull(BBlk2mV(),BREP2,BRNG2,2,VX1,4,BEXCIT2,True,False,BSETL2,BINT2,BMULT2,BOSE
T2) 'Strain
    StrainCalc(BBlk2(),BREP2,BBlk2mV(),BBlk2ZeroMv(),BCODE2,AdjGF(),0) 'Strain calculation
    If Flag(8) Then Zero8          'Go do Zero8 subroutine

    '_____ Output Table Control _____
    If  Flag(1) Then CallTable STRAIN
  Next Scan                    'Loop up for the next scan

  '\\\\\\\\\\\\\\\\\\\\\\\\ LOW PRIORITY ////////////////////////

'  BackgroundSequence
  SlowSequence                  'Used for slow measurements
  Dim CountSlow                 'Dimension CountSlow
  Dim TripVolt                  'Dimension TripVolt
  Dim CountAvg                  'Dimension CountAvg
  '---------------------------------------------------------------
  Scan(1,Sec,0,0)               'Scan once every 1 second
    Battery(TripVolt)           'Battery voltage measurement
    CountSlow = CountSlow + 1       'Increment counter
    If CountSlow >= 60 Then         'Test counter
      CountSlow = 0             'Reset counter
      '_____ Battery Saver _____
      AvgRun(TripVolt,1,TripVolt,10)  'Running average (10 mins) of TripVolt
      CountAvg = CountAvg + 1       'Increment CountAvg
      If CountAvg > 9 Then          'Test TripVolt after 10 AvgRun inputs
        CountAvg = 0            'Reset AvgCount after it equals 10
        If TripVolt < 11.0 Then     'Test for less than 11.5 volts
          PowerOff(0,0,Min)     'Kill the Logger
        End If                  'End of If TripVolt
      End If                    'End of If CountAvg
  '   '-------------------------------------------------------------
    End If                      'End of If
  Next Scan                     'Loop up for the next scan


EndProg                         'Program ends here

'***** Program End *****
```

## REFERENCES


AASHTO (1997). *Guide Specifications for Design of Pedestrian Bridges*, American Association of State Highway and Transportation Officials, Washington, D.C.

AISC (2001). *Manual of Steel Construction – Load and Resistance Factor Design*, American Institute of Steel Construction, Chicago, 3rd ed.

American Society of Civil Engineers (ASCE). (1961). "Wind forces on structures", *Transactions of the American Society of Civil Engineers*, 126, II, 1124.

American Society of Civil Engineers (ASCE). (2002). *ASCE 7-02 Minimum design loads for buildings and other structures,* Reston, VA, Table C6-1.

Bathe, K.J. (1996). *Finite element procedures,* Prentice-Hall, Englewood Cliffs, NJ, 420-449.

Belove, C. (1986). *Handbook of modern electronics and electrical engineering*, John Wiley & Sons, New York, Table 7.9.

Campbell Scientific (1996a). *03001 Wind sentry instruction manual*, Campbell Scientific, Inc., Logan, Utah.

Campbell Scientific (1996b). *4WFB120, 4WFB350, 4WFB1K, 4 wire full bridge terminal input modules instruction manual*, Campbell Scientific, Inc., Logan, Utah.

Campbell Scientific (2001). *CR5000 measurement and control system operator's manual*, Campbell Scientific, Inc., Logan, Utah.

Cooper, T. (1905). "What Wind Pressure Should be Assumed in the Design of Long Bridge Spans?", *Engineering News*, 5 Jan., 15-16.

DeLony, E (2005). "Rehabilitation of Historic Bridges", *Journal of Professional Issues in Engineering Education and Practice*, American Society of "Civil Engineers, Reston, VA, July, 131, 3, 178.

DeLorme (1997a). Colorado Atlas & Gazetteer, DeLorme, Yarmouth, ME, 99.

DeLorme (1997b). Colorado Atlas & Gazetteer, DeLorme, Yarmouth, ME, 38.

DeLorme (1997c). Colorado Atlas & Gazetteer, DeLorme, Yarmouth, ME, 64.

Hatfield, F. J. (2001). "Engineering for Rehabilitation of Historic Metal Truss Bridges", *Proceedings of the 7th Historic Bridges Conference*, Sponsored by Wilbur J. and Sara Ruth Watson Bridge Book Collection, Cleveland State University, Sept. 19 – 22, Cleveland, OH.

Herrero, T. (2003). *Development of strain transducer prototype for use in field determination of bridge truss member forces*, Civil Engineering Dept., Univ. of Colorado at Denver, Denver.

Ketchum, M.S. (1908). *The design of highway bridges and the calculation of stresses in bridge trusses*, McGraw-Hill, New York, 141-155.

RAM (2005). RAM Advanse, ver. 7.0, RAM International, Carlsbad, CA.

RISA (2002). *RISA-3D*, ver. 4.5, Risa Technologies, Foothill Ranch, CA.

Rutz, F.R. (2004a). *Lateral load paths in historic truss bridges*, PhD Thesis, Civil Engineering, University of Colorado at Denver, 69-70.

Rutz, F.R. (2004b). *Lateral load paths in historic truss bridges*, PhD Thesis, Civil Engineering, University of Colorado at Denver, 31-32.

Rutz, F.R., and Rens, K.L. (2004). "Alternate load paths in historic truss bridges: new approaches for preservation," *Proceedings of the 2004 Structures Congress*, Ed. by G.E. Blandford, Structural Engineering Institute of the American Society of Civil Engineers, May 22-26, Nashville, TN, ASCE, Reston VA.

Smith, C.S. (1881). "Wind Pressure Upon Bridges", *Engineering News*, 1 Oct. 395.

USGS. (1973). *Topographic map: Fruita quadrangle*, U.S. Dept. of Interior, Geological Survey, Denver.

Vishay (2004). "Errors due to leadwire resistance." *Technology*, Vishay Measurements Group, Raleigh, <http://www.vishay.com/brands/measurements_group/guide/ta/lwr/wclwr.htm> (May 7, 2004).

Waddell, J.A.L. (1898a). *De pontibus*, John Wiley & Sons, New York, 332-335.

Waddell, J.A.L. (1898b). *De pontibus*, John Wiley & Sons, New York, 224 and Plate VIII.